

# The Low Temperature Magnetic Relaxation of $\text{Dy}_2\text{Ti}_2\text{O}_7$

by

Halle Revell

A thesis  
presented to the University of Waterloo  
in fulfillment of the  
thesis requirement for the degree of  
Master of Science  
in  
Physics

Waterloo, Ontario, Canada, 2012

© Halle Revell 2012



I hereby declare that I am the sole author of this thesis. This is a true copy of the thesis, including any required final revisions, as accepted by my examiners.

I understand that my thesis may be made electronically available to the public.



## Abstract

The recent formulation of the monopole picture of spin ice[1, 2, 3], has lead to several studies of the signatures of monopole excitations[2, 4], as well as studies of the motion of magnetic monopoles[5, 6, 7]. In this thesis low temperature dynamics of the dipolar spin ice material  $\text{Dy}_2\text{Ti}_2\text{O}_7$  are examined through SQUID measurements of the dc magnetic relaxation. The results are compared to recent ac susceptibility measurements[8] and new Monte Carlo simulations. It is found that instead of the relaxation being a single exponential decay with a temperature-activated relaxation time, which is what is expected from the dipolar spin ice model[9, 10, 11], the relaxation is a stretched exponential that develops into a long-time tail. The relaxation has a temperature-activated relaxation time,  $\tau(T) = \tau_o \exp(\Delta E/kT)$ , that has an energy barrier,  $\Delta E/k$ , of  $\sim 9\text{ K}$ , as opposed to the  $\sim 5\text{ K}$  energy barrier predicted by the dipolar spin ice model. By comparison to dynamic Monte Carlo simulations the stretched exponential behaviour is attributed to surface effects of the sample and the long-time tail is explained by a small amount (0.3%) of stuffed Dy spins in the material. The 9 K energy barrier is explained by assuming that the basic spin flip process is not fully temperature independent and instead has an energy barrier of 4 K. This study should bring to light the importance of taking material defects and surface effects into account as one would in an electric conductor, whose material defects lead to resistance. Even in the case of the spin ice materials, which are usually assumed to be extremely “clean”, defects can play an important role in the dynamics and this study is the first instance where resistance meets “magnetism”.



## Acknowledgements

I would like to first acknowledge my supervisor Dr. Jan Kycia. Without his support, insight, and drive, I would not be where I am right now. His intuition when it comes to physics is impressive and his passion for the experiment is contagious to everyone around you. I want to acknowledge Patrik Henelius, our theorist collaborator on this work. Patrik performed the Monte Carlo simulations presented in this thesis and gave tremendous insight and guidance regarding the interpretation of my results. He also was extremely fun to work with. Thank you to my committee for providing valued insight along the way: Anton Burkov, Hart Peemoeller, and Rob Hill. Thank you to Jeff Mason for being my fridge partner. We were some how always able to make a laugh out of working on the fridge. All the helium transfers and guidance were much appreciated. I would like to thank Luke Yaraskavitch, my close friend and colleague, for teaching me so much around the lab, but mostly for all the epic coffee breaks and fun nights out with friends. I want to acknowledge Shuchao Meng for stimulating conversations and teaching me so much in the lab, specifically photolithography and making coaxial cables. Thanks also to David Pomaranski, Lauren Persaud, Jeff Quilliam, Borko Djurkovic, Shaoxiong Li, Dave Vresk, Chas Mugford, Will Teows, Kevin Liu who are people who I have worked with in the lab and who have all at one time or another helped me with something. Thank you to my grad school friends: Mike Wesolowski, Chad Daley, Ann Kallin, Behnam Javanparast, Stephen Inglis (the ninja, who taught me a lot of theory), Jason Iaconis, Jordan Thompson, Troy Borneman, Adam (Marion) Patznieck, Lori Woolner-Melko. Thank you to my roommates I found randomly who turned out to be amazing friends, Shanna Walters and Preet Pannu. Thank you to Karla Williams, my best friend in the entire world. To all the other friends I have met in Waterloo, thank you. Mom and Dad, you guys have supported me from day one and taught me you can work hard and still find time to have lots of fun. I get my intensity, determination, and passion for life from you guys. Jackie, you are the funniest, most awesome brother in the world - *nobody* knows me the way you do. Thank you to everyone at my dad's house (Kathy, Kristyn, Lucas, Jeff, Marguerite) for your continued support and thank you Moss for your support and for making my mom so happy. I would like to acknowledge my grandmother, Joan Ackerman, and late grandfather Gordon Ackerman - I love you two so, so much. Andrew Achkar, you are the most supportive, loving, intelligent and down-right-hilarious person I have ever known. Thank you from the bottom of my heart for being in my life and loving me so much; I love you.





## **Dedication**

This thesis is dedicated to my mom (Gay), dad (Kevin), brother (Jackson), and Andrew.



# Table of Contents

List of Tables	xiii
List of Figures	xv
<b>1 Introduction</b>	<b>1</b>
<b>2 Spin Ice</b>	<b>5</b>
2.1 Pyrochlore Oxides . . . . .	5
2.2 Spin Ice Model . . . . .	6
2.3 Dipolar Spin Ice Model . . . . .	8
2.4 Magnetic Monopoles . . . . .	10
2.5 Low Temperature Relaxation Times . . . . .	19
<b>3 Experimental Details</b>	<b>27</b>
3.1 DC SQUID Background . . . . .	27
3.2 The DC SQUID Gradiometer . . . . .	30
3.3 Magnetometer Design . . . . .	33
3.4 Sample Details . . . . .	37
<b>4 Results</b>	<b>39</b>
4.1 AC Susceptibility of $\text{Dy}_2\text{Ti}_2\text{O}_7$ . . . . .	39
4.2 DC Magnetization of $\text{Dy}_2\text{Ti}_2\text{O}_7$ . . . . .	43

<b>5</b>	<b>Comparison to AC Susceptibility and Monte Carlo Simulation</b>	<b>53</b>
5.1	Comparison to AC Susceptibility . . . . .	53
5.2	Comparison to Monte Carlo Simulation . . . . .	56
5.3	Two- $\tau$ Model: Comparison to Recent Work . . . . .	64
<b>6</b>	<b>Bringing It All Together</b>	<b>69</b>
<b>7</b>	<b>Conclusions</b>	<b>73</b>
7.1	Implications . . . . .	74
<b>A</b>	<b>Fitting Details</b>	<b>75</b>
A.1	Determining Zero . . . . .	75
A.2	Normalizing . . . . .	76
A.3	Signal Averaging . . . . .	76
A.4	Fitting Limits . . . . .	79
A.5	Fit Functions . . . . .	79
A.6	Fitting Methods . . . . .	79
<b>B</b>	<b>Measurement Challenges</b>	<b>85</b>
B.1	Vibrations . . . . .	85
B.2	Magnetic Shielding . . . . .	85
B.3	Backaction . . . . .	86
<b>C</b>	<b>Demagnetization</b>	<b>89</b>
	<b>References</b>	<b>93</b>

# List of Tables

3.1	Dimensions and crystal orientations of the samples (in cm). . . . .	37
-----	---	----



# List of Figures

2.1	The pyrochlore lattice . . . . .	7
2.2	The specific heat of $\text{Dy}_2\text{Ti}_2\text{O}_7$ from Monte Carlo simulation . . . . .	9
2.3	The creation of a monopole pair . . . . .	11
2.4	The creation and separation of two monopoles . . . . .	12
2.5	Comparison of relaxation times from theory and ac susceptibility . . . . .	14
2.6	Magnetization relaxations at 360 mK from Giblin <i>et al.</i> [6] . . . . .	16
2.7	Magnetization relaxations for different temperatures from Giblin <i>et al.</i> [6] . . . . .	17
2.8	Relaxation frequencies obtained from previous ac susceptibility work . . . . .	21
2.9	Current ac susceptibility results . . . . .	22
2.10	Comparison of ac susceptibility, thermal relaxation, and magnetocaloric measurements . . . . .	24
3.1	The operation of a dc SQUID . . . . .	28
3.2	How a first-order SQUID gradiometer works . . . . .	31
3.3	Schematic of the SQUID gradiometer with pick-up coils . . . . .	32
3.4	Microscopic image of holes made in the substrate . . . . .	33
3.5	Schematic of the experimental stage of the magnetometer . . . . .	34
3.6	Images of the magnetometer . . . . .	35
4.1	AC susceptibility spectra . . . . .	40
4.2	AC susceptibility data obtained with new magnetometer . . . . .	42

4.3	Magnetic relaxation at 0.55 K . . . . .	43
4.4	Magnetic relaxation at 0.9 K . . . . .	44
4.5	Magnetic relaxation data: $C(t)$ vs. $t$ . . . . .	45
4.6	Magnetic relaxation data: $\ln(-\ln(C(t)))$ vs. $\ln(t)$ . . . . .	47
4.7	Stretch exponential factor vs. inverse temperature . . . . .	49
4.8	Relaxation times vs. inverse temperature . . . . .	50
5.1	Different fits to the out-of-phase susceptibility . . . . .	54
5.2	Monte Carlo simulation compared to experiment . . . . .	55
5.3	Decay of correlations from simulations . . . . .	58
5.4	Configuration of a stuffed spin . . . . .	61
5.5	Energy and monopole density as a function of distance from a stuffed spin . . . . .	62
5.6	Two- $\tau$ fit comparison of dc data . . . . .	65
5.7	Two- $\tau$ fit comparison of ac susceptibility data . . . . .	66
6.1	Measured relaxation in the context of other measurements . . . . .	72
A.1	Defining zeros in magnetic relaxation at $T = 0.9$ K . . . . .	77
A.2	Example of signal averaging . . . . .	78
A.3	Residuals used to estimate fitting limits . . . . .	81
A.4	Residuals of the different fits at 0.675 K . . . . .	82
A.5	Percent difference between fitting approaches . . . . .	83
B.1	Subtraction of oscillatory noise from vibrations . . . . .	87
B.2	Correction for back-action in gradiometer . . . . .	88
C.1	AC susceptibility spectra for two different geometries . . . . .	90
C.2	Calibrated ac susceptibility spectra for two different geometries . . . . .	91



# Chapter 1

## Introduction

Condensed matter physics, simply put, is the study of different phases of condensed matter. It is the study of how atoms arrange themselves within a material and the underlying forces that compete to form those arrangements. The field of study requires the use of many body statistical physics and has been known to give rise to some of the most difficult mathematical problems to date. Despite these challenges, condensed matter physicists know that their reward is to discover and gain understanding of exotic states of matter like superconductivity, superfluidity, spin liquidity, and multiferroics, to name a few. Not only do the materials that exhibit these states of matter have the ability to change our world both technologically and economically, but they are constantly challenging old ways of understanding the electronic properties of matter.

One of the forefronts of study in this arena is frustration. Frustration arises when a material cannot satisfy all of its interactions simultaneously, due to geometry of its crystal lattice. The classic example is an antiferromagnetic nearest neighbour interaction on a 2D triangular lattice with Ising spins on the vertices. Considering one triangle in the lattice, when two spins anti-align, the third spin has no preferred alignment, and there is a degeneracy and residual entropy at zero temperature. This picture can be expanded by considering a ferromagnetic nearest neighbour interaction on a 3D pyrochlore lattice, which is a lattice of corner-sharing tetrahedra. If the spins are Ising along the local  $\langle 111 \rangle$  axes, pointing either in or out of each tetrahedra, each tetrahedra will have a 6-fold degeneracy. This is the case for the materials known as spin ices, which will be the focus of this thesis.

In the last fifteen years, the subject of spin ice has gained a vast amount of attention in the condensed matter community. Initial interest arose when Bramwell and Harris discovered what appeared to be a geometrically frustrated system with ferromagnetic

nearest-neighbour exchange.[12] The material was  $\text{Ho}_2\text{Ti}_2\text{O}_7$ , now a well-established spin ice.  $\text{Ho}_2\text{Ti}_2\text{O}_7$  is a pyrochlore oxide, whose magnetic spins sit on the vertices of corner-sharing tetrahedra. The single ion anisotropy, in combination with what appeared to be a ferromagnetic coupling, seemed to explain the observed frustration. Gingras and den Hertog richened the picture by considering dipolar interactions, which turn out to play a large role in the system.[9] On the experimental front, these materials have garnered immense interest as they contain rich physics and single crystal samples can be grown or obtained with ease. The interesting physics in these materials spans a large temperature range, attracting both low and more intermediate temperature researchers. Ramirez and colleagues were first to measure the zero-point entropy of  $\text{Dy}_2\text{Ti}_2\text{O}_7$ , another spin ice material, and demonstrate the connection to water ice, from where the material gets its name.[13]

The association that spin ice has to common water ice is important. Water ice is an example of a solid that has residual entropy - disorder at absolute zero temperature. It is where the study of frustration began. Bernal and Fowler first introduced the “ice rules” which govern the ground state of hexagonal water ice and state that on each oxygen site there must be two near protons and two far.[14] Pauling took this a step further and calculated the residual entropy of water ice.[15] When Ramirez measured the specific heat of  $\text{Dy}_2\text{Ti}_2\text{O}_7$ , he observed Pauling’s entropy.[13] Finding a magnetic analogue to water ice, 64 years after Pauling calculated the residual entropy, was quite a feat and generated much excitement in the field, as these materials could be more easily studied than water ice. In addition, the application of a magnetic field is a tuneable control knob within the Hamiltonian of the system that water ice does not possess.

More recently, low temperature excitations out of spin ice state in  $\text{Dy}_2\text{Ti}_2\text{O}_7$  and  $\text{Ho}_2\text{Ti}_2\text{O}_7$  have been viewed as “magnetic monopoles”. [1, 2, 5, 10, 16] From this new picture, new experimental results and theories have emerged.[6, 11, 17, 18] Previously, the main mystery was that no order had been observed down to 50 mK when the dipolar spin ice model predicts a transition, although it was suggested that ordering wait times became too long for actual experiments.[19] Currently, the nature of the dynamics of spin ice at low temperature is generating the majority of open questions. Theories describing the dynamics in the context of the monopole picture, such as the gas of monopoles or the Debye-Huckel theory[10, 18], do not agree well below 1 K with ac susceptibility experiments[8, 20]. This disagreement will be elaborated upon in the following chapter. An exciting paper relating the induction of a current of monopoles by the application of a magnetic field to the Onsager-Wien effect in electrolytes, within a limited temperature range, suggested that faster modes of relaxation exist in the system than previously expected.[6] Connecting ac susceptibility data with time based dc magnetization measurements in order to shed light on the disagreement between theory and experiment is the goal of the work presented in

this thesis.

In the following Chapter entitled, “Spin Ice”, the basics of spin ice theory and previous experiments will be presented. The monopole picture of spin ice will also be explained, highlighting key experiments that support the theory. The aim is to motivate the experimental work performed in this thesis. In the third chapter, experimental details of the project will be given. Finally, the results and conclusions of the project will be presented and explained. Over the course of this degree, a new homemade SQUID magnetometer was constructed and served as the main tool for performing both magnetization and ac susceptibility measurements of the spin ice material  $\text{Dy}_2\text{Ti}_2\text{O}_7$ .



# Chapter 2

## Spin Ice

### 2.1 Pyrochlore Oxides

Pyrochlore oxide materials have the chemical formula  $R_2M_2O_7$ , where R is a  $4f$  trivalent rare earth ion, and M is usually a tetravalent transition metal. These materials have a cubic pyrochlore crystal structure, which is a lattice of corner-sharing tetrahedra shown in Fig. 2.1. The R ions and M ions each sit on the corners of their own pyrochlore sublattice, which are interspersed. If either, or both, R and M are magnetic then geometric frustration will occur.[21] In a magnetic system the first interaction considered is typically the nearest neighbour exchange. Subsequent interactions such as dipolar, exchange beyond nearest-neighbour, or spin-orbit coupling determine what specific phases will develop at low temperature. Pyrochlore materials have been found to develop spin-liquid ( $Tb_2Ti_2O_7$  [22]), order-by-disorder ( $Er_2Ti_2O_7$  [23]), and conventional ( $Dy_2Ti_2O_7$ ,  $Ho_2Ti_2O_7$ ) and quantum spin ice ( $Yb_2Ti_2O_7$  [24]) phases at low temperature, which makes them a fascinating subject for condensed matter research. Gardner, Gingras and Greedan provide a thorough review of the pyrochlore materials in Ref. [21].

In the more specific case of the spin ice pyrochlores  $Dy_2Ti_2O_7$  and  $Ho_2Ti_2O_7$ <sup>1</sup>, the rare earth ions are magnetic and have a relatively large magnetic dipole moment. The magnetic moments of  $Dy^{3+}$  and  $Ho^{3+}$ , in terms of Bohr magnetons, are 10.6 and 10.4, respectively.[26] The large dipole moments, result in a sizeable dipolar interaction. The crystal field ground states of  $Ho_2Ti_2O_7$  and  $Dy_2Ti_2O_7$  are a single-ion doublet. The next highest excited state is on the order of 200 K (for  $Dy_2Ti_2O_7$ ) and 300 K (for  $Ho_2Ti_2O_7$ ),

---

<sup>1</sup> $Ho_2Sn_2O_7$  is also a spin ice material, but it is less studied as it is only available as a powder[25]

allowing the spins to be treated as classical Ising spins at temperatures of 10 K and below. The crystal electric field has a strong anisotropy and as a result the spins are Ising in the local  $\langle 111 \rangle$  crystal axis directions. This means the spins are constrained to point either directly in or out from the centre of the tetrahedra (see Fig. 2.1). The ground state of the system is such that two spins point in and two spins point out of each tetrahedra. This two-in-two-out constraint, was connected to the Bernal and Fowler ice rules[14] for water ice, which states that each oxygen should have two near protons and two far protons. This constraint is satisfied by a large number of spin configurations, leading to huge degeneracy. It was Pauling who quantified this degeneracy for water ice as  $\approx 3/2^{N/2}$ , corresponding to a macroscopic zero point entropy  $(R/2) \ln(3/2)$ , where  $R$  is the molar gas constant.[15] Ramirez *et al.* measured the zero-point entropy of  $\text{Dy}_2\text{Ti}_2\text{O}_7$  through specific heat and found it to be extremely close to this value.[13] Since then the magnetic analogues of water ice have been known as the spin ices.

## 2.2 Spin Ice Model

Although until the late 1990s, spin ice materials were not discovered, Anderson had noticed that antiferromagnetic Ising spins in the global  $z$  direction on pyrochlore lattice mapped onto Pauling's description of hexagonal water ice.[29] In 1997 Harris *et al.* realized that  $\text{Ho}_2\text{Ti}_2\text{O}_7$ , which was a pyrochlore material, appeared to have a ferromagnetic nearest neighbour exchange.[12]  $\text{Ho}_2\text{Ti}_2\text{O}_7$  was assumed to have ferromagnetic coupling between magnetic ions, because the material has a Curie-Weiss temperature of about +1.9 K. The first Hamiltonian used to describe spin ice materials is simply called the nearest neighbour spin ice model, which only took into account the nearest neighbour exchange interaction.[30] It turns out that a ferromagnetic coupling between Ising spins constrained to point along the local  $\langle 111 \rangle$  axes on the pyrochlore lattice maps onto Pauling's description of hexagonal water ice, similarly to Anderson's realization. This mapping seemed to explain why a system with ferromagnetic coupling would have no long range order down to 0.05 K, given the expected ground state entropy. However, in this simple model, there is no consideration of dipolar interactions, which one would expect to be comparable or even larger than the exchange interactions, given that the rare earth ions ( $\text{Ho}^{3+}$  and  $\text{Dy}^{3+}$ ) have large magnetic moments.

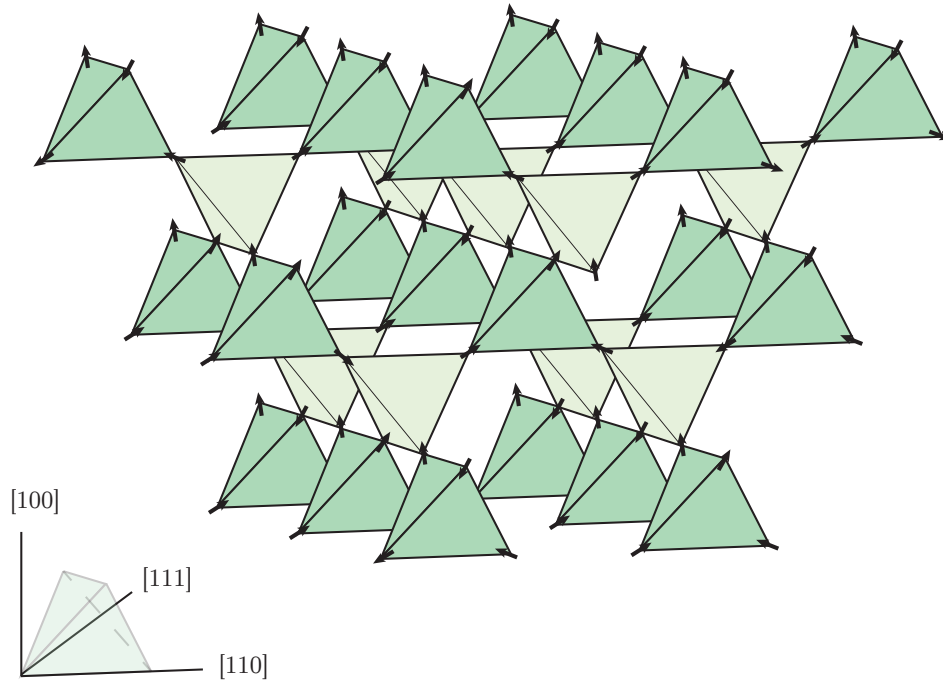


Figure 2.1: The pyrochlore lattice, in the case of  $\text{Dy}_2\text{Ti}_2\text{O}_7$  and  $\text{Ho}_2\text{Ti}_2\text{O}_7$ , where rare earth ions sit on the corners of the tetrahedra and experience an anisotropy from the crystal field which constrain the spins to point along the local  $\langle 111 \rangle$  axes (i.e. either toward the centre or away from the centre of each tetrahedron). The principle crystal axes are shown in the bottom left. Applying a magnetic field in the  $[100]$  direction results in all spins interacting with the field. Applying a field in the  $[110]$  direction, results in only two of the spins on each tetrahedra interacting with the field, while the other two are completely orthogonal to the field. Applying a field in the  $[111]$  direction results in one of the three spins on each tetrahedra being parallel to the applied field and the remaining three being weakly coupled, which leads to a breaking of the ice rules more often at even fairly weak field magnitudes.[27, 28]

## 2.3 Dipolar Spin Ice Model

Siddharthan *et al.* were first to consider the dipole-dipole interaction present in the spin ice system and calculated it out to the 5th nearest neighbour.[31] However, the dipolar spin ice model was fully realized by den Hertog and Gingras.[9] By taking into account the dipolar interactions out to infinity, using an Ewald summation technique, it was shown that although spin ice materials appeared to have nearest neighbour ferromagnetic exchange initially, the nearest neighbour exchange interaction is actually antiferromagnetic. The long range dipolar interactions, at the nearest neighbour level, are ferromagnetic. Therefore, since the nearest neighbour dipolar interaction has a larger interaction energy than the exchange, the effective exchange appears overall ferromagnetic. The dipolar spin ice model Hamiltonian is,

$$H = -J \sum_{\langle ij \rangle} \mathbf{S}_i^{z_i} \cdot \mathbf{S}_j^{z_j} + D r_{nn}^3 \sum_{j>i} \frac{\mathbf{S}_i^{z_i} \cdot \mathbf{S}_j^{z_j}}{|\mathbf{r}_{ij}|^3} - \frac{3(\mathbf{S}_i^{z_i} \cdot \mathbf{r}_{ij})(\mathbf{S}_j^{z_j} \cdot \mathbf{r}_{ij})}{|\mathbf{r}_{ij}|^5} \quad (2.1)$$

where  $\mathbf{S}_i^{z_i}$  represents the Ising moment at lattice site  $i$  and the local Ising axis is  $z_i$ . den Hertog and Gingras were able to use the Ewald summation technique to show that the dipolar interactions, when extended to infinity, cause the material to obey the ice rules.[9] If this model is reduced to include nearest neighbour interactions only (NN-DSI model) we obtain the following Hamiltonian,

$$H = -J_{\text{eff}} \sum_{\langle ij \rangle} \mathbf{S}_i^{z_i} \cdot \mathbf{S}_j^{z_j} \quad (2.2)$$

where  $J_{\text{eff}} = J_{\text{nn}} + D_{\text{nn}} = \frac{(J+5D)}{3}$ . For  $\text{Dy}_2\text{Ti}_2\text{O}_7$ ,  $D_{\text{nn}} \sim 2.35 \text{ K}$  and  $J_{\text{nn}} \sim -1.24 \text{ K}$ [9], making  $J_{\text{eff}}$  ferromagnetic overall. The most subtle point that den Hertog and Gingras make is that the special combination of  $1/r^3$  dipolar interactions and Ising anisotropy produces a behaviour that mimics the nearest neighbour spin ice model.

In subsequent work on the dipolar spin ice model, Melko *et al.*, developed a Monte Carlo loop algorithm, the results of which predict a first order phase transition to a long-range ordered phase with zero magnetization per unit cell.[19, 32] Fig. 2.2 contains the low temperature specific heat of the dipolar spin ice model that was obtained using the Monte Carlo loop algorithm. The algorithm cleverly uses loops that improve dynamics at low temperature and make it more computationally efficient to “wait” long enough for the system to order. They do not claim that this is experimentally achievable as the time scales become too long. The inclusion of the ordering peak also recovers the missing residual entropy reported by Ramirez *et al.*[13] To date, no experimental heat capacity



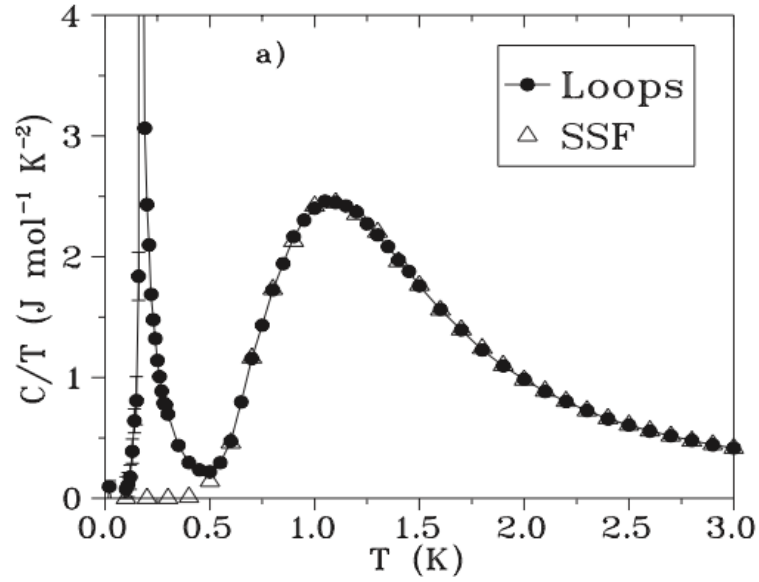


Figure 2.2: Low temperature specific heat of the dipolar spin ice model using Monte Carlo. The closed circles are using the loop algorithm developed by Melko *et al.* and the open triangles are using the single spin flip approach. There is a transition at  $T = 0.18 \text{ K}$ . From Ref. [19].

measurements of either  $\text{Ho}_2\text{Ti}_2\text{O}_7$  or  $\text{Dy}_2\text{Ti}_2\text{O}_7$  have been able to observe ordering down to  $50 \text{ mK}$ . [13, 16, 33, 34]

## 2.4 Magnetic Monopoles

In 2008, Castelnovo *et al.* introduced the monopole formulation of spin ice.[1] Although this was the first work to coin the term “monopole”, such defects in rare earth pyrochlores and their behaviour were introduced earlier by Ryzhkin in 2005.[3] Within the spin ice configuration, one can imagine each spin being replaced by a dumbbell with a positive and a negative end. The total length of the dumbbell is twice the length from a corner of a tetrahedron to its centre. This means that there are four dumbbell ends in the centre of each tetrahedron on the lattice. When in the spin ice state, since the dumbbell ends each have a positive or negative charge, the centre of each tetrahedron will have zero divergence as shown in Fig. 2.3 (c). However, once there is an excitation (single spin flip), as is shown on the right panel of Fig. 2.3, the two affected neighbouring tetrahedra will have equal and opposite total “magnetic charge”, as one will contain three positive dumbbell ends and the other will contain three negative dumbbell ends. Fig. 2.3 illustrates this concept, using the different representations of the system. The dumbbell picture can be further simplified by realizing that the spin ice state is a “vacuum state” for the magnetic monopoles and each single spin flip excitation creates two monopoles of equal and opposite magnetic charge that will be able to move in the “vacuum”.

The spin ice state is called a vacuum for the monopoles because the tetrahedra obeying the two-in-two-out constraint have zero divergence, and the tetrahedra containing monopoles have a non-zero divergence, similar to electric charges in a vacuum. The monopoles can become de-confined if there is enough screening present - i.e. the monopole density is high enough. This means that a monopole pair can be created and separate with a finite energy cost. The reason this is possible is because the monopoles can travel apart by means of subsequent single spin flips, that obey the ice rules. This is conceptualized in Fig. 2.4. The two monopoles which have separated are connected by a classical Dirac string.[1, 2] The string is tensionless and connected by the reversed spin flips along which the monopoles traveled. The strings are not unique, meaning there may be several chains of spins oriented such that they connect the same two monopoles. There is no energy associated with these strings, except the Coulomb interaction between the monopoles on its ends. These are classical Dirac strings, so they are observable, and in fact they were observed by Morris *et al.* in diffuse neutron scattering measurements.[2] In that paper, Debye-Hückel theory was used to calculate the specific heat and showed good agreement with the measurement. Debye-Hückel theory is a model that describes approximate treatment of dilute plasmas.[35] The monopole formulation of spin ice is born right out of the dipolar spin ice model, up to small corrections, and is described in detail in the supplementary information from Ref. [1].

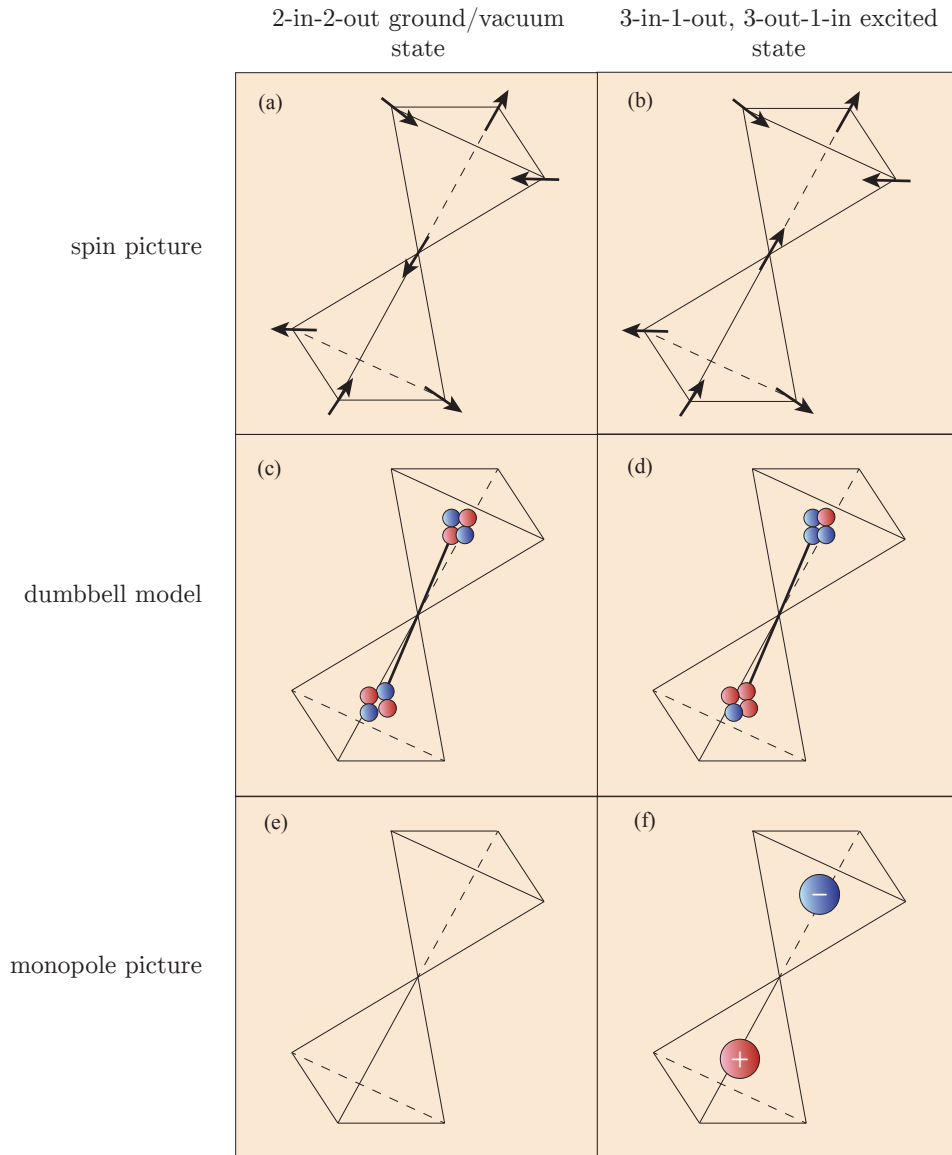


Figure 2.3: The creation of a monopole pair. **Left panels** (a, c, e) contain representations of the 2-in-2-out vacuum state. **Right panels** contain representations of a monopole excitation. **Top panels** (a, b) contain the spin representation, where the magnetic ions sit on the corners of the tetrahedra. **Middle panels** (c, d) contain the dumbbell representation of the system where each spin is replaced with a dipole dumbbell. **Bottom panels** (e, f) contain the monopole representation of the material where the 2-in-2-out state is a vacuum and a single excitation creates two monopoles of opposite polarity.

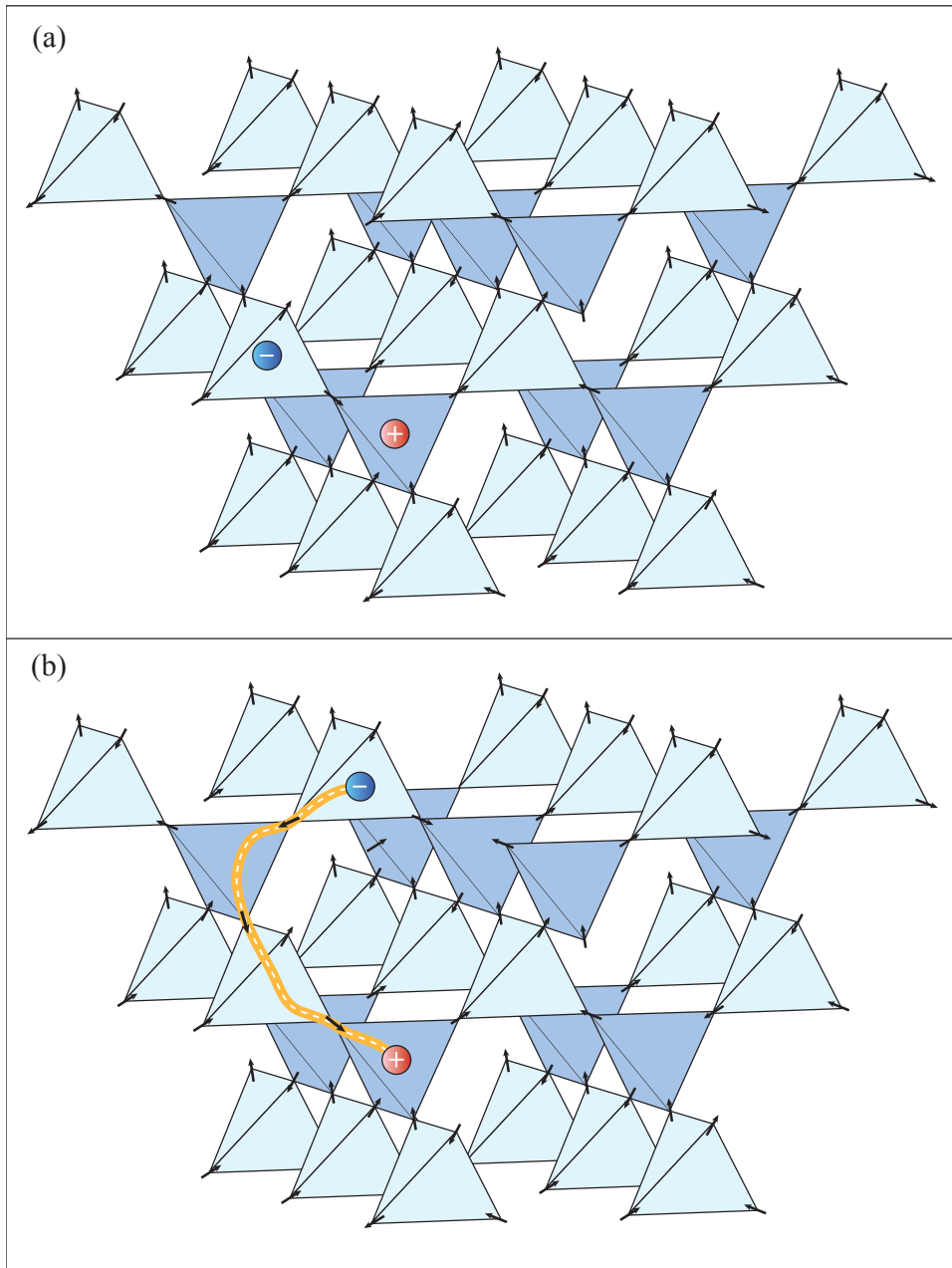


Figure 2.4: The creation and separation of magnetic monopoles in spin ice. (a) The pyrochlore lattice in the spin ice state, with one excitation, showing a monopole pair. (b) The same monopole pair after time having separated through subsequent spin flips which obey the ice rules. The pair is connected by a tensionless Dirac string.

Jaubert and Holdsworth performed Monte Carlo simulations of a Coulomb gas of magnetically charged particles in the grand canonical ensemble using Metropolis dynamics.[10] The goal of their simulations was to capture the crossover of the relaxation time from the quasi-plateau quantum tunnelling regime to the low temperature ( $< 2$  K) regime. The next section in this chapter will go into further detail regarding the importance of relaxation times, how to experimentally access them, and the different relaxation regimes in spin ice. Jaubert and Holdsworth compared their simulation results to the ac susceptibility data of Snyder *et al.*[36] Fig. 2.5 contains the two results in a plot of relaxation frequency against inverse temperature. By plotting the relaxation frequencies on a log scale against inverse temperature, which is most practical when trying to expose possible temperature activated behaviour, it can easily be seen that the two results are diverging at the lowest temperature. More recent ac susceptibility work [8], which is discussed in more detail throughout this thesis, is plotted on this graph as well. This newer ac susceptibility result goes to lower frequency and temperature than the measurements in Ref. [36] and does not quantitatively agree with the simulation in Ref. [10] below 1 K.

Castelnovo *et al.* recently published work which elaborates on Debye-Hückel theory of spin ice by comparing to simulations and ac susceptibility data.[18] In this work, several different theoretical models are compared to the ac susceptibility in Ref. [36]. In Fig. 2.5 the two models from Ref. [18] that agreed the best with the experimental data are shown. One can see that at low temperatures the experimental data is diverging from theory. The Arrhenius law with a dressed monopole energy  $\Delta_d$ , green curve, assumes that the energy barrier to relaxation is the cost of a defect (the creation of two monopoles) plus the energy to separate them such that they are deconfined (further apart than the screening length). The Debye-Hückel ( $\Delta = 4.57$ ), red curve, assumes that the relaxation is proportional to the inverse of the monopole density  $1/\rho$ , which is obtained from the Debye Hückel approximation. Neither of these theories is capturing the relaxation from either Ref. [36] or Ref. [8]. In the paper by Castelnovo *et al.*, theory and experiment are compared on a  $\log \tau$  versus  $\log T$  graph, where deviations at low temperature are less visible. As well, Castelnovo *et al.* present a phenomenological model, where an extra fitting parameter is introduced, resulting in a closer fit to the data from Ref. [36]. However, there is no justification for value of this extra parameter and it may be that the model is becoming underconstrained. For comparison purposes, simulation results from Ref. [10] have been added to Fig. 2.5.

Bramwell *et al.* set out to quantify the charge of the monopoles in spin ice using muon spin rotation measurements on  $\text{Dy}_2\text{Ti}_2\text{O}_7$ . [5] They experimentally quantified the charge by applying Onsager's theory of electrolytes [37] to the case of  $\text{Dy}_2\text{Ti}_2\text{O}_7$ . The experimental results appear to agree with the monopole charge calculated in Ref. [1]. Their result was

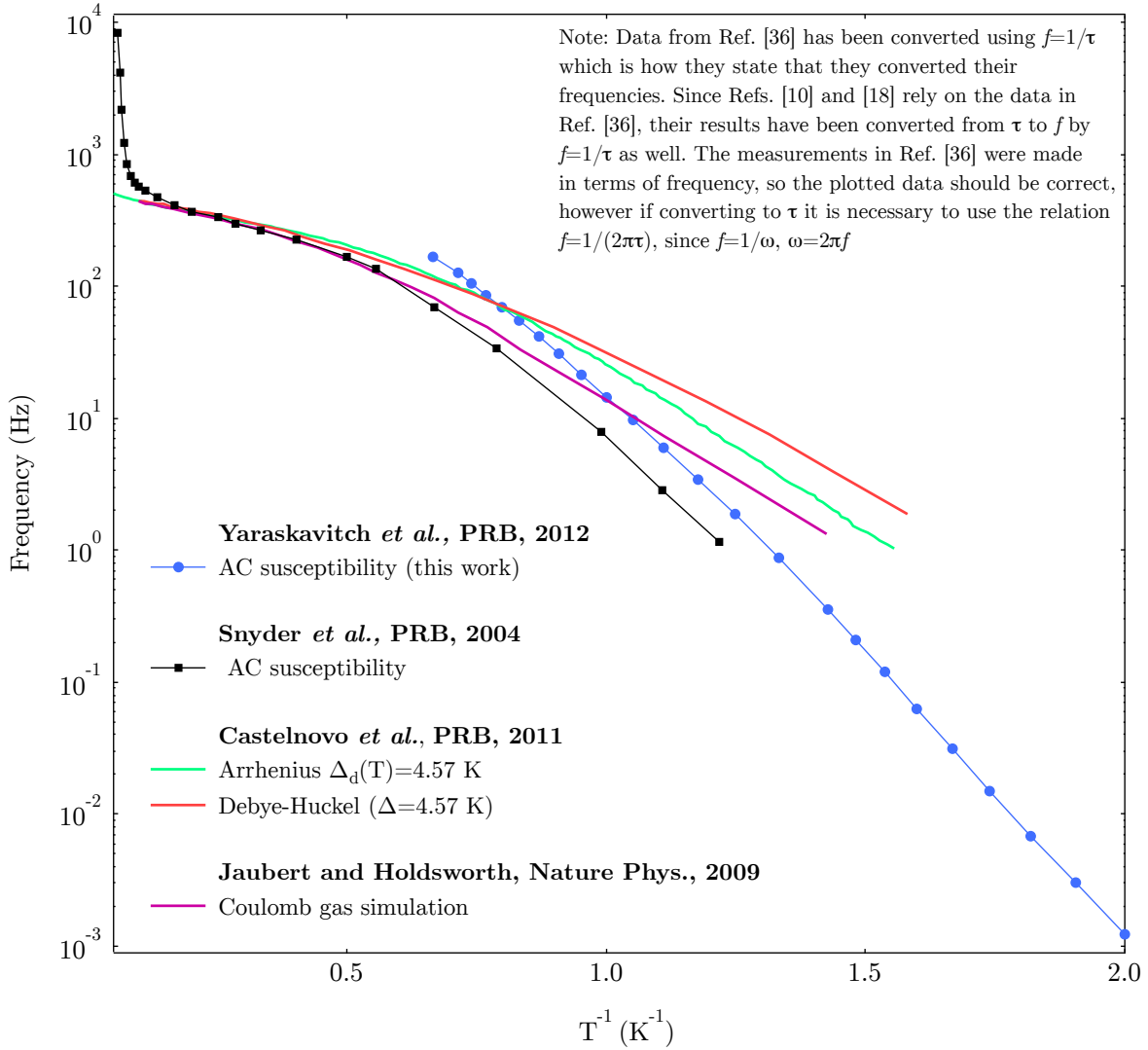


Figure 2.5: Plots of relaxation frequency versus inverse temperature comparing theory and simulation to ac susceptibility data. AC susceptibility data from Ref. [36] (black squares) deviates from theory and simulation at low temperature. AC susceptibility data from Ref. [8] (blue circles) also deviates from theory and simulation at low temperature. Neither the dressed monopole Arrhenius law (light green solid line) or the Debye-Hückel approximation (red solid line) from Ref. [18] capture the low temperature dynamics observed in ac susceptibility measurements of  $\text{Dy}_2\text{Ti}_2\text{O}_7$ . Simulated dynamics from Ref. [10] (purple solid line) fail to capture the measured dynamics as well.

said to be valid in the temperature regime of  $0.07 \text{ K} < T < 0.3 \text{ K}$ , where Onsager's theory is valid. There has been some controversy concerning this result. Dunsiger *et al.* [7] claim that based on the type of muon spin rotation measurements performed in Ref. [5], monopole signatures would be unobservable. Dunsiger *et al.* go on to show a signal originating from their Ag sample holder which looks nearly identical to the signal observed in Ref. [5].

Giblin *et al.* built on Ref. [5], by moving on to measuring magnetic current in  $\text{Dy}_2\text{Ti}_2\text{O}_7$ . [6] In this work, the authors apply a small (1-5 Oe) magnetic field parallel to the [100] crystal axis and observe the decay of, what they describe as, the induced monopole separation once the field is removed. They used a copper electromagnet to apply the magnetic field and a dc SQUID to measure the magnetization of the sample. Giblin *et al.* performed their measurements on a He-3 cryostat. They used the following Onsager-Wien dissociation equations to relate their measurements to monopole theory [37]:

$$\begin{aligned} \frac{d\Delta n_f(t)}{dt} &= k_D \Delta \tilde{n}_b(t) - 2K^{-1} k_D n_f^{\text{eq}} \Delta n_f(t) \\ \frac{d\Delta \tilde{n}_b(t)}{dt} &= -(k_{Or} + k_D) \Delta \tilde{n}_b(t) + 2K^{-1} k_D n_f^{\text{eq}} \Delta n_f(t) \end{aligned} \quad (2.3)$$

where  $\tilde{n}_b(t)$  and  $n_f(t)$  are the concentrations of bound and free monopoles.  $k_{Or}$  is the rate constant for orientation of dipoles and  $k_D$  is the rate constant for dissociation of bound pairs.  $K$  is the equilibrium constant for the reaction. The concentrations of bound and free monopoles can be related to the magnetic moment to lowest order and by making some approximations, discussed in detail in Ref. [6]. Fig. 2.6 contains the data presented in Ref. [6], which are decay curves of the magnetic moment of the sample of  $\text{Dy}_2\text{Ti}_2\text{O}_7$  once the applied field has been removed. The two coupled differential equations (2.3) are solved numerically, by Giblin *et al.*, with initial conditions set during the time that the field is applied. The experimentally measured decay of the magnetic moment density is then fit to the solutions  $\mu_{tot}(t) = \mu_b(t) + \mu_f(t)$ . The fits determine the parameters ( $k_D$ ,  $k_{Or}$ ,  $n_f^{\text{eq}} = \exp(-T_f/T)$ ,  $n_b^{\text{eq}} = \exp(-T_b/T)$ ), where  $T_f$  and  $T_b$  are the free and bound charge creation energies, respectively. Giblin *et al.* claim that the energy scales obtained from these fits at 360 mK are in excellent agreement with theory. The Wien-Onsager dissociation model does not fit to the data at 550 mK or 700 mK. However, it is stated that the length scale conditions for the validity of Onsager-Wien dissociation are not satisfied at these temperatures.

Finally, in Ref. [6], the SQUID measurements are related to the muon spin rotation measurements presented in Ref. [5], by plotting  $\kappa(B)/\kappa(0)$  versus  $b$ , where  $\kappa(B)/\kappa(0) = 1 + b/2 + b^2/12 + \dots$  in the Onsager-Wien model and  $b$  is determined experimentally since  $b = \mu_o Q^3 B / 8\pi k^2 T^2$ . While the data both lie along the path of  $\kappa(B)/\kappa(0) = 1 + b/2 +$

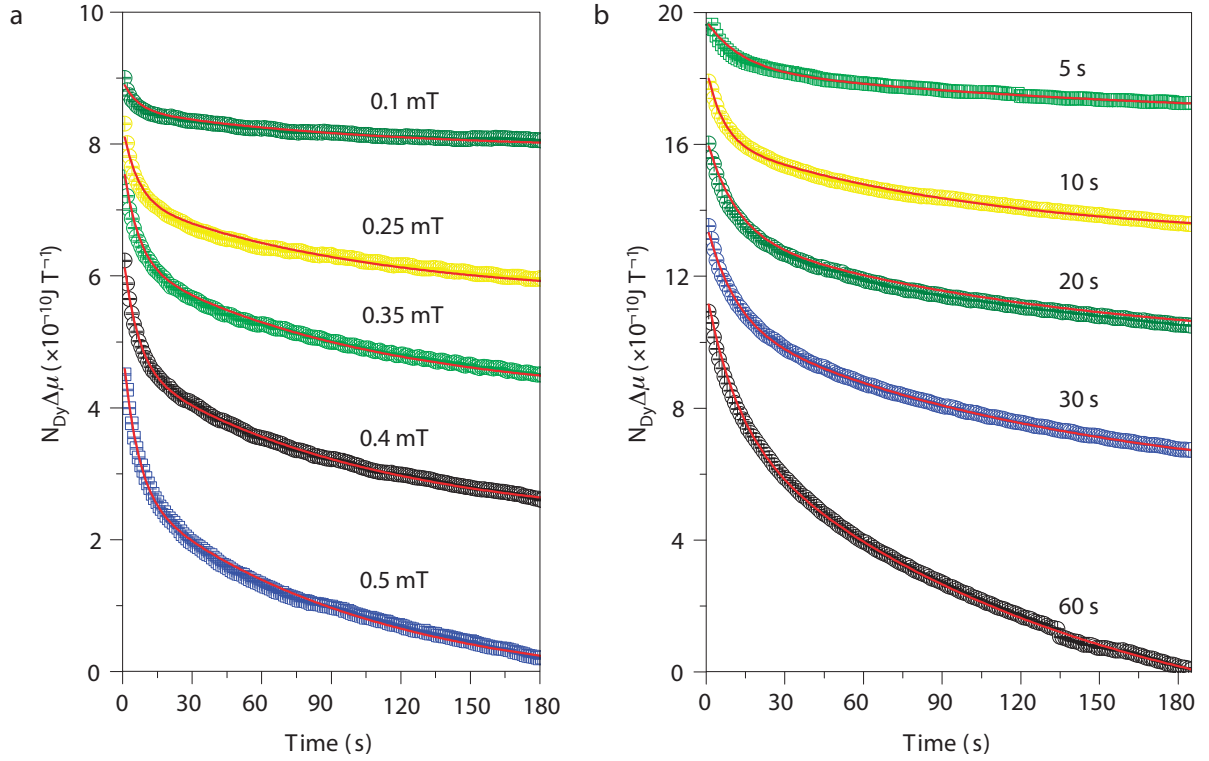


Figure 2.6: The decay of the magnetic moment density of  $\text{Dy}_2\text{Ti}_2\text{O}_7$  after the removal of the applied field. The colourful markers are the data measured by the SQUID and the red line is the fit to the Onsager-Wien model. (a) The field was applied for a charging time of  $t_o = 10 \text{ s}$  with various field strengths. (b) A field of 5 Oe was applied for various charging times,  $t_o$ . Figure is from Ref. [6].



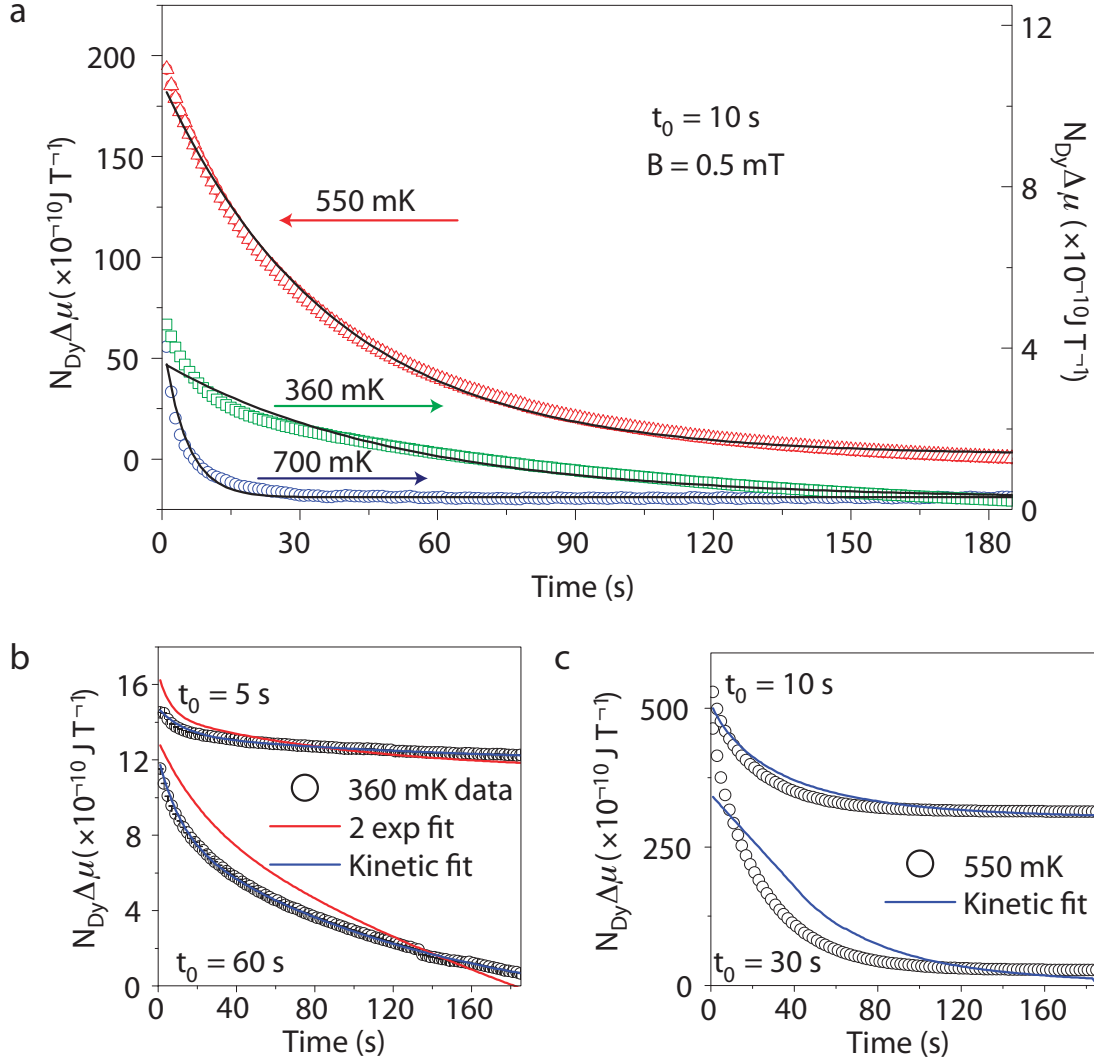


Figure 2.7: The decay of the magnetic moment density of  $\text{Dy}_2\text{Ti}_2\text{O}_7$  after the removal of the applied field for three temperatures. (a) The 5 Oe field was applied for a charging time of  $t_o = 10 \text{ s}$  at temperatures: 360 mK, 550 mK, 700 mK and the decays were fit to the Onsager-Wien dissociation solutions to Equation 2.3 (kinetic fit). (b) A field of 5 Oe was applied for  $t_o = 5 \text{ s}$  and  $t_o = 60 \text{ s}$  at 360 mK. A fit to a double exponential is compared to a fit to the Onsager-Wien solutions (kinetic fit). (c) A field of 5 Oe was applied for  $t_o = 10 \text{ s}$  and  $t_o = 30 \text{ s}$  at 550 mK. The data does not appear to fit the Onsager-Wien solutions. Figure is from Ref. [6].

$b^2/12+\dots$ , the interpretation of data from Ref. [5] is under question by Dunsiger *et al.* [7]. By looking at Fig. 2.6, one can see that the decay of the magnetic moment has not equilibrated by  $t = 180$  s. While Giblin *et al.* state that Onsager-Wien dissociation can describe dissociation and recombination of monopoles at short time scales, they state that there are two relaxations at 0.36 K, one about 10 s and the other a few hundred seconds. Considering that they state that the zero of the magnetic moment is a fit parameter, it would seem that they did not wait for the magnetic moment to equilibrate after removal of the field.[6] Being that they did not wait for equilibration, it seems strange to make statements about visible relaxations. The observation of two relaxations (10 s and a few hundred seconds) is contrary to what is seen with ac susceptibility at 360 mK and will be discussed further in the following section. The main results presented in this thesis will attempt to consolidate the discrepancy between dc magnetization measurements and ac susceptibility measurements.

## 2.5 Low Temperature Relaxation Times

In this section, previous ac susceptibility measurements, thermal measurements, and magnetization measurements will be compared and discussed in the context of relaxation times. It is of interest to determine the nature of spin ice dynamics down to the lowest temperatures. There is a characteristic time scale associated with any microscopic process. The evolution of that time scale with temperature gives insight towards the energy scales involved, as well as the nature of its freezing. A standard way of obtaining this information about a magnetic material is to perform ac susceptibility measurements. By applying a small ac magnetic field to a sample containing spins, one can measure how well the spins are able to track the field using lock-in detection. AC susceptibility has an in-phase and out-of-phase component[38],

$$\chi(\omega) = \chi'(\omega) - i\chi''(\omega) \quad (2.4)$$

In the case of a single Debye-type relaxation components are related by[38],

$$\begin{aligned} \chi'(\omega) &= \chi_s + \frac{\chi_T - \chi_s}{1 + (\omega\tau)^2} \\ \chi''(\omega) &= \omega\tau \left( \frac{\chi_T - \chi_s}{1 + (\omega\tau)^2} \right) \end{aligned} \quad (2.5)$$

where  $\chi_T$  is the dc susceptibility (limit of  $\omega \rightarrow 0$ ) at the temperature  $T$  and  $\chi_s$  is the susceptibility in the limit of  $\omega \rightarrow \infty$ . The maximum of the out of phase component of the susceptibility can be used to determine the relaxation time  $\tau$ , since  $1 = \omega\tau$  when  $\chi''$  is at a maximum. Typically either the temperature is fixed and the frequency is scanned or the frequency is fixed and temperature is scanned. The peak in  $\chi''$  as a function of frequency will move as the temperature is changed and vice versa. Hence, by performing these measurements, the relaxation frequency or time can be determined and related to temperature.

As mentioned in an earlier section, several ac susceptibility measurements have been made by different groups.[36, 39, 40, 41] Recent measurements by Matsuhira *et al.* will be presented in the results section as this work was done at the same time as this project was being carried out. Fig. 2.8 is a plot of relaxation frequency versus inverse temperature containing previous ac susceptibility data.[40, 41] The temperature scans performed by Matsuhira *et al.* are a less reliable way to determine relaxation, since the spectra are less symmetric than the spectra of the frequency scans and therefore the true peak is more difficult to determine. An Arrhenius relaxation indicates that there is a temperature-activated process whose relaxation time as a function of temperature is governed by the equation

$\tau(T) = \tau_o \exp(\Delta E/T)$ , or equivalently,  $f(T) = f_o \exp(-\Delta E/T)$ , where  $\Delta E$  is the energy barrier (divided by the Boltzmann constant so that it is in units of Kelvin) to relaxation of the process and  $f_o = 1/2\pi\tau_o$  is the attempt rate of traversing the energy barrier[10, 11]. There are three general regimes belonging to the relaxation of spin ice materials. The first regime is the high temperature regime which is described by an Arrhenius law with an activation energy of  $\sim 200$  K for  $\text{Dy}_2\text{Ti}_2\text{O}_7$  ( $\sim 290$  K for  $\text{Ho}_2\text{Ti}_2\text{O}_7$ ) [40, 42], where transitions to higher crystal field states set the energy barrier to relaxation. The next regime is from about 12 K to 2 K, and is referred to as the “quasi-plateau” regime. It is well-described by an Arrhenius law with an energy barrier of  $2 J_{\text{eff}}$ , which is believed to be due to quantum tunnelling processes, along with some monopole excitations.[10] The third regime (below 2 K) is possibly the least understood. The lowest temperature relaxation frequencies obtained by ac susceptibility experiments prior to the work in Ref. [8] hint at an Arrhenius regime as can be seen in Fig. 2.8, however there is not enough data to confirm or quantify this. It should be firmly noted that Jaubert and Holdsworth were able to capture the crossover accurately from the quasi-plateau regime to about 1K by simulating a Coulomb gas of monopoles.[10, 11]

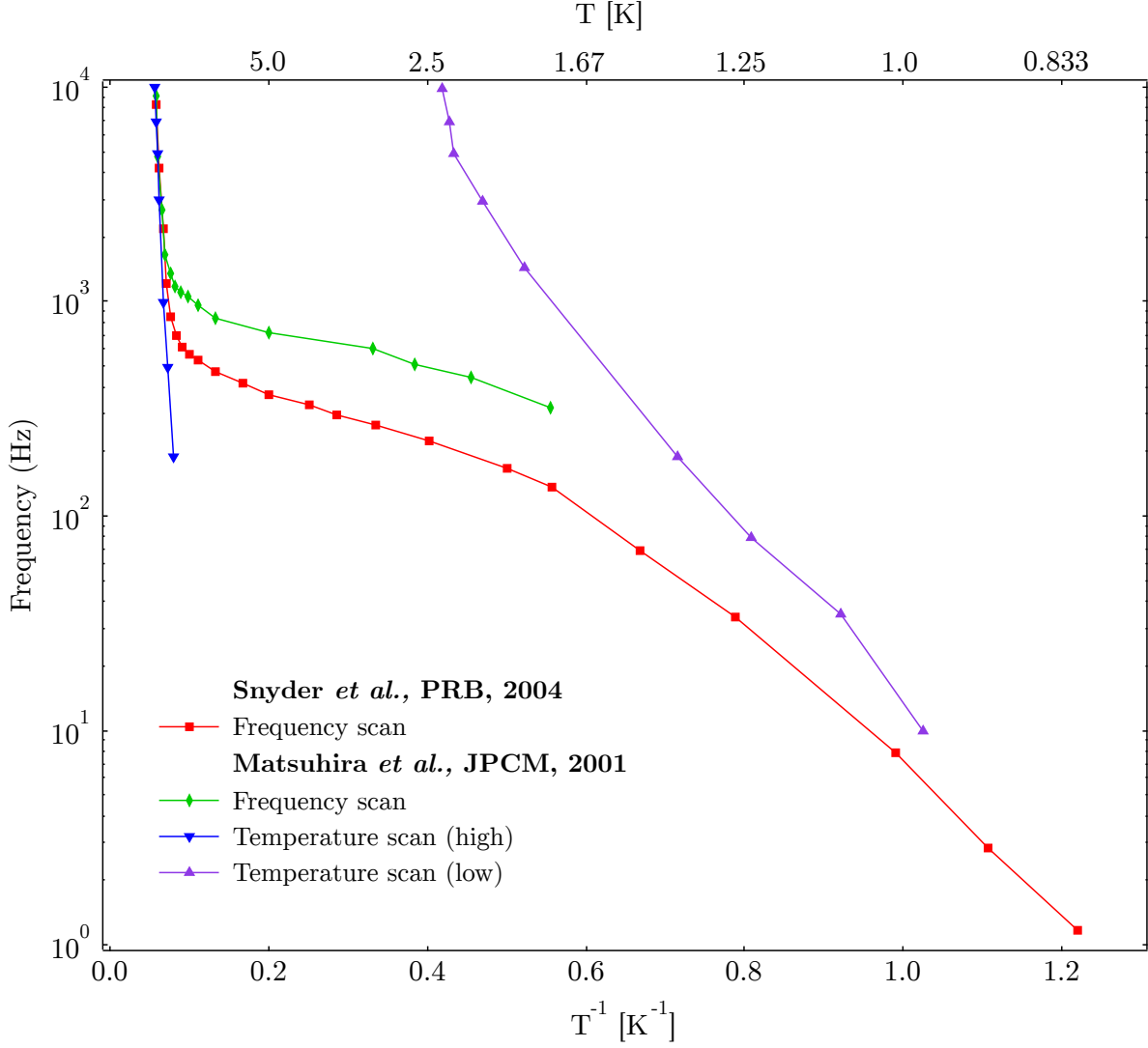


Figure 2.8: Relaxation frequencies obtained from previous ac susceptibility work[40, 42, 36] plotted as frequency (log scale) versus inverse temperature. The frequency scans produce a more reliable result, as their absorption spectra are more symmetric, making it easier to determine the maximum. The relaxation enters the “quasi-plateau” region below 15 K ( $0.066 \text{ K}^{-1}$  and above) where quantum tunneling processes are dominant and the dynamics are well-described by an Arrhenius law with energy barrier  $2J_{\text{eff}}$ , the energy cost for the creation of two monopoles when sufficient screening is present. Relaxation below 2 K ( $0.5 \text{ K}^{-1}$  and up), up until recently, had not been explored or understood adequately.

More recent studies of  $\text{Dy}_2\text{Ti}_2\text{O}_7$  and  $\text{Ho}_2\text{Ti}_2\text{O}_7$  using ac susceptibility [8, 20] were published in the last year and the resulting relaxation times are plotted in Fig. 2.9.

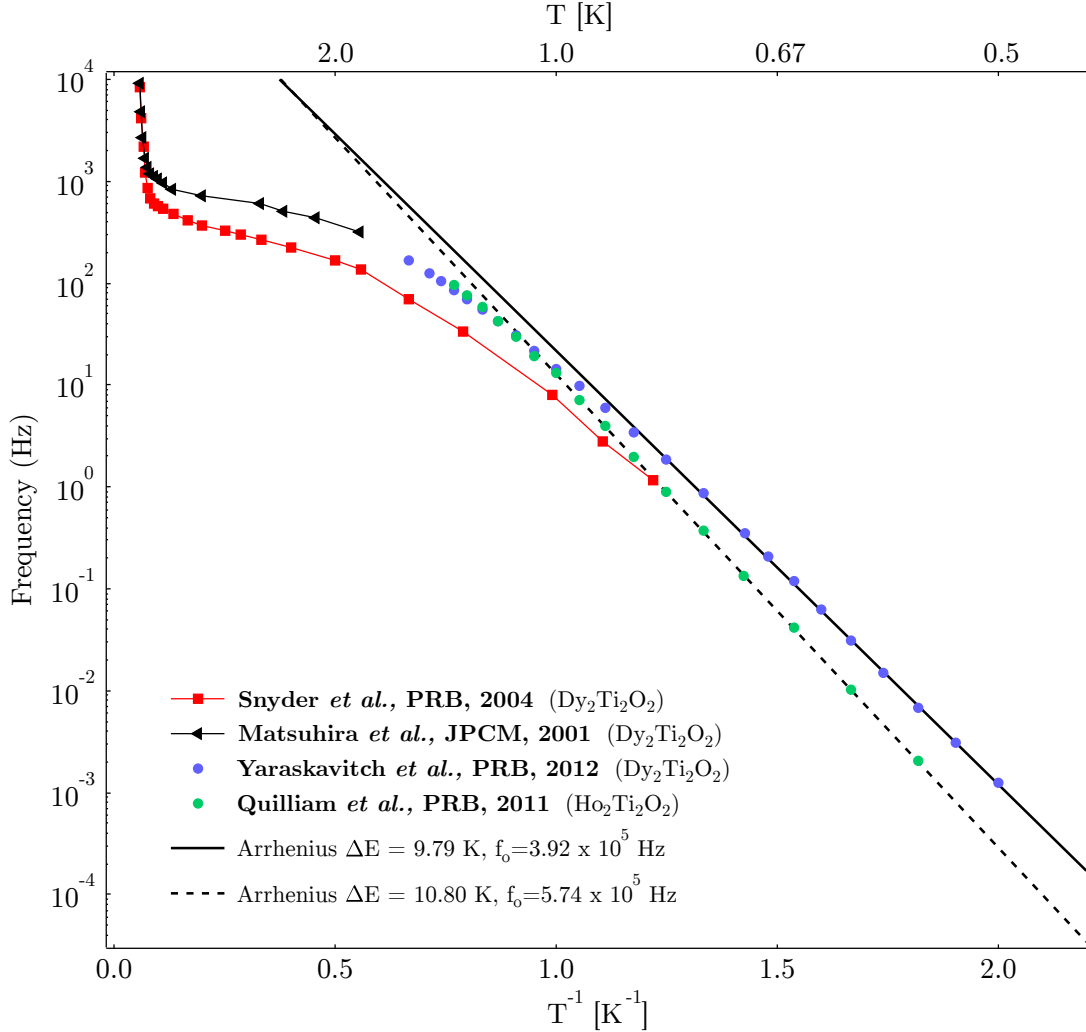


Figure 2.9: Relaxation frequencies from older[36, 40] and more recent[8] ac susceptibility results. The newer data from Refs. [20, 8] shows Arrhenius behaviour below  $\sim 1$  K with energy barriers of 9.79 K ( $\sim 9 J_{\text{eff}}$ ) for  $\text{Dy}_2\text{Ti}_2\text{O}_7$ , 10.80 K ( $\sim 6 J_{\text{eff}}$ ) for  $\text{Ho}_2\text{Ti}_2\text{O}_7$ .

The measurements go to three orders of magnitude lower in frequency than earlier measurements and find Arrhenius temperature-activated relaxation below temperatures of

$\sim 1$  K with energy barriers of 9.79 K (for  $\text{Dy}_2\text{Ti}_2\text{O}_7$ ) and 10.80 K (for  $\text{Ho}_2\text{Ti}_2\text{O}_7$ ). These values are close to  $9 J_{\text{eff}}$  and  $6 J_{\text{eff}}$ , respectively. This more recent ac susceptibility [8, 43] appears to resolve the earlier ac susceptibility results [36, 39, 40, 44] by performing a thorough demagnetization correction and going to lower frequency. Matsuhira *et al.* may have performed a demagnetization correction, however the details of how it was carried out are not explicitly stated. [39, 40] Snyder *et al.* do not mention any demagnetization. [36, 41] The shift in frequency between Ref. [8] and Ref. [36] may be due to a lack of demagnetization correction in the work of Snyder *et al.* Also, in Snyder *et al.*'s conversion from frequency to time constant  $\tau$ , they explicitly make the statement  $\tau = 1/f$  [36], when in fact  $\tau = 1/\omega = 1/2\pi f$ . In this thesis, the data of Snyder *et al.* shown in terms of characteristic frequencies is converted using  $\tau = 1/f$ , which is also the case for Refs. [10, 11, 18] as they use the experimental data from Ref. [36] to anchor their theoretical findings. When the relaxations are plotted in terms of  $\tau(T)$  in this thesis, the frequencies are converted using  $\tau = 1/(2\pi f)$ , which should correct for the original  $2\pi$  error. While the discrepancy between experimental ac susceptibility results may be somewhat settled, the remaining problem is the disagreement between current monopole theory, ac susceptibility, and thermal measurements. Thus far, there is no theory that can explain the energy barriers for  $\text{Ho}_2\text{Ti}_2\text{O}_7$  and  $\text{Dy}_2\text{Ti}_2\text{O}_7$  at low temperature.

In Fig. 2.10, magnetocaloric measurements [45] and thermal relaxation measurements [33] of the relaxation time are plotted alongside the latest ac susceptibility results [8] for  $\text{Dy}_2\text{Ti}_2\text{O}_7$ . The thermal measurements show a flattening of temperature dependence starting at about 500 mK. The magnetocaloric measurements seem to independently qualitatively confirm this flattening. The work of Klemke *et al.* claim that thermodynamic field theory can explain the behaviour that they observe. [33] Klemke *et al.* perform experiments on a [110] oriented sample of  $\text{Dy}_2\text{Ti}_2\text{O}_7$  and consider two relaxations, emanating from the two  $\alpha$  and  $\beta$  chains of spins that couple differently to the applied magnetic field when spin ice is oriented this way. [12, 46] They observe two relaxation frequencies and fit them both to a function of the form  $b = \bar{b} + A \exp([E + \epsilon]/k_B T)$ , where  $\bar{b}$  is the result of strong screening effects, the exponential  $e^{\epsilon/k_B T}$  represents the weakening of these effects, and  $E/k_B$  is the barrier to relaxation. Klemke *et al.* report an energy barrier of  $E/k_B = 8.36$  K for both relaxations  $\alpha$  and  $\beta$  and explain it by attributing it to the cost of the creation of two monopoles plus their Coulomb potential energy. They cite Castelnovo *et al.* in Ref. [18] for theoretical values of monopole creation energy and Coulomb potential energy. While this appears convincing, it should be noted that in Ref. [18], it is stated that at low temperature ( $T < 500$  mK), monopole separation and screening length diverge and standard Arrhenius behaviour is expected, which would agree qualitatively with the ac susceptibility results in Refs. [8, 20]. In addition, the numbers that are provided for the breakdown of

the barrier energy in Ref. [33] are chosen some what arbitrarily, as there is much discussion of different energy barriers in Ref. [18].

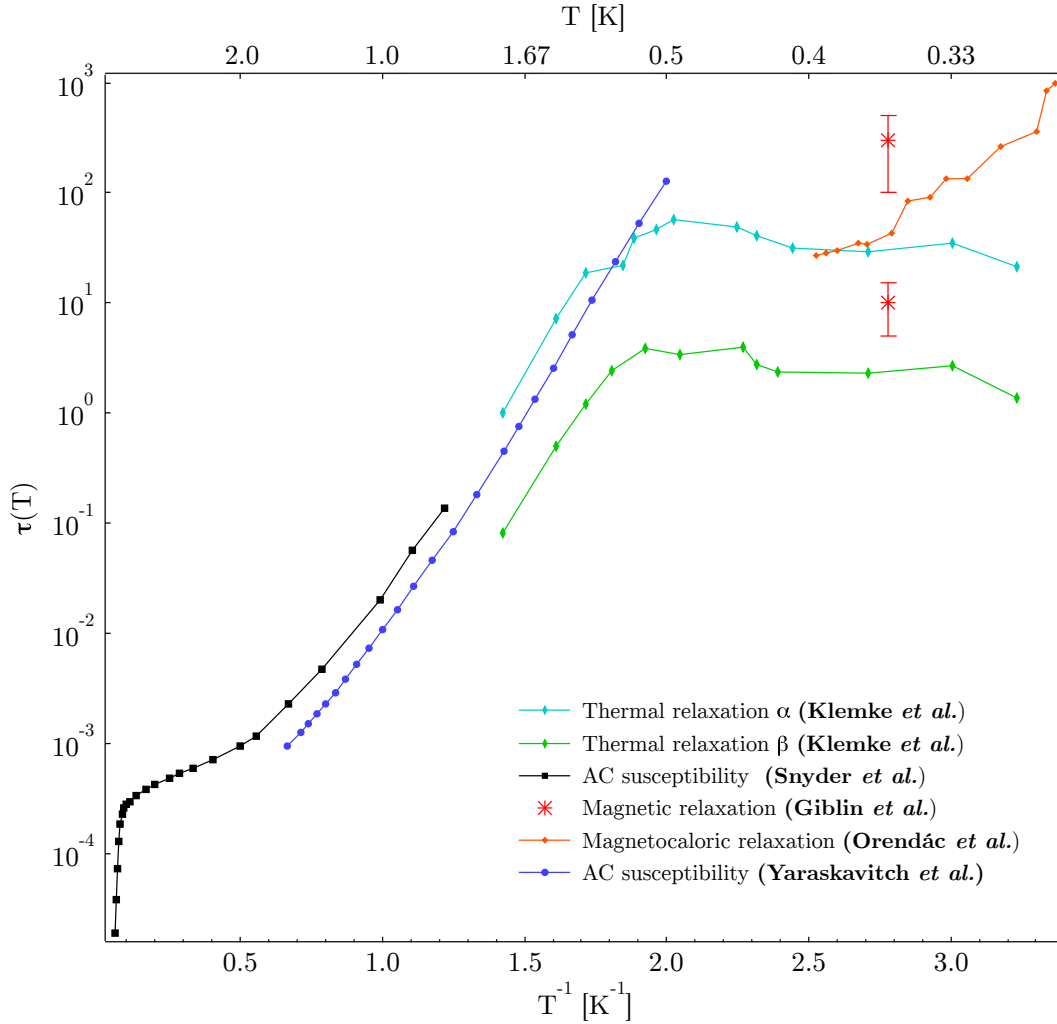


Figure 2.10: Comparison of relaxation times obtained from ac susceptibility, thermal relaxation, and magnetocaloric measurements. While the ac susceptibility measurements[8, 20, 36] show a temperature-activated Arrhenius behaviour at low temperature, the magnetocaloric[45] and thermal relaxation measurements[33] show a flattening of temperature dependence below 500 mK. Also plotted on this graph are the relaxation times that correspond to the time scales reported in Ref.[6] at 360 mK.



Also plotted in Fig. 2.10 are the relaxation times observed by Giblin *et al.* at 0.36 K.[6] The two relaxation times they observe are not visible in the ac susceptibility measurements from Ref. [8]. Giblin *et al.* use applied magnetic fields with magnitudes of 1 to 5 Oe and claim to be in the low field linear regime, where the magnetic response is linearly dependent on the applied field. The ac susceptibility measurements in Ref. [8] were made with an ac field of an amplitude of 6 mOe. Therefore, if Giblin *et al.* were in the linear response regime and observed relaxations at 360 mK of 10 s and a few hundred seconds these relaxations would correspond to frequencies of 0.016 Hz and 0.0016-0.00053 Hz that would be detectable and manifest themselves as peaks in the out-of-phase spectra in ac susceptibility measurements. No peaks in the  $\chi''(f)$  spectrum are observed in the range of  $10^{-3}$  Hz to  $10^4$  Hz at 0.36 K.[8]

The major themes that emerge from previous works discussed in this chapter are: Arrhenius behaviour at low temperature, two relaxations instead of a single relaxation as mentioned in different contexts by both Ref. [6] and Ref. [33], and differences in ac and dc magnetization measurements. The goal of this thesis project was to design a new magnetometer and perform ac susceptibility measurements on  $\text{Dy}_2\text{Ti}_2\text{O}_7$  in order to test its performance and perform new dc magnetization measurements on  $\text{Dy}_2\text{Ti}_2\text{O}_7$ .



# Chapter 3

## Experimental Details

### 3.1 DC SQUID Background

Superconducting quantum interference devices (SQUIDs) have been the most sensitive magnetometer devices for decades.[47] These devices take advantage of the Josephson effect[48] and flux quantization to provide a measurement resolution on the order of a few micro-flux quanta,  $\mu\phi_0$ . In this section a brief introduction of how a dc SQUID works will be presented. A dc SQUID, shown in Fig. 3.1 is comprised of two Josephson junctions connected in parallel, which form an otherwise closed superconducting loop.

There are different types of Josephson junctions, however the junctions in the SQUID that is used in this project are superconductor-insulator-superconductor (SIS) junctions. The junction consists of two superconducting interfaces (typically having an area of about  $1 \times 1 \mu m$ ) which are separated by a thin (few nanometer) insulating barrier. It turns out that if this barrier is biased with a small direct current, the junction will be superconducting and will tunnel Cooper pairs across the barrier. Once the bias current is increased past a certain critical value,  $I_C$ , a voltage will develop across the junction. The model used to describe the behaviour of most SIS Josephson junctions is called the resistively capacitively shunted junction (RCSJ) model. All junctions have a certain capacitance, as they have geometry similar to capacitor plates. As well, they will have a resistance, however, usually a resistor will be placed in parallel with each junction in order to optimize the junction performance, which is referred to as the shunt resistor. The RCSJ model can be more intuitively viewed as a particle moving down a tilted washboard. The details of this model can be found in Ref. [47].

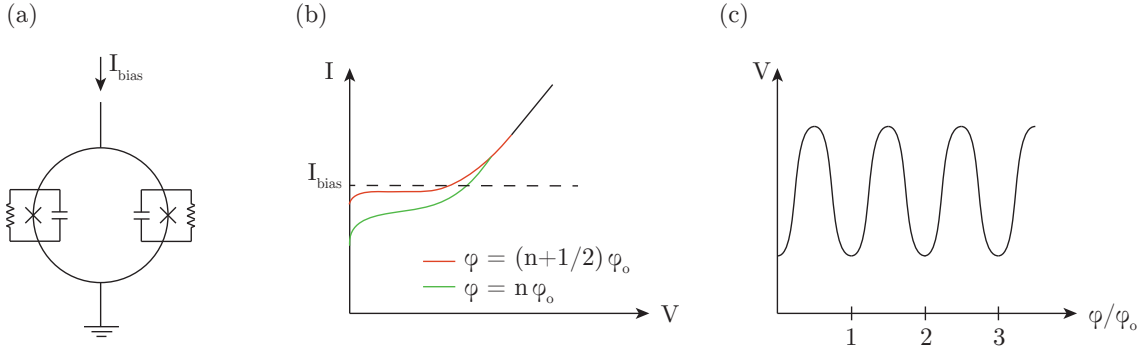


Figure 3.1: The operation of a dc SQUID. (a) Two identical resistively capacitively shunted junctions, in parallel, are biased with a current source  $I_{\text{bias}}$ , such that  $I_{\text{bias}} > 2I_C$ , where  $I_C$  represents the critical current of each of the junctions. (b) A magnetic flux that threads the SQUID loop will cause the I-V characteristic to shift continuously between the red and green curves, as the total magnetic flux threading the loop will remain quantized in integer multiples of flux quanta, which is a phenomenon of closed superconducting loops.[47] If  $\phi \neq n\phi_0$  then a current will be generated around the loop in order to quantize the total flux, which changes the effective critical currents of the junctions and shifts the I-V characteristic accordingly, causing the operating point set by the bias current to trace out an oscillating voltage. (c) The  $V$ - $\phi$  curve is a sinusoidal function. One can use phase sensitive detection in a feedback circuit to sit on a point on the curve, which is known as a flux-locked loop configuration.

In a dc SQUID two identical SIS Josephson junctions are in parallel, with all wiring made from a superconductor, in this case niobium. The SQUID must be biased with a dc current that is greater than twice the critical current,  $2I_C$ , of each junction. The bias current splits equally to each of the identical junctions causing them to operate in their voltage regime. If the magnetic flux threading the loop that connects the junctions in parallel is below half a flux quantum,  $\phi_0 = h/(2e)$ , a current will be generated around the loop in order to bring the total flux through the loop back to zero. This is a result of flux quantization that occurs in closed loops of superconductors.[47] The generated (quantizing) current will effectively lower the critical current in one of the junctions and raise the critical current by the same amount in the other junction. As the applied magnetic flux is raised past half a flux quantum, the current generated due to flux quantization will switch directions and bring the total flux up to 1 flux quantum. This pattern will continue

as the applied magnetic flux is continuously increased. The resultant voltage across the device is a sinusoidal function of the applied magnetic flux. These concepts are illustrated in Fig. 3.1. In practice, a flux locked loop (FLL) circuit is used to linearize the flux to voltage relationship. FLL circuitry uses phase sensitive detection to detect small changes in voltage. The information about the change is fed to a feedback coil, which applies an equal and opposite flux to the SQUID in order to move the operating point of the SQUID back to where it was before the small change. The voltage across the current limiting resistor leading to the feedback coil is the signal that is read out. It is directly proportional to the magnetic flux that is applied to the SQUID, which is the quantity of interest.

SQUIDS are used in many applications, such as aerial resource detection, magnetic resonance imaging research, and nuclear magnetic resonance material research. The conventional method for detecting magnetic fields is measuring the induced EMF through a coil placed in the field of interest. Many of the fields being detected are of sinusoidal nature  $\sim \cos \omega t$ . Faraday's law states that the induced EMF is proportional  $\partial\phi/\partial t$ , so in the case of a sinusoid,  $EMF \sim \omega \sin \omega t$ . When detecting high frequency fields, this implies that the readout signal is growing with frequency, which is advantageous. However, when detecting slowly varying or low frequency signals, the frequency dependence of the readout signal becomes a limitation. SQUIDS have a flat frequency response, meaning there is no loss of signal with varying frequency. This is especially important in low frequency measurements, where the SQUID's performance is better than the conventional coil method. DC SQUIDS do have a cut off frequency, which is dependent on components in the FLL circuit, specifically the value of the feedback resistor being used.

## 3.2 The DC SQUID Gradiometer

Because SQUID detection is such a sensitive method of detecting magnetic fields, these devices are susceptible to noise issues. Intrinsic noise comes mainly from the Nyquist noise (current noise) of the shunt resistor and is proportional to  $\sqrt{T/R}$ .<sup>[47]</sup> One way to reduce the intrinsic noise of a SQUID would be to raise the shunt resistance. However, external noise sources are common to almost any environment. Examples of noise common to almost any lab environment may include the magnetic field produced from the operation of an elevator, the transformers on the power adapters of telephones, or even Earth's field. Sources like these can easily be picked up by SQUIDs and as a result they can skew or completely shadow the magnetic signal of interest. One way to reduce noise is to introduce magnetic shielding, such as mu-metal shielding or superconducting shields. Shielding is effective, however finding the space to put these shields if mounting an experiment to the mixing chamber of dilution fridge can be challenging or impossible. Mu-metal shielding also tends to be rather expensive. Alternatively, there is a clever loop configuration that can be used in the fabrication of a SQUID in order to greatly reduce external noise.

A first order SQUID gradiometer detects the difference in magnetic flux between two loops. This is achieved by making a figure-8 shaped SQUID. This is visualized in Fig. 3.2, where two loops of equal area are counter-wound from the same mother SQUID loop. One can imagine that if a spatially constant magnetic field were applied to the device, an equal and opposite current would be induced in each sub-loop, meaning that overall, the entire SQUID loop would detect no magnetic flux. The devices are typically only micrometers in size, so any magnetic noise source that is far enough away would appear as a spatially constant field relative to the difference in space between the coils and would therefore be screened from the measurement. The key to making an actual measurement with one of these devices is to place the sample of interest in one of the loops, or inductively coupling a sample to one of the loops, such that the SQUID will detect changes in the sample's magnetization.

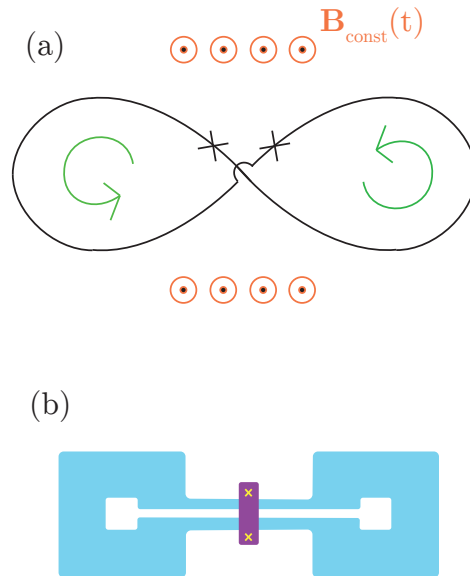


Figure 3.2: The SQUID gradiometer. (a) A schematic sketch of the figure-8 configuration of a first order gradiometer, illustrating the directionality of the induced current in the loops from a spatially constant external field that may vary with time. Junctions have been enlarged and are realistically symmetrically placed about the centre of the device. (b) A schematic of the actual shape of the SQUID gradiometer. The figure-8 winding is achieved through clever photolithographic layering and insulating barriers that contain windows.

The SQUID used for this project was fabricated by *ezSQUID* in Germany. The SQUID is made of niobium and has two aluminum oxide junctions of about  $1 \times 1 \mu\text{m}$  area and 2-3 nm thickness. The SQUID, itself, is a first order gradiometer which was fabricated using photolithographic techniques. There are two pick-up coils that form superconducting flux transformers with input coils, which are all lithographically patterned onto the silicon that the SQUID sits on. Fig. 3.3 contains a schematic of the gradiometer. One of the challenges faced throughout the course of this project was to be able to make a hole in the silicon chip in order to place the needle shaped sample directly in the middle of the pick-up coil. The motivation behind this geometric configuration is that one wants the pick-up coil to be tightly coupled to the most uniformly magnetized portion of the sample. In a magnetic sample that is not infinitely long there are fringe effects where the magnetization of the

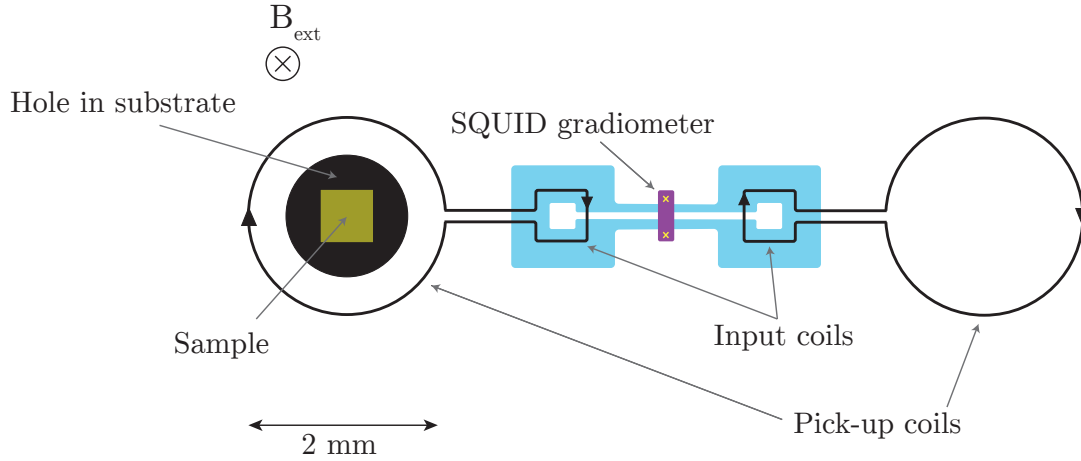


Figure 3.3: The schematic of the SQUID gradiometer, pick-up and input coils. Note: the SQUID is not drawn to scale and has been enlarged to emphasize the junctions and general shape.

sample at the ends is no longer representative of the average bulk magnetization. However, if the long axis of the sample is sufficiently larger than the short axes, and a single loop is placed in the middle of the sample, as in this case, the magnetization of the sample approaches a pure magnetic dipole.[49] Several techniques were employed to attempt to drill a hole into silicon, however, due to the directionality of the structure of silicon and its tendency to cleave, this mechanical feat was not possible. Laser ablation was performed by *Questech Services Co.* in Garland, Texas, to create a 1 mm diameter hole in the centre of one of the pick-up coils. Fig. 3.4 contains microscopic images of one of the holes. The pick-up loops on the device used in this project, have another coil patterned directly around each of the pick-up coils, so that if desired, these could be used as the excitation coils for the measurement. In this project, one of these coils was used as the feedback coil in the FLL circuit.



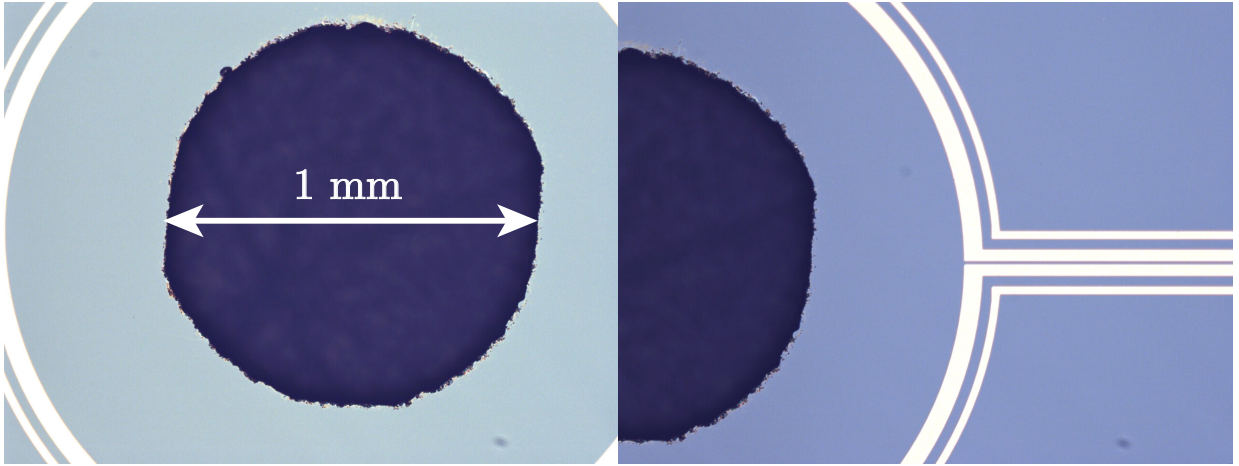


Figure 3.4: Microscopic images of the 1 mm hole that was made using laser ablation in the centre of one of the pick-up coils of the SQUID gradiometer. The needle-shaped sample of interest sits in the hole so that the sample is centred with respect to the pick-up coil.

### 3.3 Magnetometer Design

A magnetometer was designed, constructed, and used to make magnetic measurements over the course of this project. The main goals behind developing the new measurement tool were to improve the bandwidth of operation, reduce the impact of edge effects of the sample's magnetization, use a smaller coil setup for the possibility of multiplexing[50], and to get a SQUID measurement operating on the second dilution fridge. One of the SQUIDs discussed in the previous section was used to make a magnetometer. In order to perform ac susceptibility measurements and dc magnetization measurements, it was necessary to be able to apply a magnetic field to the sample and simultaneously be able to measure the sample's magnetization. This was achieved by wrapping a 2 cm diameter coil which served as the excitation coil. The SQUID gradiometer was placed directly in the centre of the excitation coil so that, while the the field from the excitation coil was applied to the sample, the SQUID was unable to detect it. Fig. 3.5 contains a 3-dimensional diagram of the magnetometer stage that was mounted to a dilution fridge and Fig. 3.6 contains two images of the magnetometer.

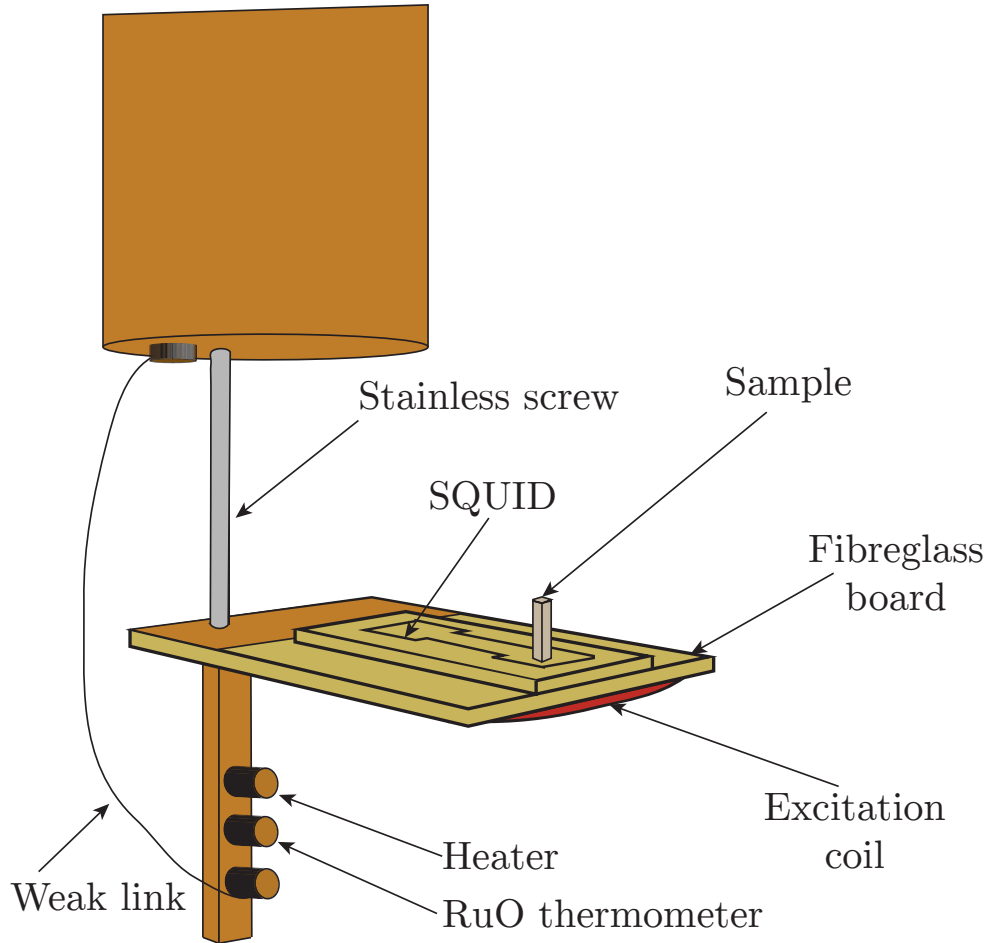


Figure 3.5: A drawing of the magnetometer experimental stage that is mounted on a dilution fridge. The SQUID is *GE*-varnished to a fibreglass board containing niobium electrode pads that the SQUID is wire-bonded to. The sample sits in one of the pick-up coils, within a hole through the silicon and within a drilled hole in the fibreglass and is fastened in place with *Apeizon* vacuum grease. An excitation coil, wound with single filamentary Ni-Cu-clad NbTi wire is screwed onto the bottom of the fibreglass board with nylon screws. The fibre glass board is thermally isolated from the mixing chamber above using a few inches of stainless steel screw so that a weak link can be used, along with a thermometer and heater, to temperature control the stage of the magnetometer. The fibreglass board has a layer of Cu foil glued onto part of it, where it meets the Cu rod below in order to make good thermal contact.

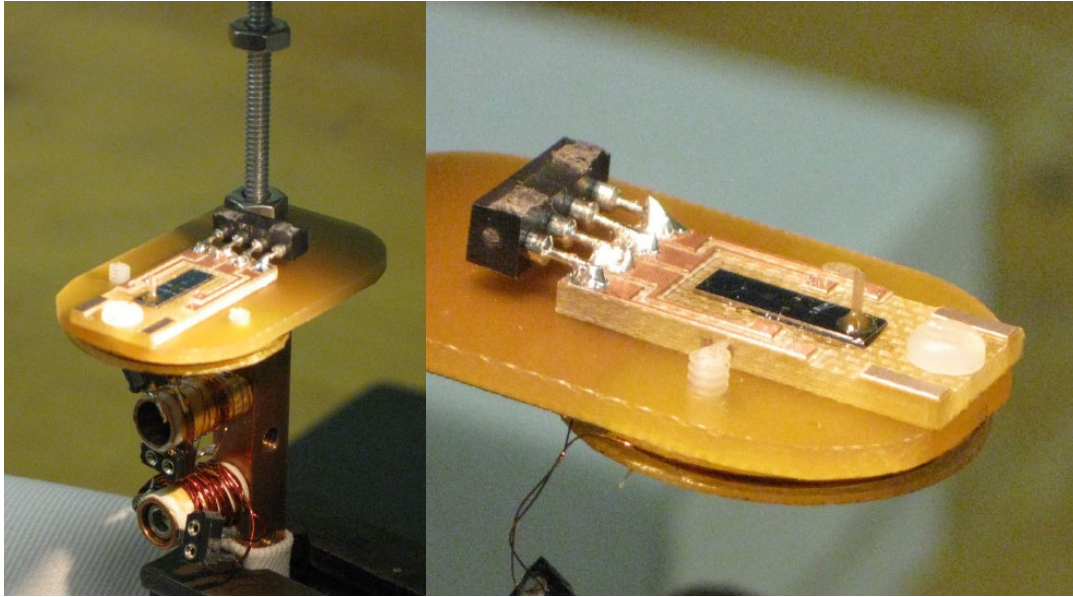


Figure 3.6: Two images of the magnetometer with a single crystal sample of  $\text{Dy}_2\text{Ti}_2\text{O}_7$  mounted to it.

The excitation coil was wound with 52 turns of nickel-copper clad NbTi single-filamentary wire. The reason for using a superconducting wire to wind the excitation coil was to avoid the possibility of resistive heat being transferred to the sample from the excitation coil, as good temperature control is extremely important in low temperature experiments. The excitation coil was connected to a twisted pair that runs up the fridge to the room temperature electronics. A current limiting resistor of  $10\text{ k}\Omega$  was placed at the voltage source of the excitation coil. Since the coil was not a Helmholtz coil, nor was its length much greater than its radius, the coil does not produce a spatially constant field. However, since the sample size is small, the field gradients are not expected to be large over the length of the sample. A future improvement to the system would be to design a Helmholtz excitation coil.

The magnetometer was thermally isolated from the mixing chamber of the fridge with a stainless steel screw, which is a poor thermal conductor. The SQUID and excitation coil were mounted to a fiberglass board, which was heat sunk to a copper post. The fiberglass board had copper foil glued to it, which was removed up to just before the point of contact with the copper post in order to improve the thermal contact. A  $10\text{ k}\Omega$  metal film resistor (heater) and  $10\text{ k}\Omega$  ruthenium oxide resistor (thermometer) were fastened to the copper

post. A weak link was connected from the mixing chamber to the copper post and PID control was used to set the temperature of the stage.

For ac susceptibility measurements, a *Stanford Research* SR830 lock-in amplifier was used to produce the excitation voltage, as well as, detect the in-phase and out-of-phase components of the FLL voltage of the SQUID. For the dc magnetization measurements, a voltage supply with a current limiting resistor was used to apply a current to the excitation coil on the magnetometer. The voltage source was controlled using a DAC which was connected to a computer. The same computer contained a *GAGEScope* PCI card which enabled the collection of the FLL voltage readout from the SQUID. Appendix B contains some details of the measurement challenges that were encountered, such as: mechanical vibrations, magnetic shielding, and backaction within the feedback configuration.

### 3.4 Sample Details

Two samples of  $\text{Dy}_2\text{Ti}_2\text{O}_7$  were studied. Both samples were cut from a single crystal grown at McMaster University using a floating image zone technique[51] with a growth rate of 6 mm/hr in 3 atm of  $\text{O}_2$ . Both samples were cut to have a needle-like geometry shown in Table 3.1. The long axis in sample A is aligned with the [100] crystal axis and the long axis in sample B is aligned with the [110] crystal axis.

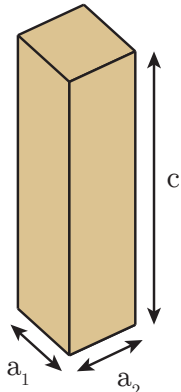
		Sample A [100]	Sample B [110]
	c	0.426	0.384
	$a_1$	0.053	0.044
	$a_2$	0.049	0.046

Table 3.1: Dimensions and crystal orientations of the samples (in cm).



# Chapter 4

## Results

### 4.1 AC Susceptibility of Dy<sub>2</sub>Ti<sub>2</sub>O<sub>7</sub>

AC susceptibility measurements of Dy<sub>2</sub>Ti<sub>2</sub>O<sub>7</sub> were performed using the newly constructed magnetometer in order to verify its performance. A sinusoidal field with an amplitude of less than 6 mOe was applied to sample B along the *c*-axis ([110] orientation). The sample was brought to a specific temperature and allowed to equilibrate, after which, ac susceptibility measurements were made by scanning through a frequency range of 10<sup>-3</sup> Hz to 10<sup>4</sup> Hz. The lock-in amplifier detected the in-phase and out-of-phase components of the sample's susceptibility. The spectra are shown in Fig. 4.1. The maximum of the out-of-phase component was used to determine the characteristic relaxation frequency, as discussed in Chapter 2.

A demagnetization correction was made to the susceptibility spectra by employing the following formulas:

$$\begin{aligned}\frac{1}{\chi} &= \frac{1}{\chi_A} - 4\pi N \\ \chi' &= \frac{\chi'_A - 4\pi N(\chi'^2_A + \chi''^2_A)}{(1 - 4\pi N\chi'_A)^2 + (4\pi N\chi''_A)^2} \\ \chi'' &= \frac{\chi''_A}{(1 - 4\pi N\chi'_A)^2 + (4\pi N\chi''_A)^2}\end{aligned}\tag{4.1}$$

Where  $N$  is the demagnetizing factor whose formula is discussed in Ref. [52],  $\chi$  is the total susceptibility, and  $\chi_A$  is the apparent susceptibility. Once the demagnetizing factor was

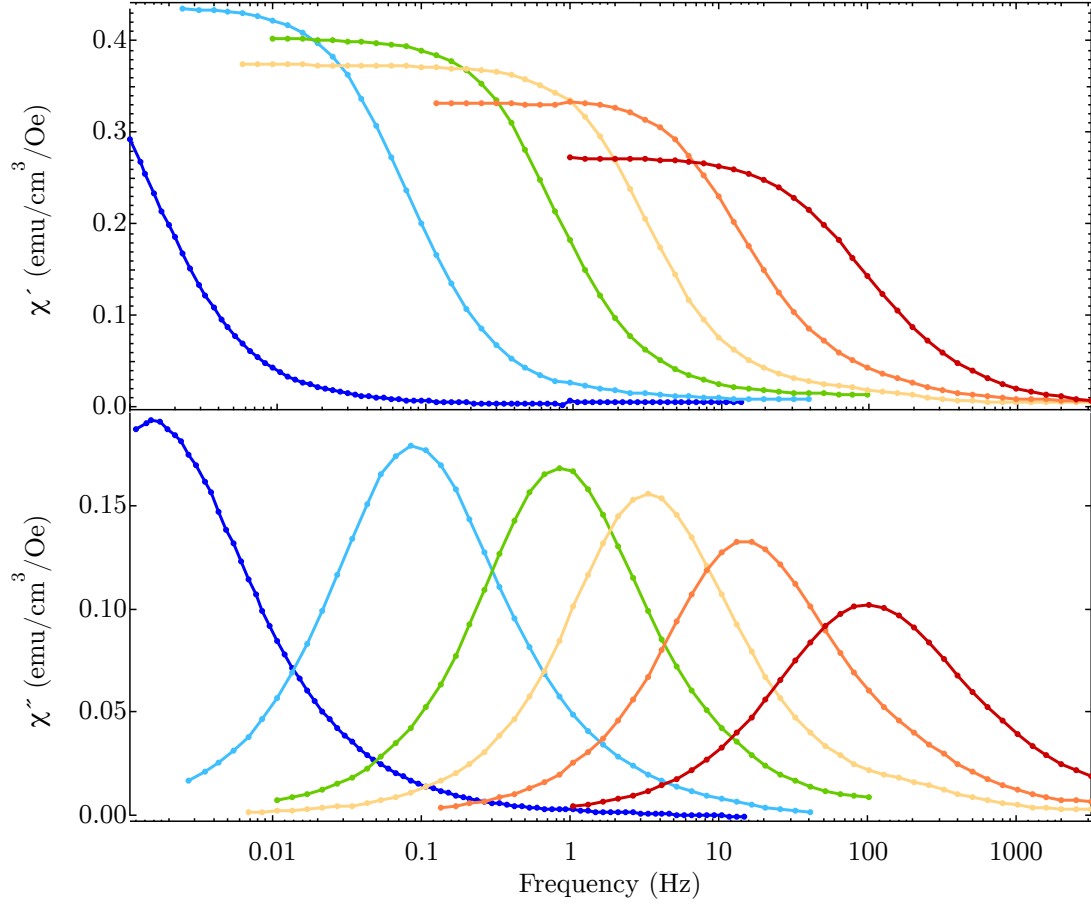


Figure 4.1: AC susceptibility spectra of  $\text{Dy}_2\text{Ti}_2\text{O}_7$  (sample B - oriented in the  $[110]$  crystal direction). **Upper panel:** In-phase susceptibility  $\chi'(f)$ . **Lower panel:** Out-of-phase susceptibility  $\chi''(f)$ . Temperatures (from left to right) are: 0.5 K, 0.64 K, 0.75 K, 0.85 K, 1.0 K, 1.3 K.



taken into account, the spectra were calibrated with the spectra from measurements of a different geometry of the same sample by a least-squares method, which is explained, in detail, in Ref. [8]. The details of the demagnetization correction are provided in Appendix C. The calibration is necessary in order to give the spectra proper, geometry-independent, field-independent, and coupling-independent units. A more conventional way to determine the calibration, is to perform the same experiment on a sample of lead that is cut to exactly geometry as the sample of interest. Since lead is perfectly diamagnetic, the susceptibility will be -1, and the voltage output of the SQUID can be converted to units of susceptibility.

The characteristic frequencies, determined from the ac susceptibility are plotted against inverse temperature in Fig. 4.2. The goal of these measurements was to reproduce the results in Ref. [8] in order to verify the functionality of the gradiometer. The susceptibility measurements made on the new magnetometer agree very well with the susceptibility measurements from Ref. [8] as can be seen by the overlap in Fig. 4.2. DC magnetization measurements are presented in the next section.

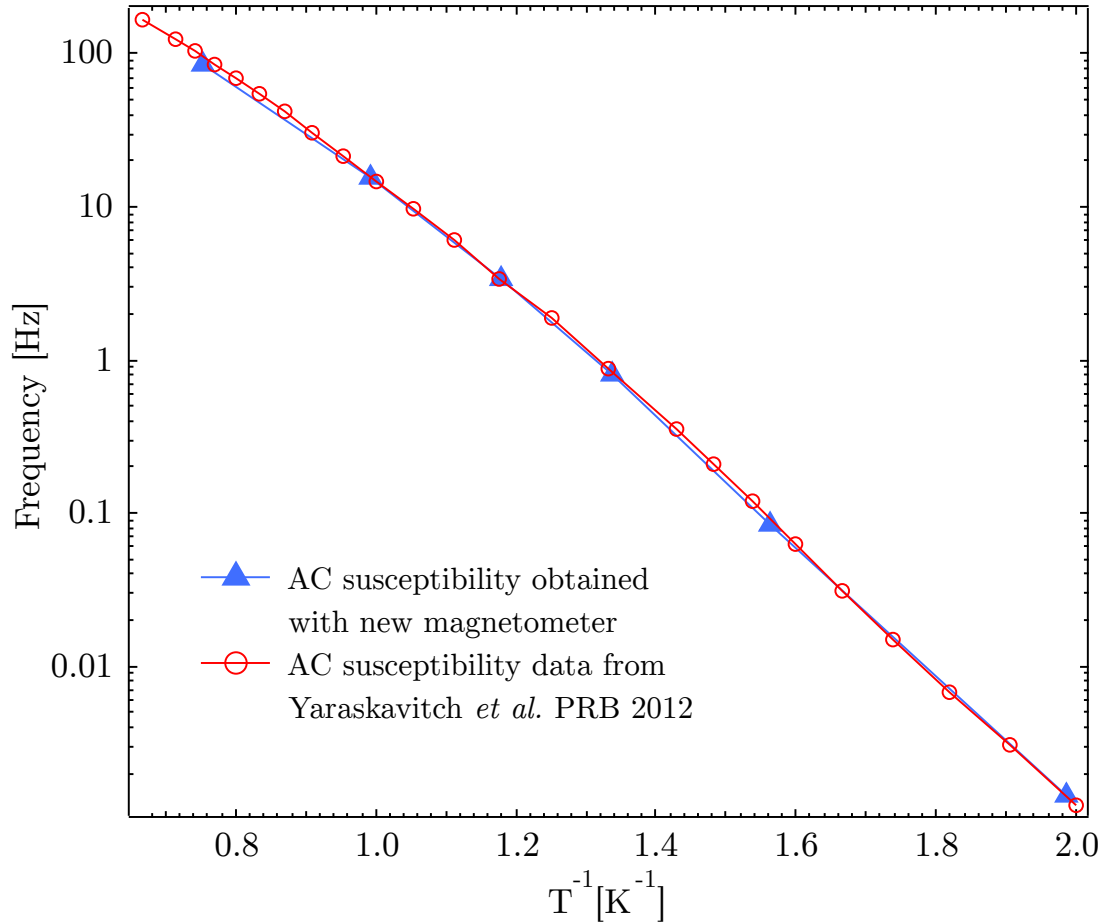


Figure 4.2: AC susceptibility measurements were made on sample B ([110] orientation) using the new magnetometer. A demagnetization correction was made and the calibration procedure discussed in this section was carried out using the susceptibility of a sample with a different geometry. The results from Ref. [8] agree very well with the susceptibility obtained with the new magnetometer, which verifies its functionality.

## 4.2 DC Magnetization of $\text{Dy}_2\text{Ti}_2\text{O}_7$

DC magnetization measurements were made on  $\text{Dy}_2\text{Ti}_2\text{O}_7$ , sample A, along the c-axis ([100] crystal axis). A 5 mOe dc magnetic field was applied until the sample appeared to be fully magnetized. The field was turned off and the relaxation of the magnetization was measured until it appeared that the sample had reached zero magnetization again. This procedure was carried out at 8 different temperatures from 475 mK to 1.1 K. Figs. 4.3 and 4.4 contain the magnetic relaxation data at 0.55 K and 0.9 K, respectively. The decay of the magnetization is much faster at 0.9 K. The dramatic increase of the relaxation time of the magnetic decay with decreasing temperature, makes plotting relaxations at all temperatures on one graph only possible by using a log scale on the time axis. The magnetic relaxations for each different temperature are shown in Fig. 4.5. In Fig. 4.5, in the upper panel, the  $y$ -axis is plotted on a linear scale and in the lower panel the  $y$ -axis is plotted on a log scale. The details of the averaging and normalizing of the data are provided in Appendix A.

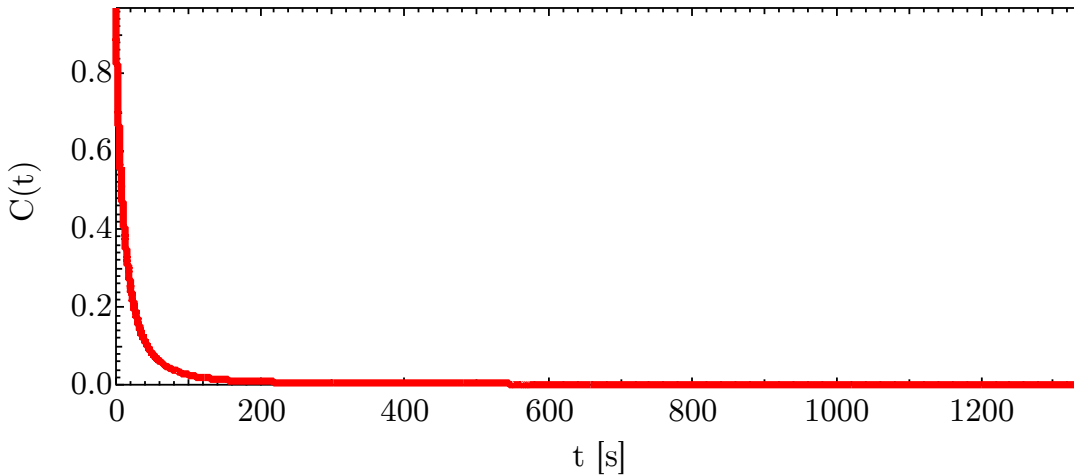


Figure 4.3: Magnetic relaxation at 0.55 K.  $C(t)$  is the magnetization (correlation function<sup>1</sup>) which is plotted against time in seconds.

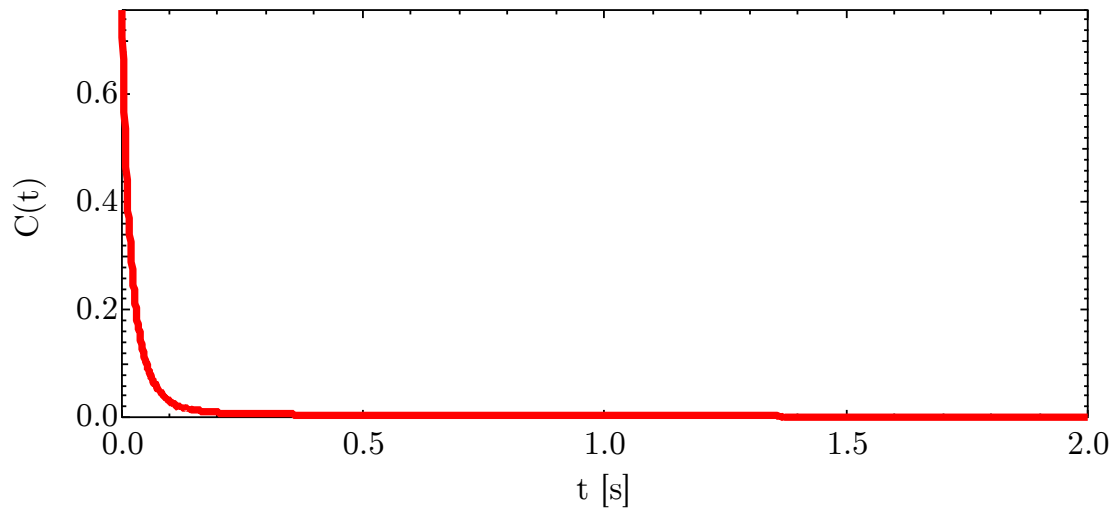


Figure 4.4: Magnetic relaxation at 0.9 K.  $C(t)$  is the magnetization (correlation function<sup>1</sup>) which is plotted against time in seconds.

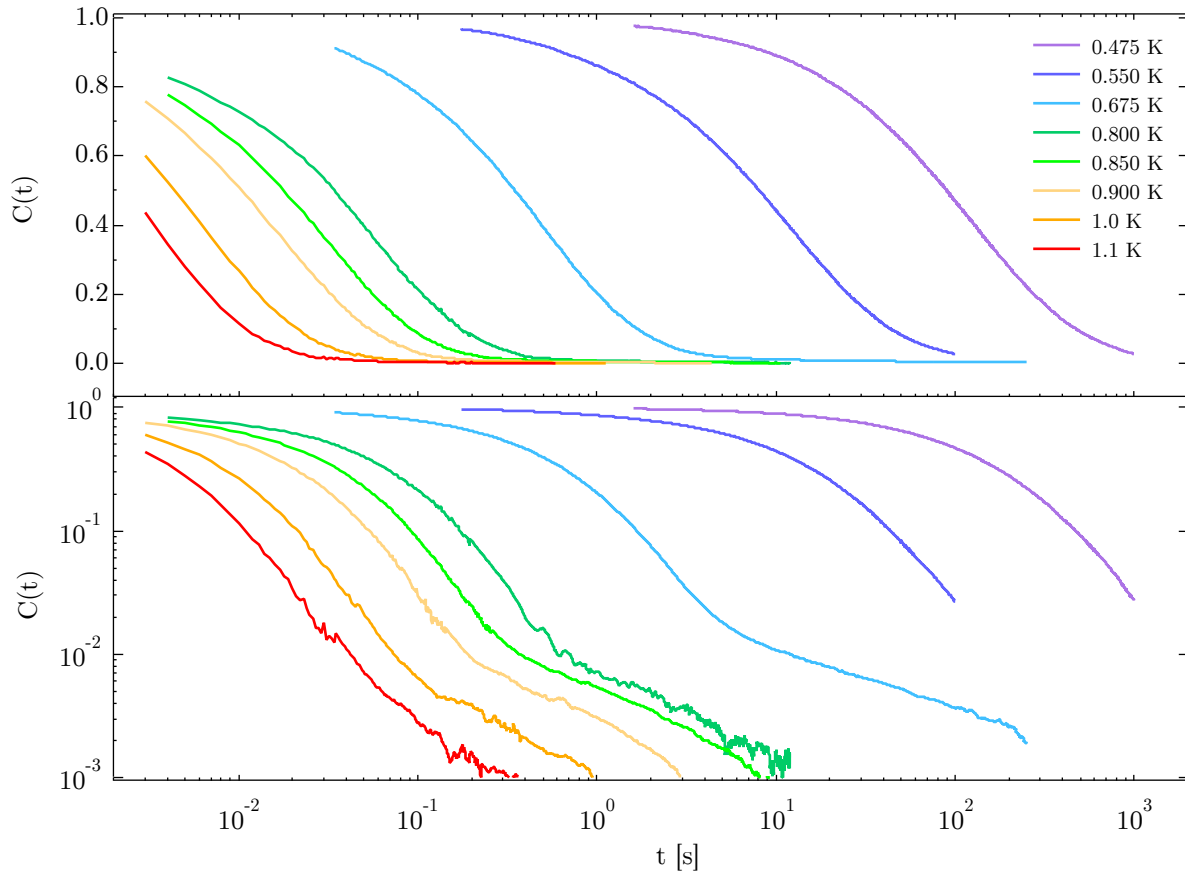


Figure 4.5: Magnetic relaxation data:  $C(t)$  vs.  $t$ . **Upper panel:**  $C(t)$  is plotted on a linear scale against  $t$  (in seconds on a log scale). **Lower panel:**  $C(t)$  is plotted on a log scale against  $t$  (in seconds on a log scale). The temperatures are indicated in the legend or from left to right they are: 1.1 K, 1.0 K, 0.9 K, 0.85 K, 0.8 K, 0.675 K, 0.55 K, 0.475 K.

From the dipolar spin ice model[9], the magnetic relaxation, also referred to as the

correlation function<sup>1</sup>, is expected to be a single exponential decay  $C(t) = e^{-t/\tau(T)}$ . [10, 11] Initially, a single exponential function was fit to the measured magnetic relaxations, however, it did not fit the data well. Next, a double exponential function,  $C(t) = A_1 e^{-t/\tau_1(T)} + A_2 e^{-t/\tau_2(T)}$ , was fit to the data. The double exponential fit the data better than the single exponential, but since a double exponential contains four free parameters,  $(A_1, A_2, \tau_1, \tau_2)$ , under-constraining the fit becomes a risk. Finally, a stretch exponential function,  $C(t) = e^{-(t/\tau)^\beta}$  was fit to the data. The stretch exponential function fit the data the best, as its fit coefficients yielded the lowest standard deviations of any of the fit functions that were tried and under-constraining is less likely in this case as the stretch exponential function contains only two free parameters. By plotting the data as  $\ln(-\ln(C(t)))$  versus  $\ln(t)$ , stretch exponential behaviour manifests itself as a straight line with a slope between 0 and 1. The slope value is the stretch exponent  $\beta$ , therefore with a slope of 1, a single exponential is recovered. In Fig. 4.6 the data is plotted in this way. The data exhibits stretch exponential behaviour and at longer times an algebraic tail develops. The long-time tails can be seen in Fig. 4.6 where the straight lines (stretch exponential behaviour) bend to shallower lines (long-time tails). A stretch exponential with  $\beta = 0.8$  is plotted in Fig. 4.6 for comparison.

---

<sup>1</sup>In Monte Carlo simulation one can use Metropolis dynamics to obtain the correlation function  $C(t) = \langle M(0)M(t) \rangle$ , where  $M(t)$  is the time-dependent magnetization of the sample and  $M(0)$  is the sample's magnetization at  $t = 0$ , which is normalized to 1. The expectation value of these quantities multiplied together is the same relaxation that one observes when a field is applied to a sample and turned off and the magnetization is allowed to relax back to equilibrium [53, 54] - essentially the dc magnetization measurements discussed in this section. For that reason, the magnetic relaxation is also referred to as a correlation function at some points. Later, when the measurements are compared to simulation this connection becomes more important.

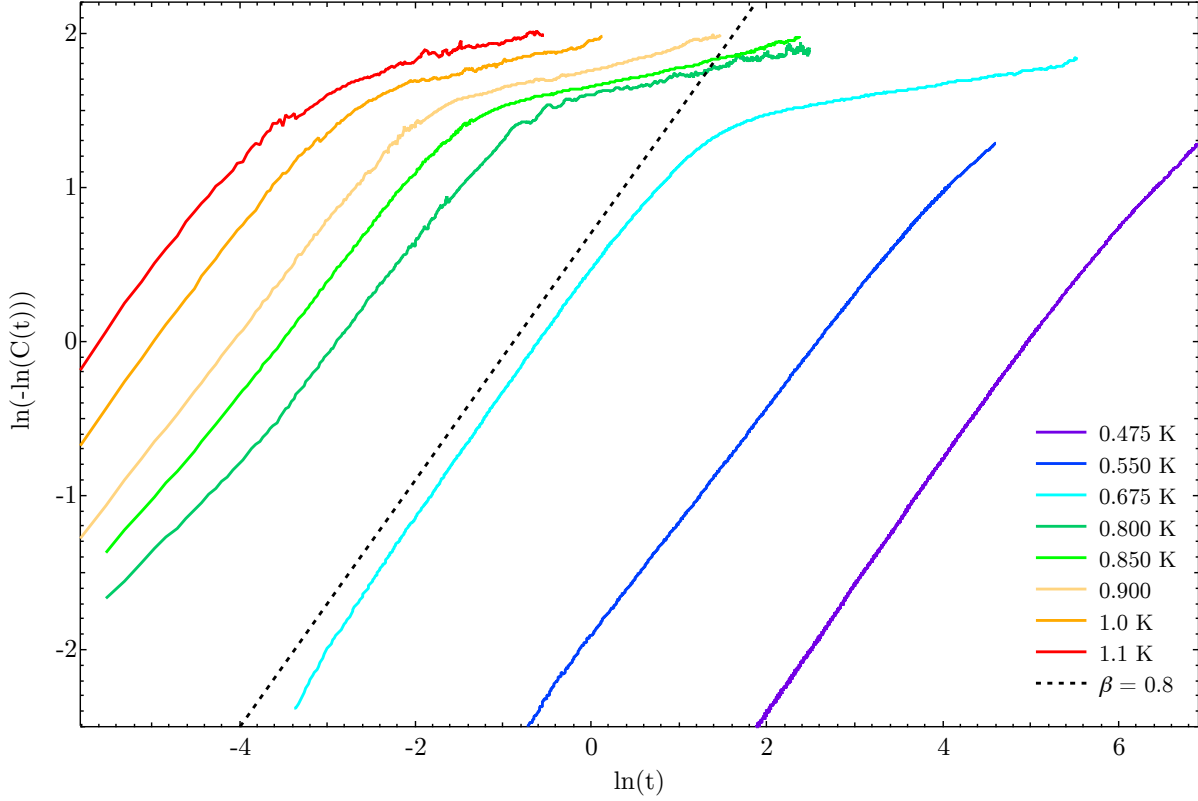


Figure 4.6: Magnetic relaxation data:  $\ln(-\ln(C(t)))$  vs.  $\ln(t)$ . In this plot, a straight line with a slope between 0 and 1 indicates a stretch exponential. The slope is the stretch exponent  $\beta$ . A slope of  $\beta = 0.8$  is plotted for comparison beside the measurements. The deviation from stretch exponential behaviour is a long-time algebraic tail. The temperatures are indicated in the legend or from left to right they are: 1.1 K, 1.0 K, 0.9 K, 0.85 K, 0.8 K, 0.675 K, 0.55 K, 0.475 K.

The data was fit to a stretch exponential function for each temperature and the fit parameters are plotted as a function of inverse temperature shown in Figs. 4.7 and 4.8. The limits of fitting and fitting methods are discussed in Appendix A. The stretch factor  $\beta$ , plotted in Fig. 4.7, is between 0.7 and 0.8 across the temperatures where the relaxation was measured, with no noticeable temperature dependence. The relaxation times (correlation times<sup>2</sup>) are plotted against inverse temperature which is useful, as plotting in

<sup>2</sup>We will use the two terms interchangeably.

this manner easily exposes Arrhenius temperature activated behaviour or the lack thereof. The relaxation is temperature activated, evidenced by the data in Fig. 4.8 fitting well to a line. The slope of the line yields the energy barrier to relaxation, which in this case is  $9.19 \pm 0.34$  K, contrary to the  $\sim 5.2$  K energy barrier which is predicted by the dipolar spin ice model. This value of 5.2 K is obtained from Monte Carlo simulations, which are discussed in the following section. The characteristic relaxation time  $\tau_o$ , obtained from the fits to the dc magnetization data, is  $6.2 \pm 2.5 \times 10^{-7}$  s, corresponding to an attempt rate of  $2.6 \times 10^5$  s $^{-1}$ .



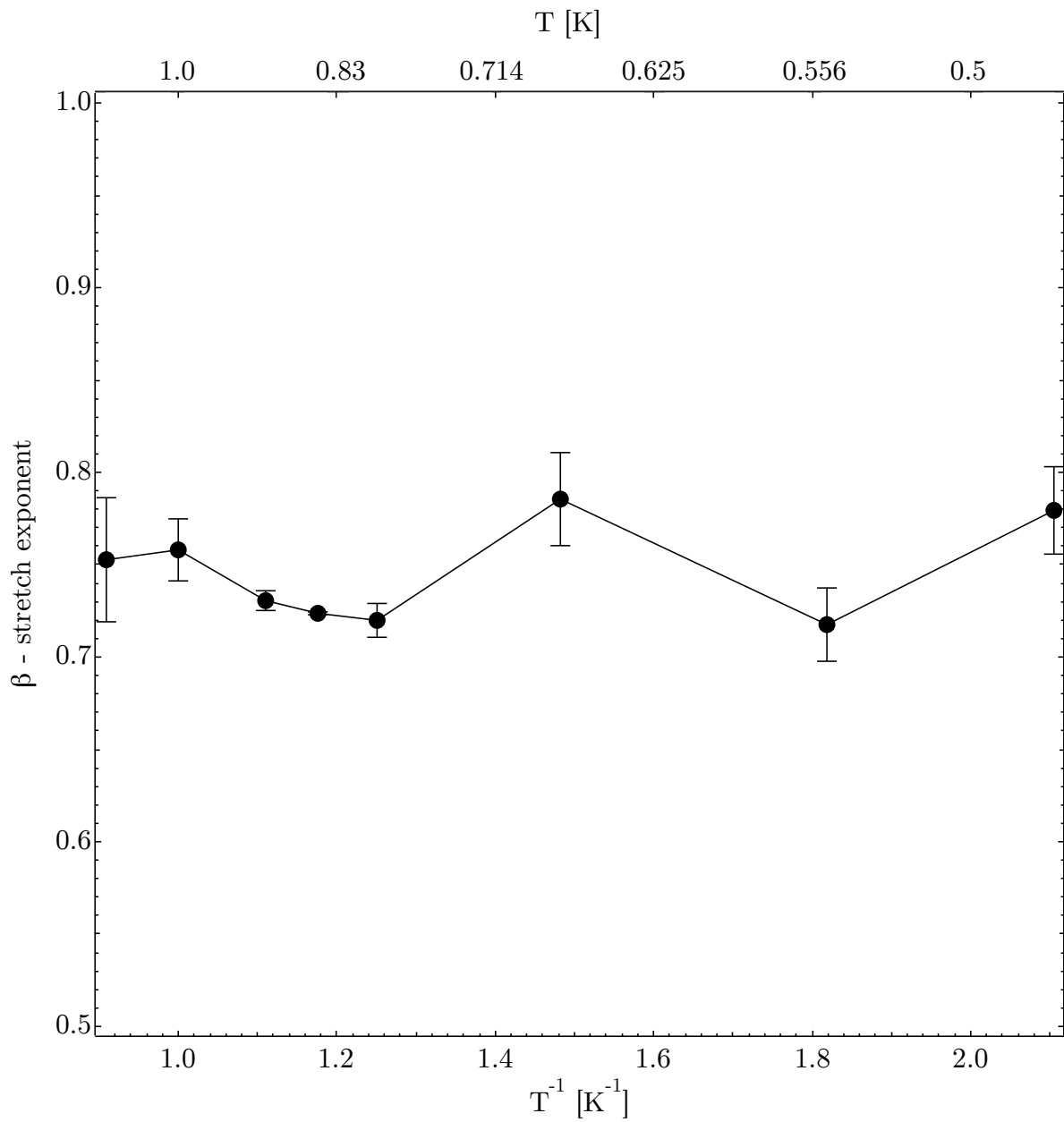


Figure 4.7: Stretch exponent ( $\beta$ ) versus inverse temperature ( $T^{-1}$ ). Over the range of temperature where measurements were made, the stretch factor is nearly temperature independent and sits between 0.7 and 0.8.

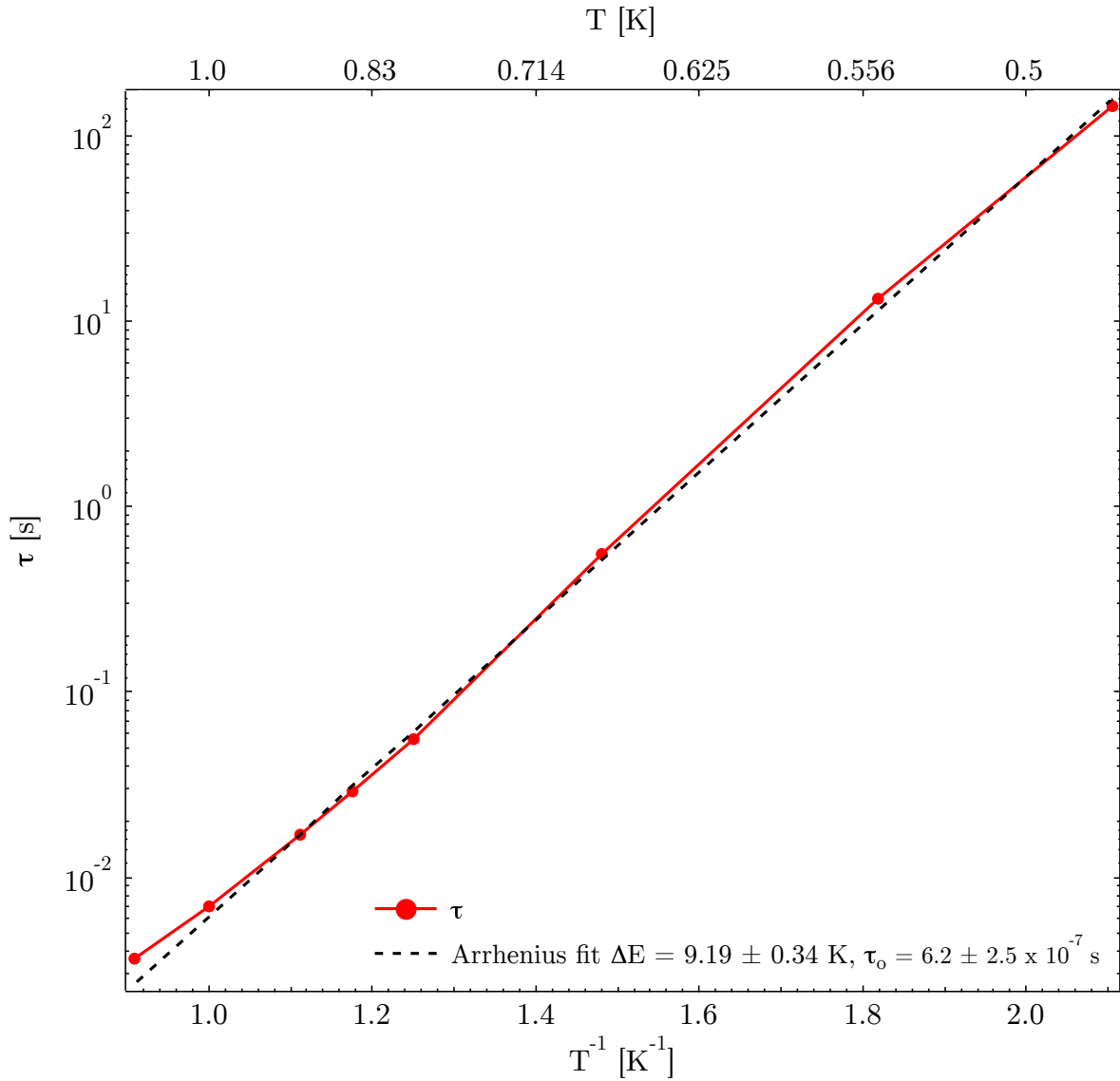


Figure 4.8: Relaxation time ( $\tau$ ) vs. inverse temperature ( $T^{-1}$ ). When relaxation times are plotted on a log scale versus inverse temperature Arrhenius temperature activated behaviour is represented by a line. The observed relaxation appears to be temperature activated with an energy barrier  $\Delta E = 9.19 \pm 0.34$  K and a spin flip rate  $\tau_0 = 6.2 \pm 2.5 \times 10^{-7}$  s. (Error bars are too small to see)

The measurements of the magnetic relaxation of  $\text{Dy}_2\text{Ti}_2\text{O}_7$  yielded three important differences from the relaxation expected by the dipolar spin ice model. The first difference is that decay is a stretched exponential rather than a single exponential. The second difference is that at longer times, the relaxation deviates from an exponential decay into what will be referred to as a long-time algebraic tail. The third and final difference is that an energy barrier to relaxation of about 5 K is predicted by the dipolar spin ice model and the measurements yield an energy barrier of about 9 K. In order to investigate these differences further a theorist, Patrik Henelius<sup>3</sup>, became a collaborator on this project. He was able to transform the ac susceptibility data from Ref. [8] into the time domain for comparison purposes and as well as perform extensive Monte Carlo simulations to look for physical reasons for the characteristics listed above.

---

<sup>3</sup>Affiliation: *Dept of Theoretical Physics, Royal Institute of Technology, SE-106 91 Stockholm, Sweden*



# Chapter 5

## Comparison to AC Susceptibility and Monte Carlo Simulation

### 5.1 Comparison to AC Susceptibility

It is possible to transform ac susceptibility data into the time domain using the fluctuation-dissipation theorem. The fluctuation-dissipation theorem hinges on the assumption that the response of a system in equilibrium to a small applied field is the same as its response to a random fluctuation. A thorough review of this theorem can be found in Ref. [55]. The experiments were performed in the linear response regime, meaning the magnetic response of the material was proportional to the applied field, which caused the fluctuation-dissipation theorem to be valid. The ac susceptibility data from Ref. [8] was transformed by,

$$C(t) = \langle M(0)M(t) \rangle = 2kT \int_{-\infty}^{\infty} \frac{\chi''(\omega)}{\omega} \cos(\omega t) d\omega \quad (5.1)$$

The transform relies heavily on the accuracy of the functional fitting to the out-of-phase susceptibility. The following function[56] was fit to the imaginary part of the susceptibility in Ref. [8],

$$\chi''(\omega) = \frac{1}{[(\tau\omega)^{\alpha_1 n} + (\tau\omega)^{-\alpha_2 n}]^{1/n}} \quad (5.2)$$

Equation 5.2 fit the susceptibility data over the entire frequency range much more accurately than a single or double Debye model, which assumes that the out-of-phase susceptibility is a Lorentzian function. The different fits are shown in Fig. 5.1.

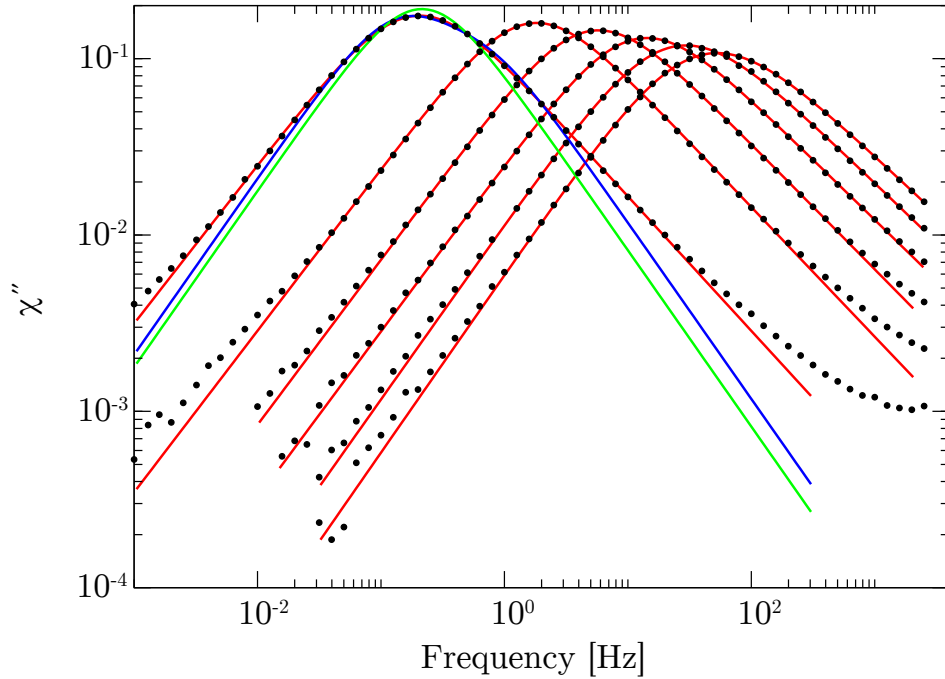


Figure 5.1: Different fits to the out-of-phase susceptibility. (Black dots) AC susceptibility from Ref. [8]. (Green line) Fit to a single Debye model. (Blue line) Fit to a double Debye model. (Red lines) Fits to Equation 5.2. Equation 5.2 describes the spectra much better than the other two models, however at the edges of the fit there is a slight deviation of the fit from the data.

The transformed ac susceptibility data is plotted in Fig. 5.2 with the dc magnetization measurements and Monte Carlo simulation results. The Monte Carlo simulations will be discussed in more detail further on in this section. In Fig. 5.2, the transformed susceptibility is shown in green. The transformed susceptibility qualitatively exhibits the same characteristics in its relaxations as the time domain dc measurements. The relaxations are stretched exponentials which turn into long-time algebraic tails at longer times. These characteristics can most easily be seen by looking at the lower panel in Fig. 5.2 where the data is plotted on a graph of  $\ln(-\ln(C(t)))$  against  $\log(t)$ . The straight lines on this plot with non-unitary slopes indicate that the relaxations are stretched exponentials with a stretch exponent,  $\beta$ , of about 0.7 to 0.8, which is also the case for the relaxations from dc magnetization measurements.

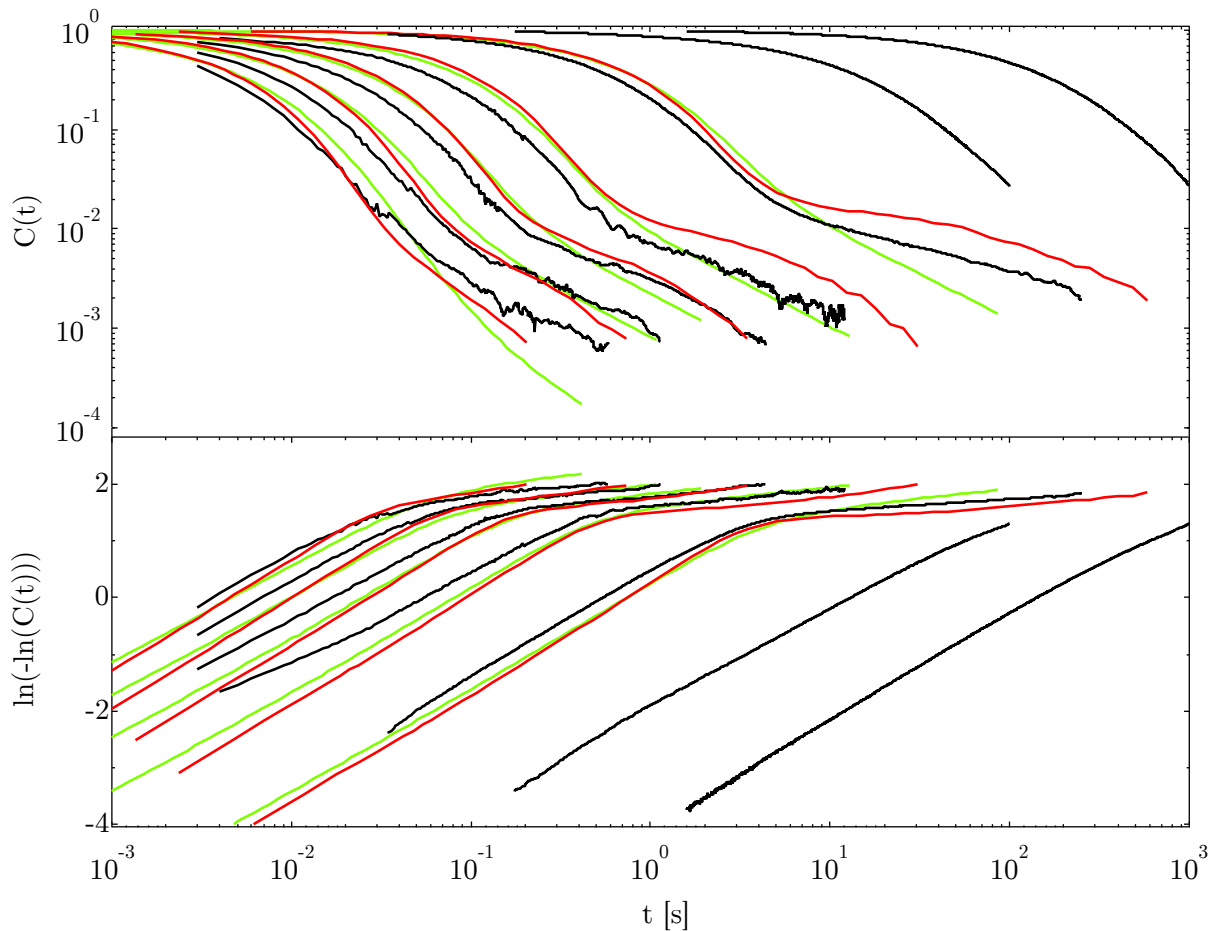


Figure 5.2: Monte Carlo simulation compared to experiment. (Red lines) Monte Carlo simulations of the dipolar spin ice model using Metropolis dynamics, open boundary conditions and a small inclusion (0.3%) of stuffed spins. (Black lines) Magnetic relaxation data. The relaxation characteristics agree, qualitatively. The stuffing causes the long time tail, and the use of open boundary conditions causes the stretching. (Green lines) AC susceptibility from Ref. [8] which has been transformed to the time domain. Temperatures from left to right are: 1.1 K, 1.0 K, 0.9 K, 0.8 K, 0.675 K, 0.55 K, 0.475 K. **Upper panel:** magnetization decay versus time with both the  $x$  and  $y$  axes in a log scale. **Lower panel:**  $\ln(-\ln(C(t)))$  versus time, where the stretch exponential behaviour is demonstrated by a straight line and the bending at the ends represents the long-time tail.

The long-time algebraic tails are slightly different than the tails from the dc magnetization measurements. Qualitatively, they both exhibit the long-time tail, however, quantitatively the bend of the tails differ at some temperatures. The bends of the tails in the transformed susceptibility data are generally slightly more shallow than the bends of the tails in the dc magnetic measurements. This difference could be due to two things: the sensitivity of the normalization of the dc magnetization data or the fitting of the ac susceptibility data. In the first case, hypothetically speaking, if the definition of zero magnetization in the dc measurements were made higher, meaning that the measurement was closer to being fully relaxed than was assumed when the data was normalized, the tails would end up having a less steep bend to them, agreeing more closely with the transformed ac susceptibility data. A systematic fitting was performed to determine a value for zero magnetization in the dc measurements, which is discussed in more detail in Appendix A. In the second case, the function used to fit to the out-of-phase susceptibility, Equation. 5.2, does not fit the ends of the spectra exactly, which can be seen in Fig. 5.1. Since the transformation of the susceptibility into the time domain is an integration of the fit function over frequency space, if some of the out-of-phase susceptibility is not accounted at the ends of the spectra, the transformation will be affected. This could be part of the reason for the quantitative disagreement in the tails of the relaxation between the ac and dc magnetic measurements. The important point to be made is that both independent measurement techniques on different magnetometers both show this long-time algebraic tail in the relaxation, and it can be stated with confidence that this is a unique characteristic emanating from the material and not an artifact of the measurement.

The relaxation measured with ac susceptibility from Ref. [8] is temperature activated with a barrier to relaxation of about 9-10 K, which was also observed in the dc magnetization measurements of the relaxation. In summary, the transformed ac susceptibility data has confirmed the three characteristics that were observed by the dc magnetization measurements: stretched exponential relaxation with a long-time algebraic tail, and temperature activated relaxation  $\tau(T)$ , with an energy barrier of about 9 K.

## 5.2 Comparison to Monte Carlo Simulation

Dynamic Monte Carlo calculations were performed by Patrik Henelius in order to obtain the dynamic correlation function  $C(t) = \langle M(0)M(t) \rangle$ . As the experimental measurements were performed in the linear response regime, the fluctuation dissipation theorem[55] allows for the correlation function  $C(t)$  and the normalized magnetic relaxation to be directly compared. As a starting point, simulations of the dipolar spin ice model were performed



using periodic boundary conditions and Metropolis dynamics, similar to the simulations performed in Ref. [11] by Jaubert and Holdsworth. The simulated magnetic relaxations (or equivalently, decay of correlations) obtained are shown in Fig. 5.3. As briefly mentioned, the dipolar spin ice model yields a single exponential correlation decay  $C(t) = e^{-t/\tau(T)}$  at all temperatures shown. The decays simulated from the dipolar spin ice model with periodic boundary conditions are plotted in red in Fig. 5.3. The single exponential decays manifest themselves as straight lines with slopes of 1 in a plot of  $\ln(-\ln(C(t)))$  versus  $\ln(t)$ , which is shown in the lower panel of Fig. 5.3. The simulations of the decays predict an Arrhenius temperature activated correlation time (relaxation time)  $\tau(T) = \tau_0 e^{\Delta E/T}$ , with an energy barrier of 5.2 K. The decays obtained from the simulations of the dipolar spin ice model with periodic boundary conditions are unable to capture the stretch exponential behaviour, long-time tail, and Arrhenius activation energy barrier of  $\sim 9$  K that is observed in experiment.

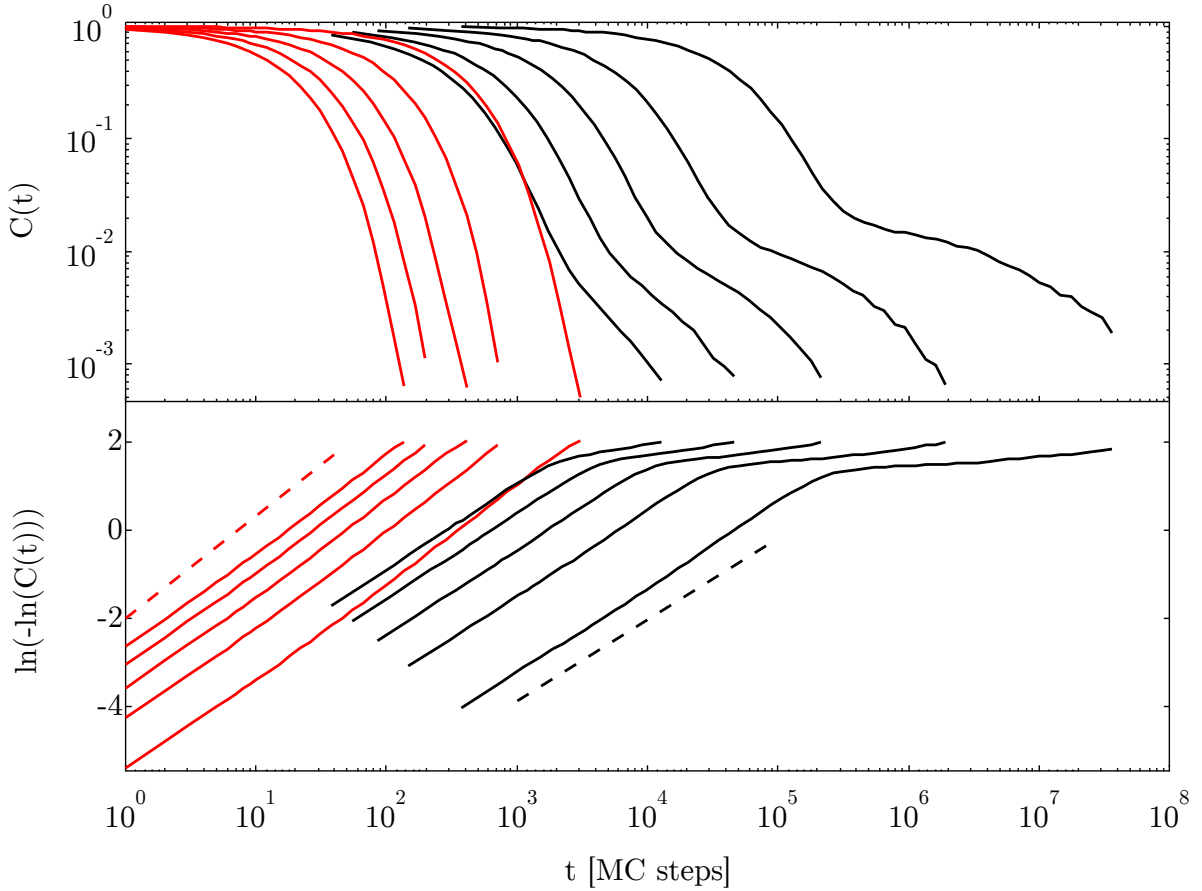


Figure 5.3: Decay of correlations (magnetization) from simulations. (Red lines) Dynamic correlation function from Monte Carlo simulations of the dipolar spin ice model using periodic boundary conditions. (Black lines) Dynamic correlation function from Monte Carlo simulations using open boundary conditions with 0.3% stuffed spins and an additional energy barrier of  $U = 4$  K. Temperatures from left to right are: 1.1 K, 1.0 K, 0.9 K, 0.8 K, 0.675 K. **Upper panel:** Correlation decay versus time with both the  $x$  and  $y$  axes in a log scale. **Lower panel:**  $\ln(-\ln(C(t)))$  versus time, where the stretch exponential behaviour is demonstrated by a straight line and the bending at the ends represents the long-time tail. (Red dashed line) represents  $\beta = 1$ , single exponential behaviour. (Black dashed line) represents  $\beta = 0.8$ , for comparison.

Several changes were introduced within the simulations of the dipolar spin ice model

with the intention of discovering what would give rise to the characteristics observed in the data. First, additional nonmagnetic Ti ions were put in place of some of the Dy ions, effectively diluting the spin ice, which has been studied by other groups in the past experimentally.[44] However, diluting the spins only sped up the dynamics and did not cause a stretched decay. There was also no major change to the simulated correlation decays from tweaking the value of the next-nearest neighbour exchange energy values.[57] Introducing a simple model of a stacking fault, by removing an atom, had no qualitative effect on the decays. Using quantum dynamic loop updates[19] did not reproduce any of the characteristics observed in the data either. It was found that three are independent modifications to the dipolar spin ice model that do lead to the behaviour observed in the magnetization decay data. The three modifications were: the use of open boundary conditions, the inclusion of a very small amount (0.3%) of additional stuffed spins and the addition of an energy barrier ( $U = 4$  K) to overturn any spin, all of which will now be discussed in more detail.

The use of open boundary conditions caused the correlation decay to become stretched with a stretch factor of about 0.8-0.85, which is very close to the stretch exponent that was observed in experiment (0.7-0.8). Periodic boundary conditions are the most common way to treat boundaries in simulations of materials. It avoids the common problem of boundary effects becoming large with a small system size. Stretched exponential behaviour was established with open boundary conditions for a system size of 1024 spins and as well for a system size of 16000 spins, which would suggest that stretched exponential behaviour is a genuine result of surface effects. The specific heat obtained from simulation converges to only slightly different limits with open boundary conditions compared to periodic boundary conditions, which suggests that the validity of model has not been compromised by this approach to the boundary conditions.

The inclusion of 0.3% extra Dy ions (“stuffed spins”) in place of nonmagnetic Ti ions lead to the formation of a long-time algebraic tail in the correlation decay, similar to the the algebraic long-time tails observed in both the ac susceptibility data and dc magnetization data. This can be seen in Fig. 5.3, where simulations of the dipolar spin ice model, in red, are compared to simulations with open boundary conditions and a small amount of stuffed spins, in black. The qualitative agreement between experiment and simulation can most easily be seen in Fig. 5.2, where the transformed ac susceptibility data and dc magnetic relaxation data are plotted with the simulated correlation decays across the same temperature range.

In the simulations, the stuffed spins are assumed to be the same magnitude as the normal Dy spins ( $10 \mu_B$ ) and have the same nearest neighbour exchange. The stuffed spins are also assumed to be Ising and forced to point along the local  $\langle 111 \rangle$  axes of the

Ti pyrochlore lattice. Fig. 5.4 contains a diagram of the crystallographic environment of the stuffed spin in the lowest energy configuration. The stuffed spin has six nearest neighbour spins. The average energy required to flip a spin next to the stuffed spin is 8.6 K (usually 5.8 K for ordinary Dy spins). The average energy required to flip a stuffed spin is 14.5 K. Counterintuitively, it is actually energetically favourable for monopole excitations to be created near the stuffed spins. Fig. 5.5 contains a plot of the monopole density and energy as a function of distance from a stuffed spin. Finding a monopole pair in tetrahedra that are neighbours a stuffed spin is three times more likely than in the rest of the material at  $T=0.675$  K, according to simulation. Essentially, the stuffed spins trap monopole excitations. Fig. 5.5 contains a plot of the energy of the configuration against the distance between the centre of mass of a monopole pair and the stuffed spin. The simulation considers two monopoles and assumes they are in adjacent tetrahedra, but are allowed to be anywhere in the lattice. There is a minimum in the energy when the monopoles reside in the tetrahedra which neighbour the stuffed spin. Not only is it more energetically favourable for a pair of monopoles to be next to the stuffed spin, but more monopole excitations are created next to a stuffed spin. The 8.6 K energy barrier to create a monopole pair next to a stuffed spin is only for the lowest energy configuration shown in Fig. 5.4 - the nearest neighbour spins either both pointing in or both pointing out of the neighbouring tetrahedra. Once a monopole disrupts this configuration and one spin is flipped the other way, the barrier to overturning a nearest neighbour spin to the stuffed spin becomes 2 K, which means there is an increase in monopole excitation creations with this low average local energy barrier.

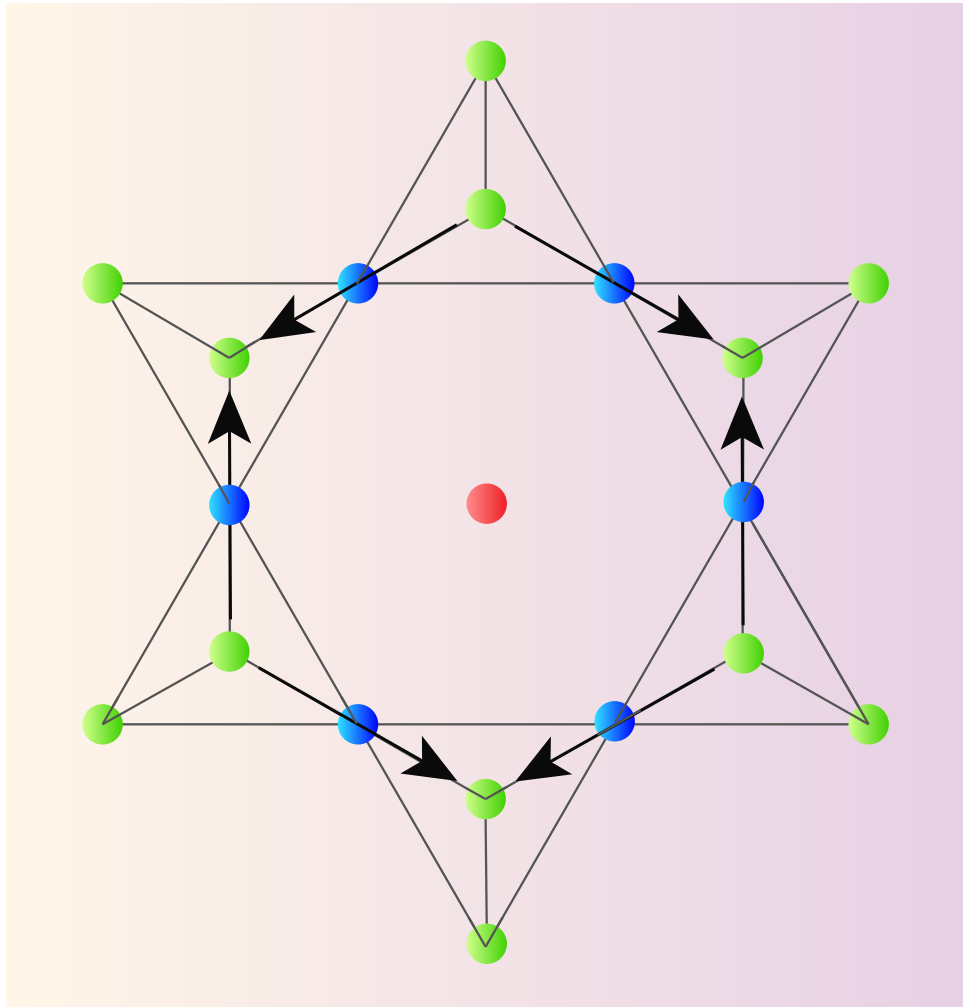


Figure 5.4: Configuration of a stuffed spin. This is the lowest energy configuration, i.e. the adjacent spins closest to the stuffed spin either both point in or both point out of their respective tetrahedra. The red central dot represents the stuffed spin. The blue dots are nearest neighbour spins to the stuffed spin, with the arrows representing the local Ising axes. The other further nearest neighbour spins are shown in green.

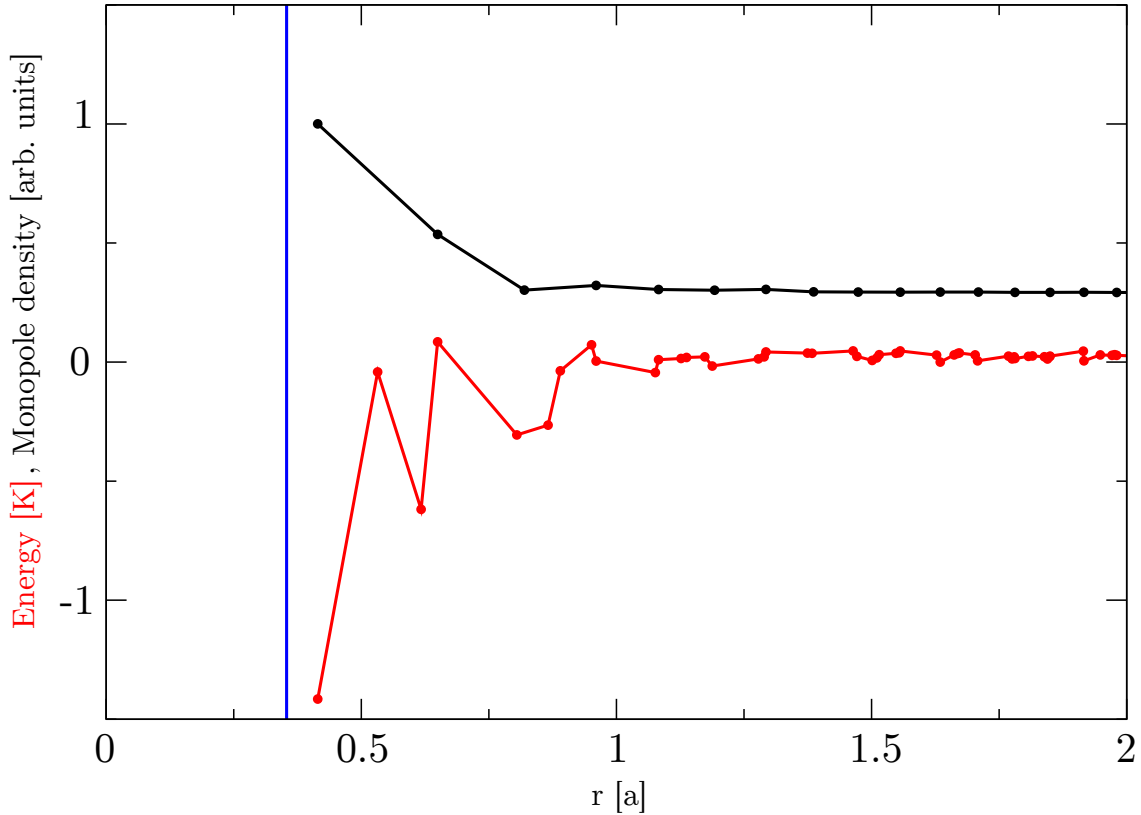


Figure 5.5: Monte Carlo density of monopoles (black) as a function of the distance from a stuffed spin. Energy of the spin ice configurations containing one monopole pair as a function of pair distance from the stuffed spin. The distance from the stuffed spin is in units of  $a$ , the unit cell length. (Blue line) indicates the nearest neighbour spin distance. **Note:** The energy is only calculated for configurations where the monopoles occupy adjacent tetrahedra, since the energy depends heavily on monopole separation.

In other studies[58, 59], higher levels ( $\sim 5\text{-}30\%$ ) of stuffing in  $\text{Dy}_2\text{Ti}_2\text{O}_7$  have been looked at, however, in this case the effects of a very small amount ( $< 1\%$ ) are being considered. It is not unimaginable that in many real samples a small amount of stuffing is plausible as no material is defect free. The strong effects of a small amount of disorder are quite interesting and should be studied further.

The final aspect of the simulations left to discuss is the addition of an energy barrier  $U = 4\text{K}$  to overturn a spin. Previously, in Refs. [10, 11] the basic spin flip process in

$\text{Dy}_2\text{Ti}_2\text{O}_7$  has been assumed to be temperature independent. This assumption is referred to as the quantum tunnelling hypothesis. The argument for this hypothesis is basically the following. To flip a spin while in the 2-in-2-out ground state, there is an energy cost on the order of the effective exchange interaction between spins. However, to actually flip the spin in terms of crystal field energies, from an up-Ising to a down-Ising state, the energy is on the order of 200 K (for  $\text{Dy}_2\text{Ti}_2\text{O}_7$  and about 300 K for  $\text{Ho}_2\text{Ti}_2\text{O}_7$ ). Below 10 K, this transition is inaccessible, unless the process is achieved through quantum tunnelling between the two ground state doublets. The quantum tunnelling has been suggested to be facilitated by transverse fields from neighbouring spins.[60] The basic spin flip rate has been inferred by Jaubert and Holdsworth to be  $\tau_o = 10^{-3}$  s from fitting an Arrhenius function between 10 K and 2 K in the “quasi-plateau” regime of the relaxation in Ref. [36]. Owing to the fact that the observation of a  $\sim 9$  K energy barrier compared with the 5.2 K energy barrier predicted by the dipolar spin ice model, has not yet been explained, it would seem plausible that the basic spin flip process is not completely temperature independent. The addition of a  $U = 4$  K energy barrier causes the theory to match experiment. The physical interpretation of this energy barrier is that the basic spin flip process from one Ising-state to the other is temperature activated with an energy barrier of 4 K. By this logic, the fit to an Arrhenius law below 1 K is,

$$\begin{aligned} \tau(T) &= \tau_o \exp(5.2 \text{ K}/T) \\ \text{and becomes } \tau(T) &= \tau_o(T) \exp(5.2 \text{ K}/T) \\ &= \tau'_o \exp(9.2 \text{ K}/T) \end{aligned} \tag{5.3}$$

where  $\tau_o(T) = \tau'_o \exp(4 \text{ K}/T)$  and  $\tau'_o \approx 10^{-7}$  s. This still leaves room for further research and more questions, as it is not clear how a combination of quantum tunnelling and temperature activation are creating this 4 K energy barrier for any spin to flip. Also, could it be that below 2 K, the basic spin flip process becomes temperature activated, whereas in the “quas-plateau” regime, it is completely governed by quantum tunneling? The attempt rate  $\tau'_o = 10^{-7}$  s is more usual for magnetic materials than the previous value of  $10^{-3}$  s obtained from the interpretation of Ref. [36], which may require a demagnetization correction.

### 5.3 Two- $\tau$ Model: Comparison to Recent Work

Throughout the course of this work, Matsuhira *et al.* performed ac susceptibility and dc magnetization measurements on Dy<sub>2</sub>Ti<sub>2</sub>O<sub>7</sub>. [43] In Ref. [43], Matsuhira *et al.* analyze their ac and dc measurements differently than how the results presented in this thesis are analyzed. With regards to their dc measurements they magnetize their sample of Dy<sub>2</sub>Ti<sub>2</sub>O<sub>7</sub>, which is cut to a needle geometry with the [111] crystal axis pointed along the sample plane, with a 5 Oe magnetic field and measure the relaxation with a SQUID. They fit the relaxation with a double exponential function,

$$M(t) = M_L e^{-t/\tau_L} + M_S e^{-t/\tau_S} + M_o \quad (5.4)$$

where  $M_L$ ,  $M_S$ ,  $\tau_L$ ,  $\tau_S$ , and  $M_o$  are the fit parameters. For the ac measurements they use a sinusoidal excitation with a magnitude of  $< 1.4$  Oe and record the in-phase and out-of-phase susceptibility. Matsuhira *et al.* fit their out-of-phase susceptibility to a 2- $\tau$  Debye model,

$$\chi''(f) = \chi_L \frac{2\pi f \tau_L}{1 + (2\pi f \tau_L)^2} + \chi_S \frac{2\pi f \tau_S}{1 + (2\pi f \tau_S)^2} \quad (5.5)$$

where  $\chi_L$ ,  $\chi_S$ ,  $\tau_L$ , and  $\tau_S$  are the fit parameters.

It is beneficial to compare the measurements from Ref. [8] and this thesis with the measurements by Matsuhira *et al.* [43] to see whether they agree. In order to facilitate the comparison, the dc magnetization data in this thesis and the ac susceptibility data from Ref. [8] are fit with Equations 5.4 and 5.5, respectively. Fig. 5.6 contains a graph of the time constants,  $\tau_1$  and  $\tau_2$ , obtained from fitting the dc magnetization data from this thesis with Equation 5.4 along with the time constants,  $\tau_L$  and  $\tau_S$ , presented in Ref. [43] plotted as a function of inverse temperature. The two results overlap with reasonable agreement. It is likely that within error they agree, as choice of fitting limits have a considerable effect on the fit parameters, suggesting there is a fair bit of error associated with the time constants obtained from the fits. This agreement is evidence that the relaxation measurements of Dy<sub>2</sub>Ti<sub>2</sub>O<sub>7</sub> are reproducible.



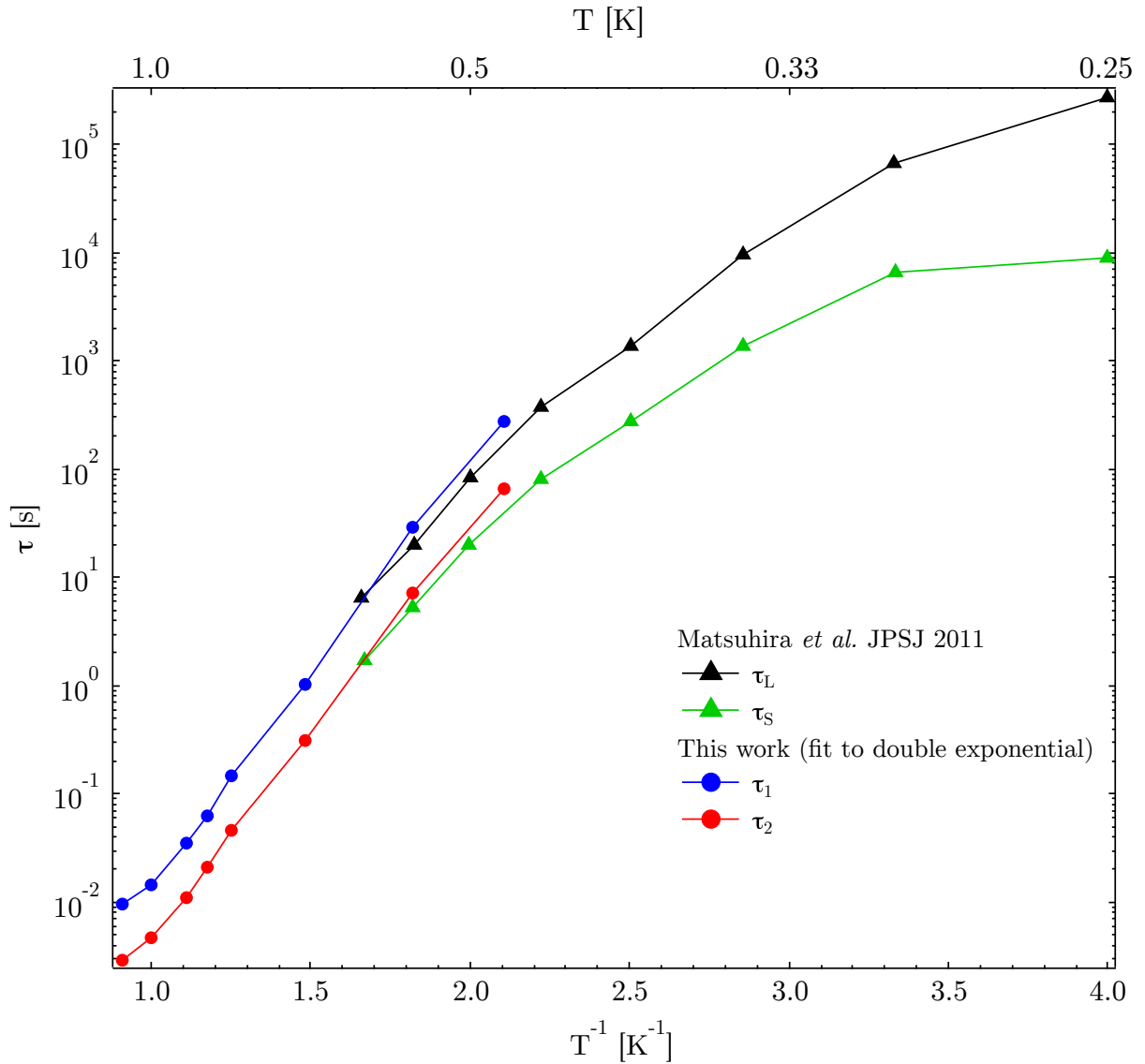


Figure 5.6: Two- $\tau$  fit comparison of dc magnetization data. (Blue circles) and (red circles) are the time constants,  $\tau_1$  and  $\tau_2$ , obtained by fitting the magnetic relaxation measurements presented in this thesis to a double exponential function. (Black triangles) and (green triangles) are the time constants  $\tau_L$  and  $\tau_S$  from Ref. [43]. The two results agree within error.

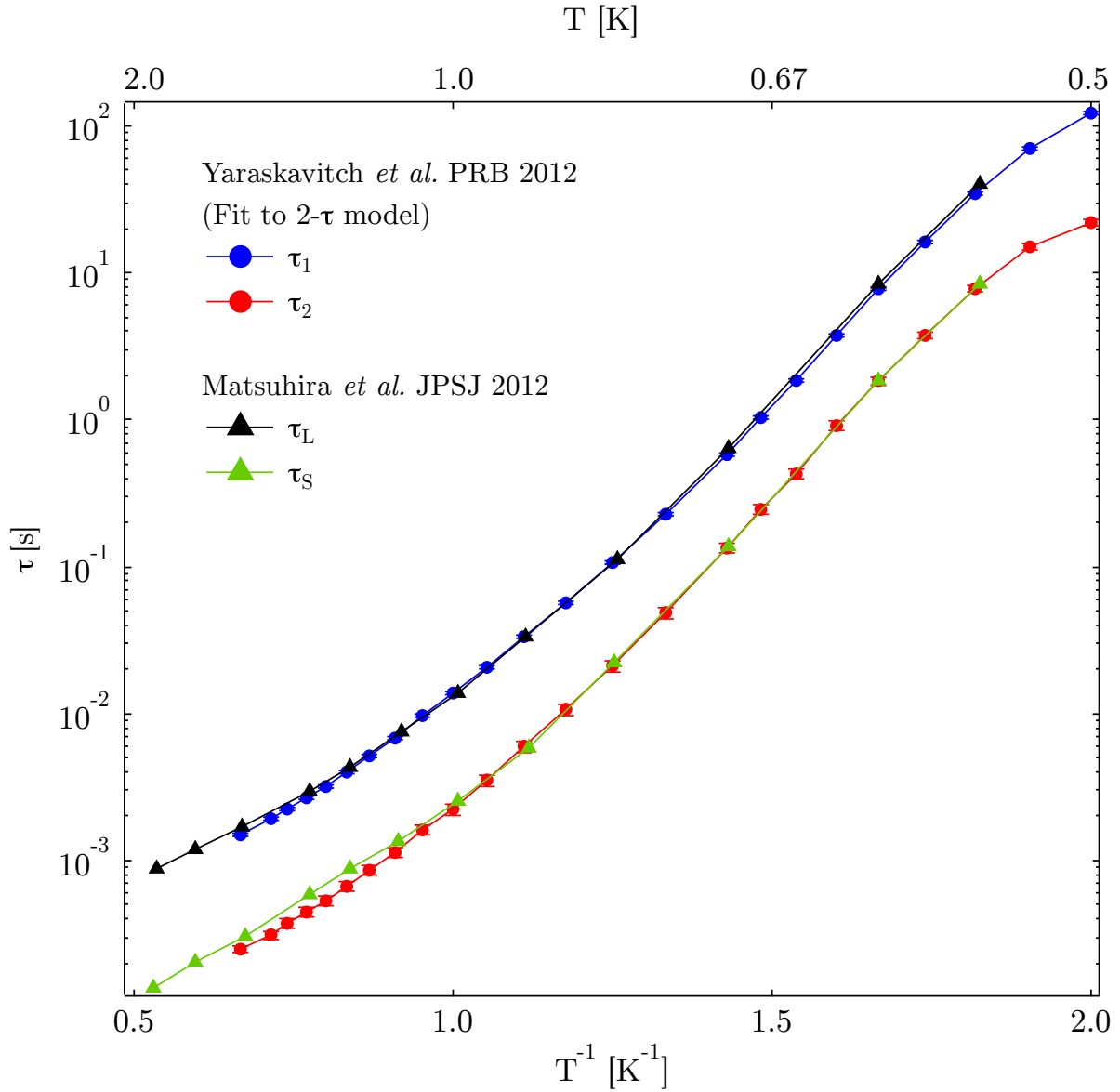


Figure 5.7: Two- $\tau$  fit comparison of ac susceptibility data. (Blue circles) and (red circles) are the time constants,  $\tau_1$  and  $\tau_2$ , obtained by fitting the out-of-phase susceptibility in Ref. [8] to Equation 5.5, a two- $\tau$  Debye model. (Black triangles) and (green triangles) are the time constants  $\tau_L$  and  $\tau_S$  from Ref. [43]. The two results agree very well over the entire temperature range.

The ac susceptibility measurements from Ref. [8] were fit to Equation 5.5. The time constants obtained from the fit are plotted with the time constants presented by Matsuhira *et al.*[43] in Fig. 5.7. The agreement between the time constants obtained from fitting to the susceptibility data is slightly better than the agreement between the time constants obtained from fitting to the dc magnetization data. A possible reason for this could be that in ac susceptibility measurements, there is no dependence on a definition of zero magnetization, and therefore there is one less fit parameter. This implies that the fit is more constrained and as a result is most likely more accurate. Contrarily, the dc magnetization measurements require a careful definition of zero magnetization, which is achieved through fitting. It makes sense that the agreement between the values of the time constants obtained from fitting to the ac susceptibility data from Refs. [43] and [8] is better than that of the dc magnetization measurements, as there is a larger error associated with fitting an exponential decay where the zero is a fit parameter. This is one important advantage that ac measurements have over dc measurements.



# Chapter 6

## Bringing It All Together

In terms of monopole dynamics, Jaubert and Holdsworth performed groundbreaking Monte Carlo simulations[10, 11] that they compared to ac susceptibility data by Snyder *et al.*[36, 42]. By using the monopole picture of spin ice and fitting to the quasi-plateau region of the relaxation in Ref. [36], Jaubert and Holdsworth simulated a Coulomb gas of monopoles to capture the dynamics crossover from the quasi-plateau relaxation regime down to about 1 K. By measuring the ac susceptibility of  $\text{Dy}_2\text{Ti}_2\text{O}_7$  down to lower frequencies and temperatures, Yaraskavitch *et al.* experimentally confirmed that there is an Arrhenius temperature activated relaxation with an energy barrier of 9.79 K.[8] The work presented in this thesis builds on the measurements in Ref. [8]. Fig. 6.1 contains a plot of the relaxation times obtained from the measurements in this thesis as well as some of the relaxation times obtained from other studies of  $\text{Dy}_2\text{Ti}_2\text{O}_7$ . One can see that the Arrhenius temperature activated relaxation exposed by these dc magnetization measurements qualitatively bridges the gap between the results from different measurement techniques, specifically the higher temperature ac susceptibility and the low temperature thermal measurements. The yellow highlighted portion of the plot in Fig. 6.1 represents the region of temperature and relaxation time space that the work in this thesis explores.

It is unclear why the measurements below 0.4 K in Fig. 6.1 are showing a lack of temperature dependence in the relaxation time. It is possible that the measurements experience a loss of equilibrium, meaning the spins become decoupled from the lattice. Since thermal measurements probe the spins through the lattice, it is important to have the spins and the lattice thermally coupled and if the time scale of their equilibration becomes larger than the measurement window, this would manifest itself as an apparent plateau in the measured relaxation time. This is because the spins would effectively be at a higher temperature since they wouldn't have had enough time to equilibrate with the

lattice. Measurements of the relaxation at 0.36 K do not contain the fast relaxation times reported by Giblin *et al.* in Ref. [6]. The relaxation time was so long at 0.36 K, that the wait time in order to resolve the entire relaxation was longer than the hold time of the dewar on the fridge and helium transfers disrupted the measurement making it very difficult. Due to experimental constraints, a magnetic field of 5 mOe was used to magnetize the sample of  $\text{Dy}_2\text{Ti}_2\text{O}_7$ , compared to the field magnetides of 1-5 Oe used in Ref. [6]. Giblin *et al.* state that they are in the linear response regime, meaning that the applied magnetic field is proportional to the magnetization of the sample. The measurements in this thesis are also in the linear response regime, so it does not seem as though the difference in field magnitude should account for the difference in the relaxation at 0.36 K. To add to this, the measurements of the relaxation by Matsuhira *et al.*[43] using the same field magnitudes ( $\sim 5$  Oe) as Giblin *et al.* do not contain the short relaxation times that Giblin *et al.*[6] report at 0.36 K. The remaining difference between the measurements is the so-called “charging time”, or time that the applied magnetic field is turned on for. Giblin *et al.*[6] apply their field for 5-60s, not letting the sample fully magnetize. Matsuhira *et al.*[43], apply the field and heat the sample in order to magnetize the sample fully and quickly. In the measurements in this thesis the field is applied until the sample is magnetized with no added heating.

As shown in the previous section, the results in this thesis agree with very recent ac and dc measurements of the relaxation of  $\text{Dy}_2\text{Ti}_2\text{O}_7$  by Matsuhira *et al.*. To summarize, the work presented in this thesis agrees with results obtained from similar magnetic measurement techniques, with the exception of magnetic measurements by Giblin *et al.* in Ref. [6] Previous ac susceptibility measurements on  $\text{Dy}_2\text{Ti}_2\text{O}_7$ [36, 39] have commented on the out-of-phase susceptibility not fitting to a single Debye relaxation - yet have not been able to explain the spectra other than suggesting “glassy” behaviour at low temperature. Further inspection of the results presented here has lead to: a connection between ac and dc characteristics of spin ice within the temperature window shown in Fig. 6.1, a characterization of the relaxation as being a stretched exponential with long time tail, and physical explanations for these characteristics through comparison to Monte Carlo simulation.

Several theories[11, 18] do expect an Arrhenius temperature activated freezing to kick in at low temperature, and this is what our measurements suggest. The relaxation function is expected to be a single exponential decay from simulation (with periodic boundary conditions) of the dipolar spin ice model. However, the measured relaxation is actually a stretched exponential decay with a long time tail which has been attributed, by comparison to Monte Carlo simulation, to a small amount of stuffing (long-time tail) and surface effects (stretching) that the real sample is exhibiting. This work should add to the current monopole picture of spin ice by starting the conversation about impurities and their effect

on the motion of monopoles. Now, when picturing the monopoles moving around the spin ice vacuum, researchers should be considering the effects of different types of defects, like the small amount of stuffing discussed earlier. The defects in spin ice act similar to defects in an electric conductor and provide an interesting avenue for further research of resistance in magnetricity (the motion of monopoles).

This work also brings to light surface effects which have only been considered in terms of demagnetization in ac susceptibility.[8, 43] There has been some work on the effect of the surface on the dynamics of water ice recently.[61, 62] The final implication of the work presented in this thesis is that a temperature activated basic spin-flip process with an energy barrier of  $U = 4$  K, which has previously been assumed to be a solely quantum tunnelling temperature-independent process (stochastic quantum tunnelling hypothesis[10, 60]), would account for the missing energy in the 5.2 K barrier predicted by the dipolar spin ice model simulation.

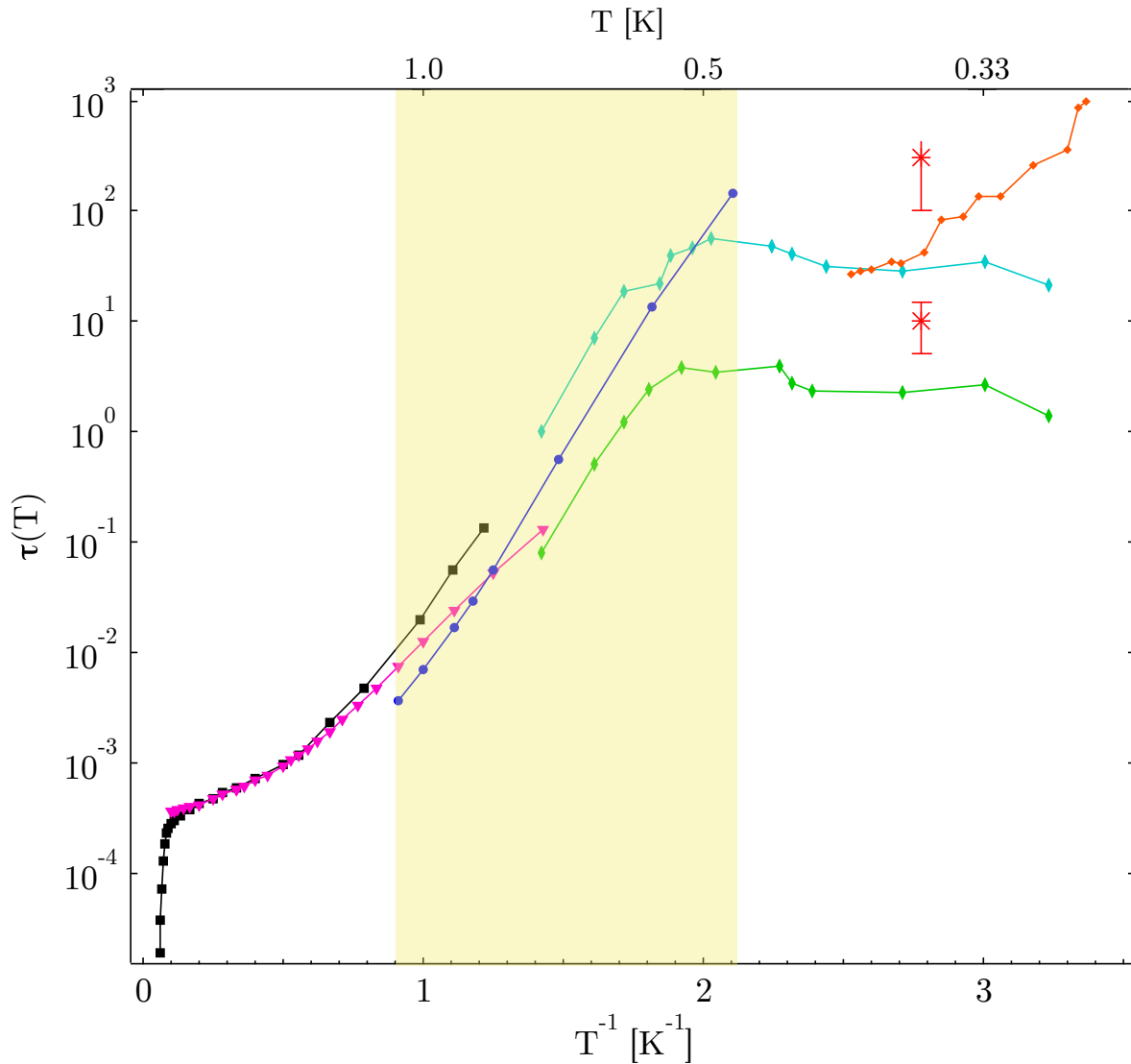


Figure 6.1: Relaxation times obtained from the dc magnetization measurements in the context of other work. Thermal relaxation from Ref. [33]  $\tau_\alpha$  (light blue diamonds) and  $\tau_\beta$  (light green diamonds). AC susceptibility from Ref. [36] (black squares). Simulation of a Coulomb gas of monopoles from Ref. [10] (pink triangles). DC magnetic relaxation from Ref. [6] (red asterisks). Magnetocaloric measurements from Ref. [45] (red diamonds). DC magnetization from this work (blue circles). The yellow highlighted section of the graph is the region of relaxation time and temperature space that the measurements in this thesis have explored.



# Chapter 7

## Conclusions

- **A planar magnetometer was constructed and tested**

A planar magnetometer that consists of a 1<sup>st</sup> order SQUID gradiometer was constructed and mounted on a dilution refrigerator. AC susceptibility measurements were performed on Dy<sub>2</sub>Ti<sub>2</sub>O<sub>7</sub> in order to test functionality. The ac susceptibility measurements agreed with the ac susceptibility results from Ref. [8].

- **DC and ac measurements have been consolidated**

Measurements of the dc magnetic relaxation of Dy<sub>2</sub>Ti<sub>2</sub>O<sub>7</sub> were made on a newly constructed planar gradiometer. The measurements were compared to ac susceptibility measurements that were transformed into the time domain using the fluctuation-dissipation theorem[55]. The results agree qualitatively, each set of relaxations demonstrating stretched exponential behaviour with a long-time algebraic tail. Both measurements confirm a temperature activated Arrhenius freezing of the relaxation time  $\tau(T) = \tau_o \exp(\Delta E/T)$ , with an energy barrier of about  $\sim 9$  K.

- **Relaxation profile has been characterized**

Contrary to previous characterizations of the relaxation of the spin ice Dy<sub>2</sub>Ti<sub>2</sub>O<sub>7</sub>, where the relaxation was treated as a single or double exponential, in this work the relaxation has been fit to a stretched exponential function.

- **Physical explanations have been made by comparison to Monte Carlo simulations**

Monte Carlo simulations of the dipolar spin ice model governed by Metropolis dynamics were performed by a collaborator and compared to the experimental results of this thesis. Simulations of the dipolar spin ice model using periodic boundary conditions yielded a single exponential relaxation and a temperature activated relaxation time with an energy barrier of 5.2 K. Diluting spins, adding a simple stacking fault, or adjusting the exchange energies did not lead to the relaxation profile observed experimentally. It was found that performing the simulations using open boundary conditions, with a small amount of stuffing (0.3%) yielded the same stretched exponential, long-time tail profile observed experimentally in the relaxations. The addition of an extra energy barrier,  $U = 4$  K, in the simulation was necessary to achieve the 9 K energy barrier observed experimentally. By reaching qualitative agreement between simulation and experiment the stretched exponential behaviour is attributed to surface effects in the material, the long-time tail is attributed to a small amount of stuffed spins, and the extra energy barrier is thought to be caused by some temperature dependence of the underlying spin flip process.

## 7.1 Implications

This work has led to a new way of identifying defects in spin ice materials. The long-time tail in the relaxation provides a new characterization mechanism for defects in magnetic materials, which may be thought of like the residual resistance in metals at low temperatures. The long-time algebraic tails are a newly discovered characteristic that is solely due to a very small amount of stuffing present in the material. More work needs to be done, both experimentally and theoretically, in order to clarify the connection between impurities and the long-time tail so that it can be useful in the characterization of the purity of magnetic materials.

# Appendix A

## Fitting Details

### A.1 Determining Zero

The magnetization measurements were made with a SQUID, and as a result, the raw readout signal was in the form of a voltage which is directly proportional to the magnetic flux threading the SQUID, which is directly proportional to the magnetization of the sample. The voltage signal is measured relative to a dc voltage, that the flux-locked loop “locks” on to. This is usually close to 0 V, but not exactly, so this means that the  $y$ -axis of the raw data does not have any absolute meaning, only relative. In order to analyze the data properly, it was important to define zero magnetization. Another important definition is  $t_o$ , the time at which the field is turned off. A typical approach to defining these quantities is outlined in Fig. A.1. To determine a definition of zero magnetization, the baseline of the magnetization decay was fit to a double exponential function with a  $y$  offset. Only the tail end of the decay from the relaxation was fit. In this approximation, the data is fit quite well. Other ideas, were to fit to a straight line, since the baseline appears flat on a linear scale, however, since the long-time tail in the data means the magnetization is not fully relaxed, it is better to fit to a function, where  $f(t = \infty) = 0$ . Fig. A.1 (c) shows this fitting and the resulting definition of zero magnetization.

The definition of zero in the  $x$ -axis (time axis) is the instant at which the field is turned off. In order to determine the time at which the field is turned off, a line is drawn along the data leading up to the switching off of the field and another line is drawn along the beginning of the relaxation. Their intersection is defined as  $t_o$ , the instant the field is turned off. This is shown in Fig. A.1 (b). In Fig. A.1 (a), the full magnetization characteristic at  $T = 0.9$  K is shown. The SQUID measures the magnetization of the sample with no field

turned on at first, then the field is turned on and the sample is magnetized. The field is then turned off and the relaxation is measured.

## A.2 Normalizing

Each of the relaxations has been normalized so that the point on the  $y$ -axis, at which the magnetization begins to decay from, is defined as  $C(0) = 1$ . This was achieved by estimating the saturated dc magnetization once the field had been applied for long enough.<sup>1</sup> For the lower temperatures (0.475, 0.55, 0.675 K) there were some issues with the speed of the field being turned off using a power supply. This was not a problem, as things are slower at these temperatures. To deal with this, the first few points were omitted and the true dc magnetization value was estimated by fitting a line extremely close to the start of the relaxation and then plugging in the definition of  $t_o$  to determine the magnetization. At the higher temperatures, this issue was rectified by using a DAC instead of a power supply, which is much faster, meaning that when the field was turned off there was no lag or time constant having to do with the electronics that was present in the actual data. With the faster electronics used for the relaxations (measured at 0.800 K, 0.85 K, 0.900 K, 1.0 K, 1.1 K), the maximum magnetization was found by fitting a line to the magnetization just before the field was switched off. It was important to fix the issue of the speed of the electronics, especially at high temperatures, because a time constant due to electronics that is comparable to the measured time constant of relaxation will lead to the time constant of the power supply being a part of the relaxation.

## A.3 Signal Averaging

The raw data from the magnetic relaxation experiments was sampled at a frequency of 1000 points per second, using a high-speed GAGE PCI scope card, that could store up to  $128 \times 10^6$  samples in memory in a single shot. 1000 samples/s was the minimum speed that the card was able to read at, which was appropriate for higher temperature data, where the magnetic signal was changing quickly with time, however, at lower temperatures this speed produced large amounts of data that needed to be signal averaged in order to be handled computationally. Data files were over a Gb in some cases, so performing fitting on data this dense was impossible on a fast laptop. In order to not lose any important

---

<sup>1</sup>It was judged that the field had been applied for “long enough” once it appeared that the magnetization was no longer changing, or changing very little with time (on a linear scale).

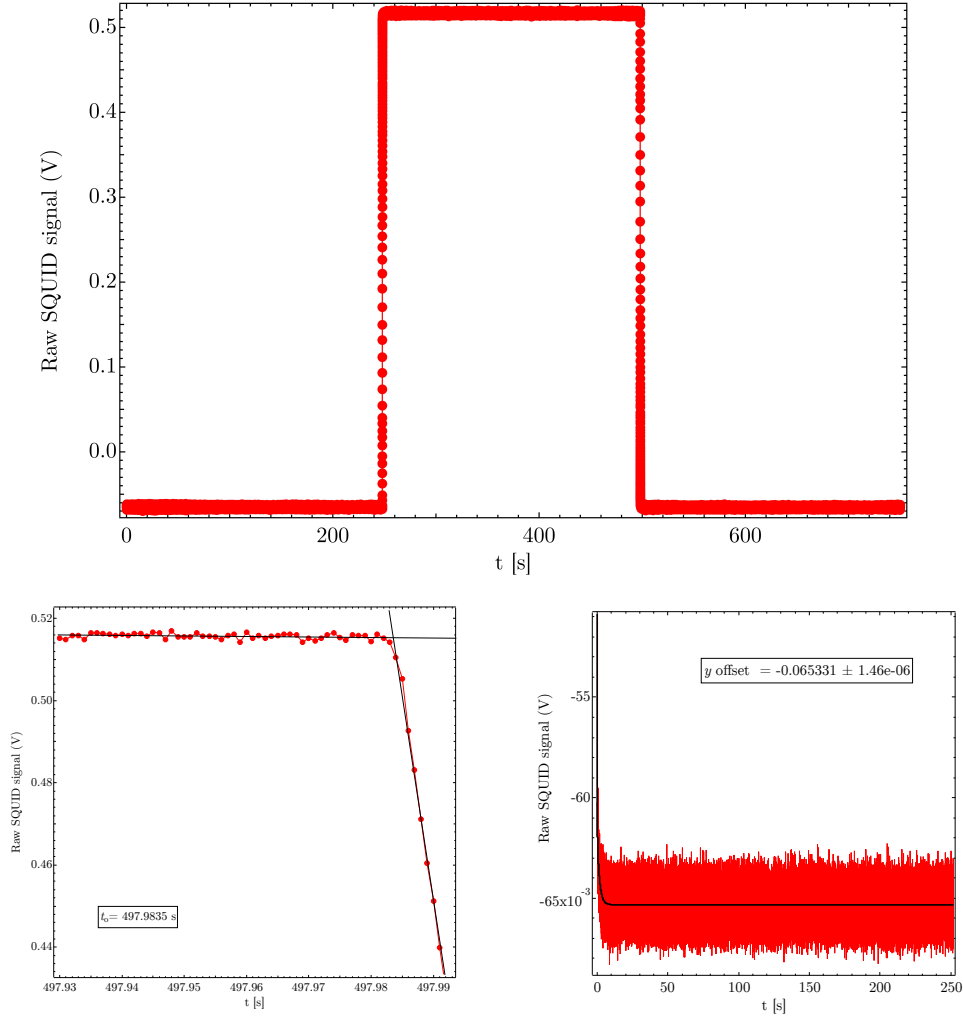


Figure A.1: Example of how zeros were defined in the raw magnetic relaxation data at  $T = 0.9$  K. (a) The full characteristic of the dc magnetization experiment. The SQUID measures the magnetization of the sample with no field applied and suddenly at 250 s, the field is turned on and the sample becomes magnetized. At about 500 s, the field is turned off and the relaxation is observed. (b) The time at which the field is turned off,  $t = 0$ , is defined by intersecting lines drawn along the fully magnetized portion of the data and the beginning of the relaxation, respectively. (c) Zero magnetization is defined by fitting the bottom portion of the relaxation to a double exponential function with the  $y$  offset as a fitting parameter. The  $y$  offset is taken to be the definition of  $C(t) = 0$ .

information about the relaxation a running average was performed, and the sample box size was adjusted so that at long times, when the relaxation was closer to equilibration and was changing less with time, a larger averaging box was used.

Fig. A.2 contains a plot of the raw data at 0.475 K and its signal average. The averaging was done carefully and checked at each step in order to make sure no real characteristics in the data (other than noise) were lost. At higher temperatures, like 0.9 K, only the long time tail was signal averaged and the first few seconds were left as raw data, since the signal was so fast at those shorter times.

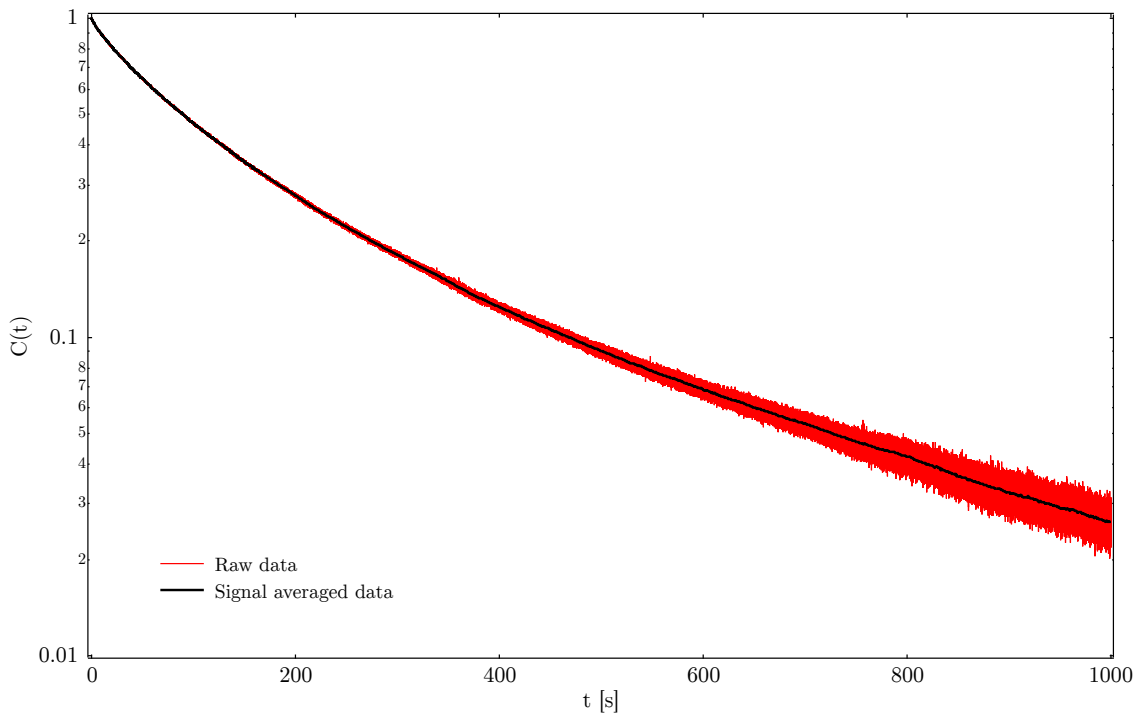


Figure A.2: Example of signal averaging at  $T = 0.475$  K. A boxcar algorithm was used to perform the running average. At denser parts of data, a larger averaging box was used. When data was more sparse, a smaller averaging box was used. At the highest temperatures, at short times, no averaging was performed.

## A.4 Fitting Limits

The limits for performing the fits on the data were determined in a systematic way. Once it was realized that the data was represented best by a stretch exponential function, the data was plotted as  $\ln(-\ln(C(t)))$  versus  $\ln(t)$ , which is a convenient form when fitting to a stretch exponential. A quick linear fit was performed on the straightest portion of the data and the fit was subtracted from the data, leaving the residual. The resulting residuals provided a gauge to see where the data deviates from the stretch exponential and the long time tail kicks in. Fig. A.3 shows the residuals used to determine the fit limits. Limits were chosen such that the deviation was less than approximately 0.1.

## A.5 Fit Functions

As mentioned earlier in the thesis, the decays of the magnetization were fit to a single, double, and stretched exponential. The residuals of each fit at 0.675 K are shown in Fig. A.4. The double and stretched exponential functions fit the data much better than the single exponential. The stretched exponential fit residual looks slightly better than the double exponential fit residual, especially near  $t = 0$  in Fig. A.4. Also, since the stretched exponential has less fit parameters, the fit is more constrained making it the superior choice over the double exponential.

## A.6 Fitting Methods

A least squares fitting algorithm was used to fit the data to a stretch exponential between the limits discussed in the previous section. However, the data was fit in two ways. First, the data was simply fit to  $C(t) = e^{-(t/\tau)^\beta}$ . Second, the data was fit to a line  $y = mx + b$ , where  $y = \ln(-\ln(C(t)))$ ,  $m = \beta$ ,  $x = \ln(t)$  and  $b = \beta \ln(\tau)$ , which was possible by first computing  $\ln(-\ln(C(t)))$  and  $\ln(t)$ . The two methods produced slightly different fit parameters:  $\beta$  and  $\tau$ . The results were within error of one another (determination of error is discussed next). Fig. A.5 shows the percent difference between the fit parameters determined by the two methods for each temperature.

To determine error bars for the fitting parameters, the limits of fitting were expanded and contracted by a factor of 2 and the resultant change in the fit parameters were used as the upper and lower error bars. This is more honest than simply using the standard

deviations, as the choice of limits on the fit have a strong impact on the fit and can cause deviations in the fit parameters that are greater than the standard deviations. The fit parameters and error bars using the first fits (to  $C(t) = e^{-(t/\tau)^\beta}$ ) are plotted in the Results chapter. The fit parameters from the fits to a stretch exponential, not a line, were used as their standard deviations were slightly lower.



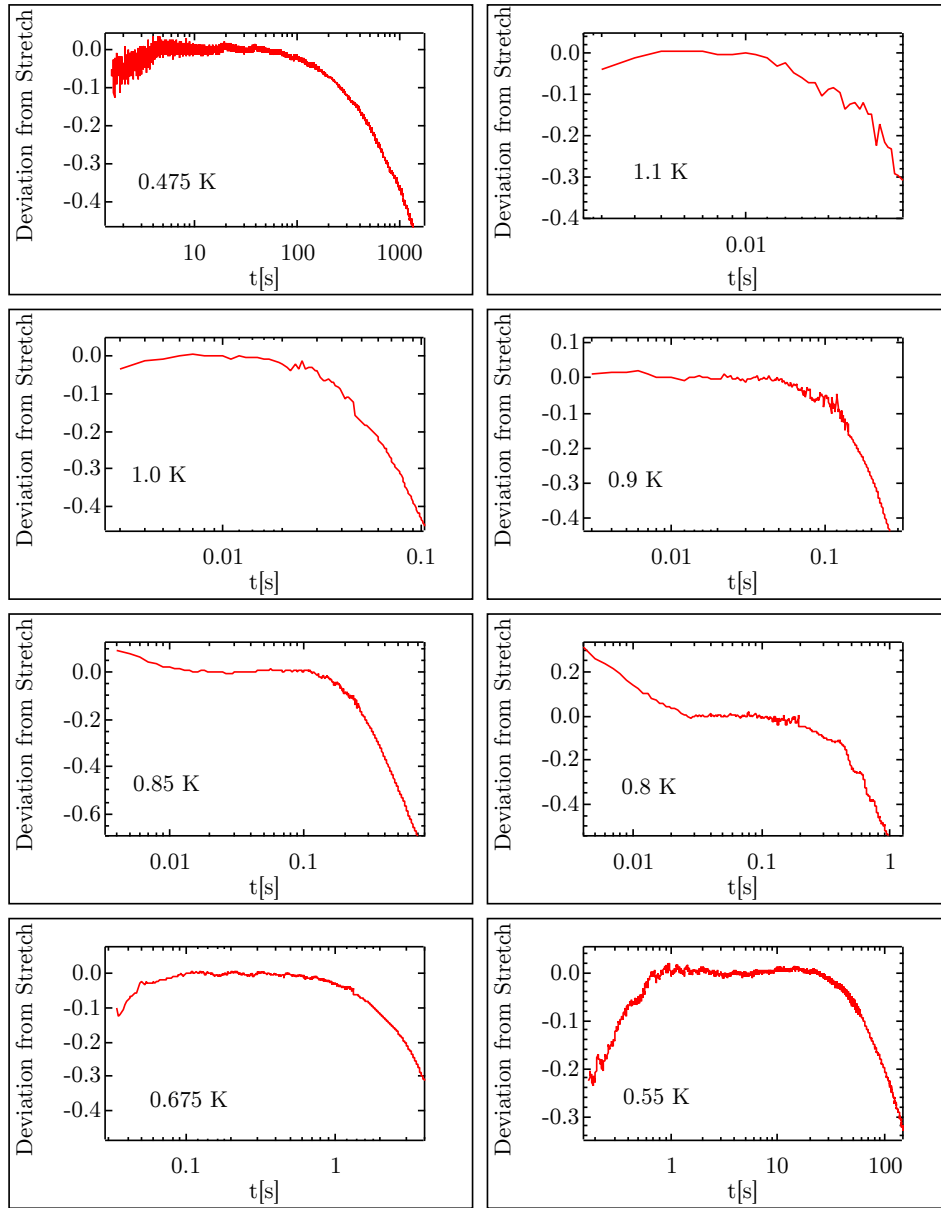


Figure A.3: Deviations from a quick fit to a stretch exponential in the  $\ln(-\ln(C(t)))$  versus  $\ln(t)$  representation. Limits in  $t$  were chosen such that the deviation was below about 0.1. For instance, at 0.55 K, limits of 0.2 s to 58 s were chosen. At this temperature, the magnetic relaxation is slower so we do not lose much information by starting our fit at 0.2 s, however at 1.0 K, we start the fit at the first data point, 0.003 s since the magnetic relaxation is fast there.

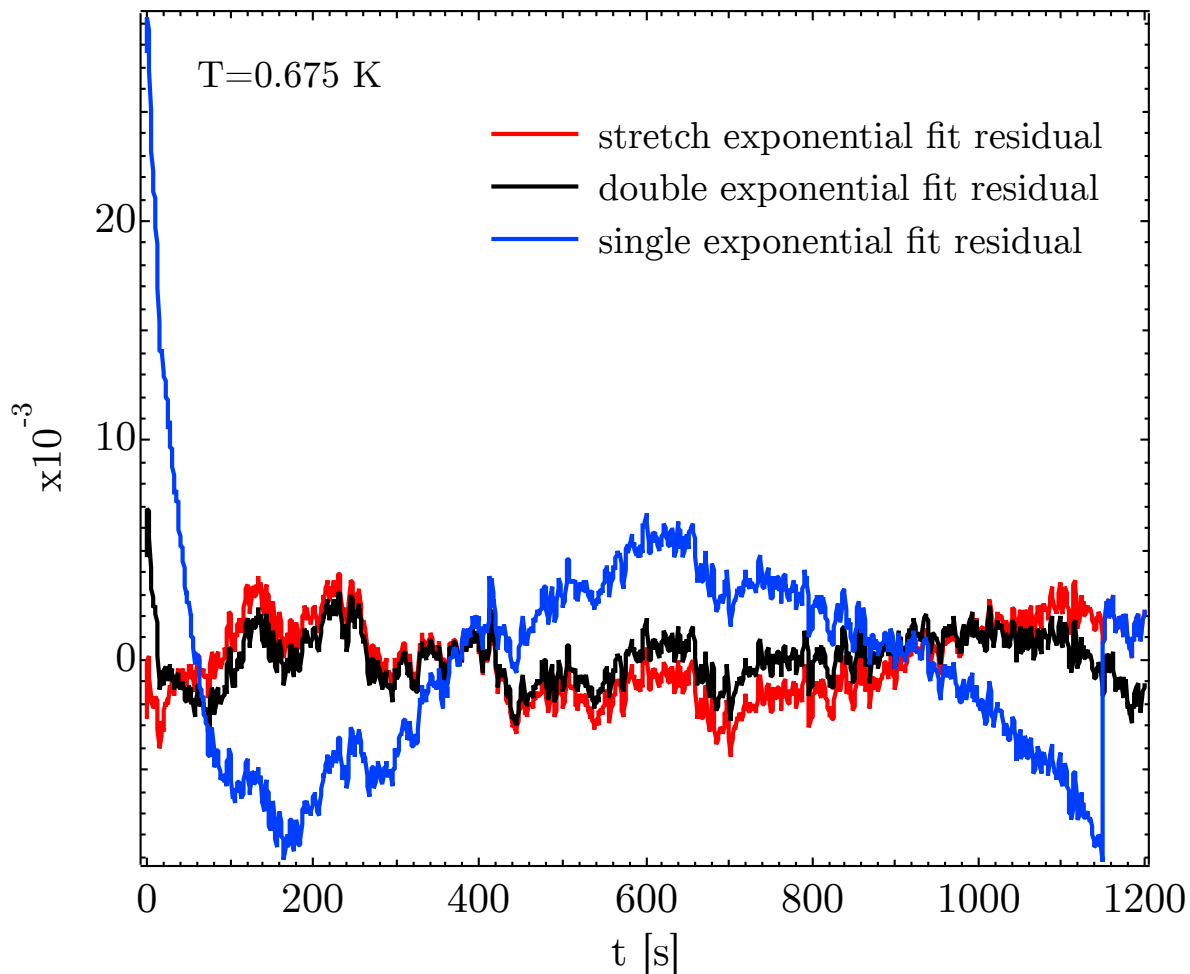


Figure A.4: Residuals of the different fits at 0.675 K. The double and stretched exponential fits capture the relaxation better than the single exponential. The stretched exponential seems to capture the beginning of the decay slightly better than the double exponential. The double exponential has four free fitting parameters, whereas the stretched exponential has only two free parameters, meaning that the fit to the stretched exponential is more constrained. Nevertheless, the double exponential can still be a valid method for parameterizing the data.

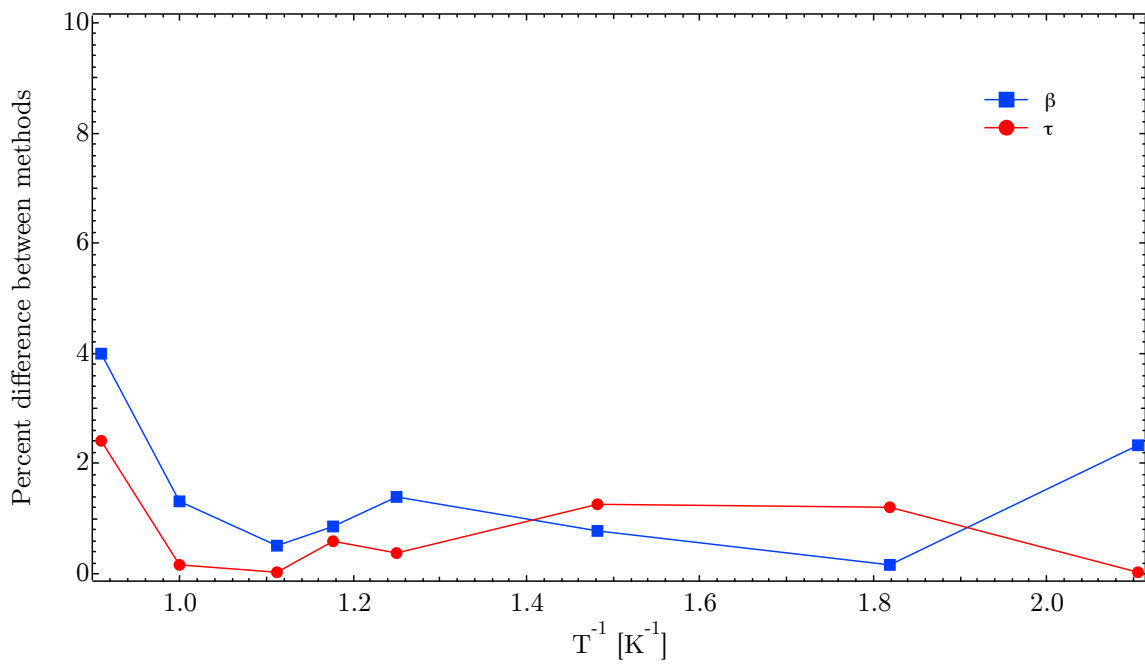


Figure A.5: Percent difference between fitting approaches for the fitting parameters.



# Appendix B

## Measurement Challenges

### B.1 Vibrations

As discussed earlier, noise can be an important issue when using SQUIDs to make sensitive measurements. When initial measurements were made, on the magnetometer, there was some noise present in the signal. This noise was a small vibration with an amplitude of about one part in a thousand of the total magnetization at 900 mK, with a frequency of  $\sim 3.8$  Hz. The noise likely came from vibrations in the building, possibly coming from the mechanical pump room across the hallway. This oscillation, remained present in all the measurements, but due to its sinusoidal nature and consistent frequency, the oscillation was fit to and subtracted from the dc magnetization data, as shown in Fig. B.1. At low temperatures, the measurements took a long time, and the phase of this oscillation would change about every 200 s. To accommodate the shifting phase, the data was fit in segments, sewn together and then subtracted.

### B.2 Magnetic Shielding

Although the magnetometer uses a SQUID gradiometer that should cancel out any external magnetic fields that are spatially constant, it is still beneficial to isolate the system from external fields by shielding. The sample should be in zero field, except for the applied field in the experiment. Without shielding, the sample is exposed to Earth's field ( $\sim 0.3 - 0.6$  Oe)[49] Since spatial constraints on the dilution fridge did not allow for shielding to be placed inside the vacuum can, a large cylindrical mu-metal shield was placed around

the outside of the dewar instead. The sample and magnetometer resided more than four feet below the top of the shield. The shield was put up before the fridge was cooled each time so that the sample was cooled in zero field.

### B.3 Backaction

In the SQUID gradiometer, the sample sits within one of the pick-up coils that is inductively coupled to one of the SQUID loops. The feedback coil sits around the other pick-up coil, which is inductively coupled to the other SQUID loop. Whenever magnetic flux is detected by the SQUID, an equal and opposite magnetic flux is applied by the feedback coil, because of the FLL circuitry. Because the sample is inductively coupled to the SQUID, anytime the feedback coil applies a magnetic flux to the SQUID, the sample experiences a small amount of that field and responds accordingly. This means that the FLL circuit experiences back-action. This was experimentally verified by unlocking the flux-locked-loop which applies 12 V across the feedback resistor, which in turn, applies a sizeable amount of current to the feedback coil. The flux-locked loop was relocked and the response of the sample was observed. Because the magnetization of the sample had already been quantified for a certain applied field, the sample's magnetization from the application of a field coming from the feedback coil (with a known amount of voltage) allowed the amount of back-action to be quantified.

The solution to this problem was to use the FLL voltage with the right current limiting resistor to apply a current to the excitation coil that is in the opposite direction of the back-action. This correction was made by first determining what current is required for the excitation coil to magnetize the sample to the same amount as when 12 V are applied across the feedback resistor. Dividing 12 V by that current value gives the resistance of the current limiting resistor that should be placed between the FLL output and the excitation coil. This rough calculation was performed and a 40 k $\Omega$  resistor was chosen at first. The results are shown in Fig. B.2. The relaxation of the sample's magnetization was greatly reduced, but the back-action was overcorrected and increasing the resistance improved the correction further.

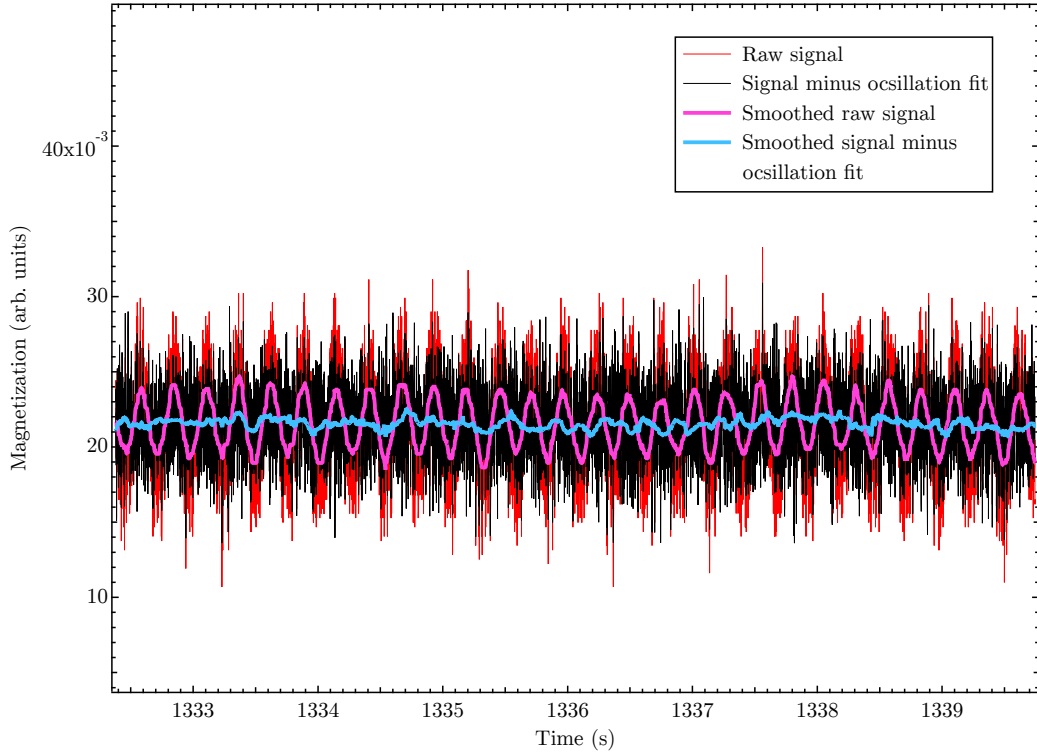


Figure B.1: Subtraction of oscillatory noise from vibrations in dc magnetization measurement at 550 mK. The raw signal had an oscillation to it (red line), which is shown more clearly in the smoothed data (magenta line). The oscillation was fit to a sine function and subtracted from the data. The raw data after the subtraction (black line) and after smoothing (blue line) is shown.

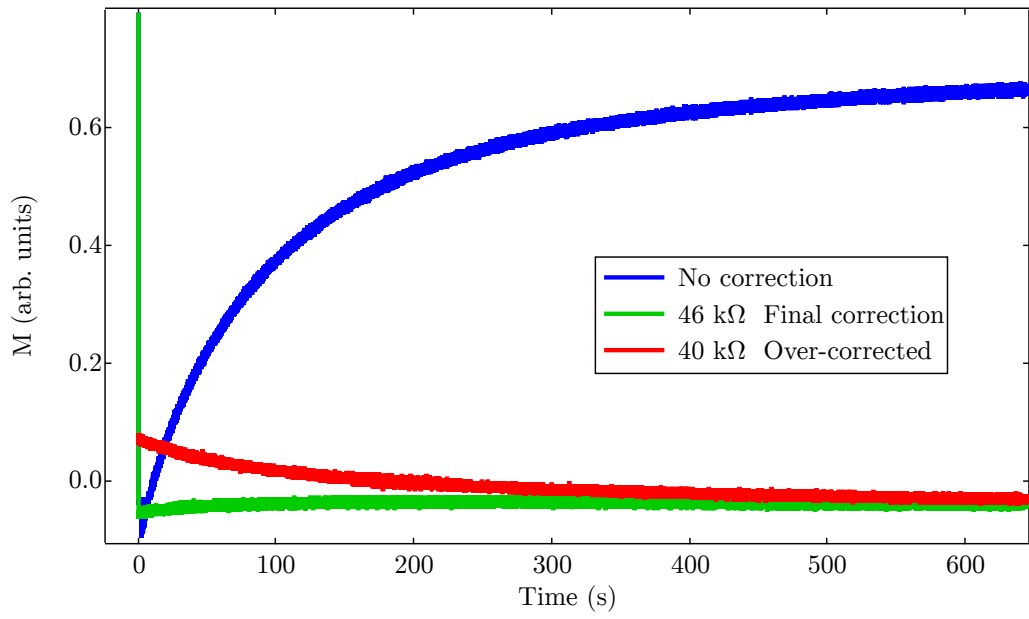


Figure B.2: Correction for back-action in gradiometer.



# Appendix C

## Demagnetization

The ac susceptibility data presented in Chapter 4, was corrected for demagnetization effects according to the formula:

$$\begin{aligned}\frac{1}{\chi} &= \frac{1}{\chi_A} - 4\pi N \\ \chi' &= \frac{\chi'_A - 4\pi N(\chi'^2_A + \chi''^2_A)}{(1 - 4\pi N\chi'_A)^2 + (4\pi N\chi''_A)^2} \\ \chi'' &= \frac{\chi''_A}{(1 - 4\pi N\chi'_A)^2 + (4\pi N\chi''_A)^2}\end{aligned}\tag{C.1}$$

In the case of the needle sample (Sample B), the demagnetizing factor was calculated to be  $N = 0.0533$ . In the case of the stubby sample, whose spectra are used in the calibration, the demagnetizing factor was calculated to be  $N = 0.1126$ . The spectra of the stubby sample, whose c-axis is also aligned along the [110] crystal axis, were measured by Luke Yaraskavitch. In Fig. C.1, the two different ac susceptibility spectra are shown for the different geometries. They have been corrected for demagnetizing effects, however in order for their spectra to be volume independent and the difference in couplings to be accounted for a least-squares method must be applied so that the two spectra overlap across all frequencies. Fig. C.2 shows the two spectra after the calibration. The calibration factors for the needle and stubby sample are 3.1406 and 25.3880, respectively.

No demagnetization was carried out for the time based dc magnetization measurements. The demagnetization correction for the ac susceptibility is straightforward in that it is constant over frequency and gets mixed into the in-phase and out-of-phase components in a manageable way. However, for a field quench measurement (dc), the relaxation has many

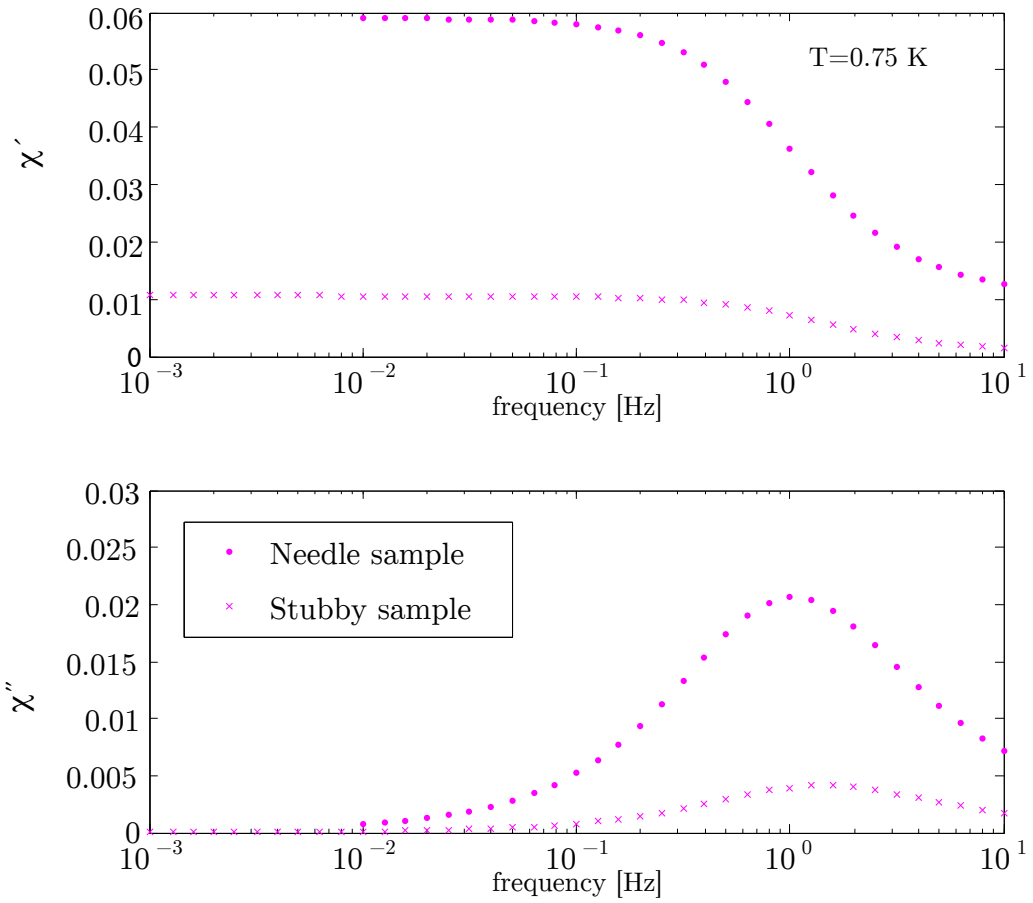


Figure C.1: AC susceptibility spectra for two different geometries at  $T = 0.75$  K

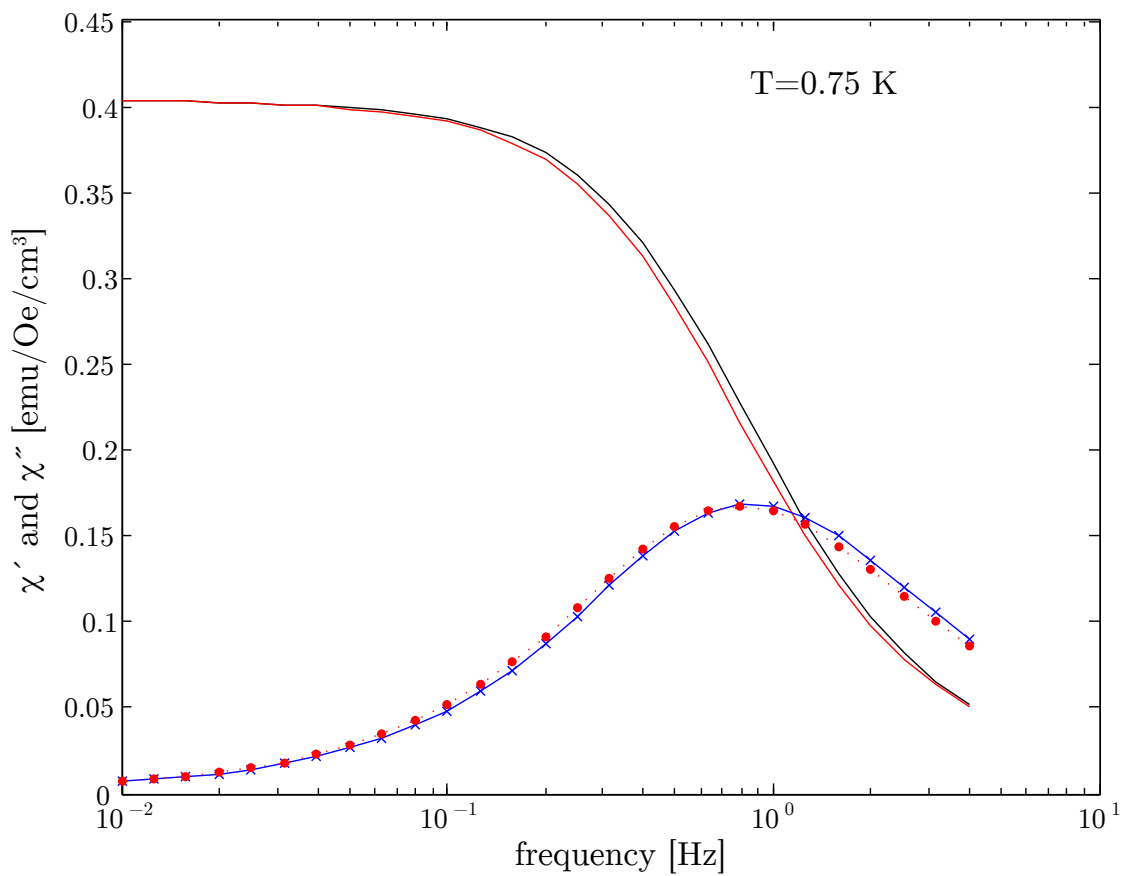


Figure C.2: Calibrated ac susceptibility spectra for two different geometries at  $T = 0.75$  K

frequency modes that make up the decay in magnetization. The frequencies are convoluted. One possible way to deal with this would be to convert the time-based measurements into frequency space using the fluctuation-dissipation theorem, just as the ac susceptibility was converted into the time-base, and perform the demagnetization correction and reconvert the corrected spectrum into the time base. Depending on how well the fitting of the spectra is, one may lose significant features in the spectra through two conversions. This process was not carried out in this work, but could be a topic for future research.

# References

- [1] Castelnovo, C., Moessner, R., and Sondhi, S. L. Magnetic monopoles in spin ice. *Nature*, **451**, p. 42, 2008.
- [2] Morris, D. J. P., Tennant, D. A., Grigera, S. A., Klemke, B., Castelnovo, C., Moessner, R., Cztemasty, C., Meissner, M., Rule, K. C., Hoffmann, J.-U., Kiefer, K., Gerischer, S., Slobinsky, D., and Perry, R. S. Dirac Strings and Magnetic Monopoles in the Spin Ice  $\text{Dy}_2\text{Ti}_2\text{O}_7$ . *Science*, **326**, pp. 411–414, 2009.
- [3] Ryzhkin, I. A. Magnetic Relaxation in Rare-Earth Oxide Pyrochlores. *Journal of Experimental and Theoretical Physics* *101*, **101**, p. 481, 2005.
- [4] Fennell, T., Deen, P., Wildes, A., Schmalzl, K., Prabhakaran, D., Boothroyd, A., Aldus, R., McMorrow, D. F., and Bramwell, S. T. Magnetic Coulomb Phase in the Spin Ice  $\text{Ho}_2\text{Ti}_2\text{O}_7$ . *Science*, **326**, pp. 415–417, 2009.
- [5] Bramwell, S. T., Giblin, S. R., Calder, S., Aldus, R., Prabhakaran, D., and Fennell, T. Measurement of the charge and current of magnetic monopoles in spin ice. *Nature*, **461**, p. 956, 2009.
- [6] Giblin, S. R., Bramwell, S. T., Holdsworth, P. C. W., Prabhakaran, D., and Terry, I. Creation and measurement of long-lived magnetic monopole currents in spin ice. *Nature Phys.*, **7**, pp. 252–258, 2011.
- [7] Dunsiger, S. R., Aczel, A. A., Arguello, C., Dabkowska, H., Dabkowski, A., Du, M.-H., Goko, T., Javanparast, B., Lin, T., Ning, F. L., Noad, H. M. L., Singh, D. J., Williams, T. J., Uemura, Y. J., Gingras, M. J. P., and Luke, G. M. Spin Ice: Magnetic Excitations without Monopole Signatures using Muon Spin Rotation. *Phys. Rev. Lett.*, **107**, p. 207207, 2011.

- [8] Yaraskavitch, L. R., Revell, H. M., Meng, S., Ross, K. A., Noad, H. M., Dabkowska, H. A., Gaulin, B. D., and Kycia, J. B. Spin dynamics in the frozen state of the dipolar spin ice material  $\text{Dy}_2\text{Ti}_2\text{O}_7$ . *Phys. Rev. B. Rapid Comm.*, **85**, p. 020410, 2012.
- [9] den Hertog, B. C. and Gingras, M. J. P. Dipolar Interactions and Origin of Spin Ice in Ising Pyrochlore Magnets. *Phys. Rev. Lett.*, **84**, pp. 3430–3433, 2000.
- [10] Jaubert, L. and Holdsworth, P. Signature of magnetic monopoles and Dirac string dynamics in spin ice. *Nature Phys.*, **5**, pp. 258–261, 2009.
- [11] Jaubert, L. D. C. and Holdsworth, P. C. W. Magnetic monopole dynamics in spin ice. *J. Phys.: Condens. Matter*, **23**, p. 164222, 2011.
- [12] Harris, M. J., Bramwell, S. T., McMorrow, D. F., Zeiske, T., and Godfrey, K. W. Geometrical Frustration in the Ferromagnetic Pyrochlore  $\text{Ho}_2\text{Ti}_2\text{O}_7$ . *Phys. Rev. Lett.*, **79**, pp. 2554–2557, 1997.
- [13] Ramirez, A., Hayashi, A., Cava, R., Siddharthan, R., and Shastry, B. Zero-point entropy in 'spin-ice'. *Nature*, **399**, p. 333, 1999.
- [14] Bernal, J. D. and Fowler, R. H. A Theory of Water and Ionic Solution, with Particular Reference to Hydrogen and Hydroxyl Ions. *Journal of Chemical Physics*, **1**, p. 515, 1933.
- [15] Pauling, L. The Structure and Entropy of Ice and of Other Crystals with Some Randomness of Atomic Arrangement. *Journal of the American Chemical Society*, **57**, p. 2680, 1935.
- [16] Kadowaki, H., Doi, N., Aoki, Y., Tabata, Y., Sato, T. J., Lynn, J., Matsuhira, K., and Hiroi, Z. Observation of magnetic monopoles in spin ice. *J. Phys. Soc. Japan*, **78**, p. 103706, 2009.
- [17] Castelnovo, C., Moessner, R., and Sondhi, S. L. Thermal Quenches in Spin Ice. *Phys. Rev. Lett.*, **104**, p. 107201, 2010.
- [18] Castelnovo, C., Moessner, R., and Sondhi, S. L. Debye-Huckel theory for spin ice at low temperature. *Phys. Rev. B*, **84**, p. 144435, 2011.
- [19] Melko, R. G. and Gingras, M. J. P. Monte Carlo studies of the dipolar spin ice model. *J. Phys.: Condens. Matter*, **16**, pp. R1277–R1319, 2004.

- [20] Quilliam, J. A., Yaraskavitch, L. R., Dabkowska, H. A., Gaulin, B. D., and Kycia, J. B. Dynamics of the Magnetic Susceptibility Deep in the Coulomb Phase of the Dipolar Spin Ice Material  $\text{Dy}_2\text{Ti}_2\text{O}_7$ . *Phys. Rev. B*, **83**, p. 094424, 2011.
- [21] Gardner, J., Gingras, M., and Greedan, J. E. Magnetic pyrochlore oxides. *Rev. Mod. Phys.*, **82**, pp. 53–107, 2010.
- [22] Balents, L. Spin liquids in frustrated magnets. *Nature*, **464**, pp. 199–208, 2010.
- [23] Savary, L., Ross, K. A., Gaulin, B. D., Ruff, J. P. C., and Balents, L. Definitive Evidence for Order-by-Quantum-Disorder in  $\text{Er}_2\text{Ti}_2\text{O}_7$ . *unpublished*, 2012.
- [24] Ross, K. A., Savary, L., Gaulin, B. D., and Balents, L. Quantum Excitations in Quantum Spin Ice. *Phys. Rev. X*, **1**, p. 021002, 2011.
- [25] Ehlers, G., Huq, A., Diallo, S. O., Adriano, C., Rule, K., Cornelius, A. L., Pagliuso, P., and Gardner, J. S. Low energy spin dynamics in the spin ice  $\text{Ho}_2\text{Sn}_2\text{O}_7$ . *J. Phys.: Condens. Matter*, **24**, p. 076005, 2012.
- [26] Ashcroft, N. W. and Mermin, N. D. *Solid State Physics* (Thompson Learning, 1976).
- [27] Matsuhira, K., Hiroi, Z., Tayama, T., Takagi, S., and Sakakibara, T. A new macroscopically degenerate ground state in the spin ice compound  $\text{Dy}_2\text{Ti}_2\text{O}_7$  under a magnetic field. *J. Phys.: Condens. Matter*, **14**, pp. L559–L565, 2002.
- [28] Fukazawa, H., Melko, R. G., Higashinaka, R., Maeno, Y., and Gingras, M. J. P. Magnetic anisotropy of the spin-ice compound  $\text{Dy}_2\text{Ti}_2\text{O}_7$ . *Phys. Rev. B*, **65**, p. 054410, 2002.
- [29] Anderson, P. W. Ordering and Antiferromagnetism in Ferrites. *Phys. Rev.*, **102**, p. 1008, 1956.
- [30] Bramwell, S. T. and Harris, M. J. Frustration in Ising-type spin models on the pyrochlore lattice. *J. Phys.: Condens. Matter*, **10**, pp. L215–L220, 1998.
- [31] Siddharthan, R., Shastry, B. S., Ramirez, A. P., Hayashi, A., Cava, R. J., and Rosenkranz, S. Ising Pyrochlore Magnets: Low-Temperature Properties, “Ice Rules, and Beyond. *Phys. Rev. Lett.*, **83**, pp. 1854–1857, 1999.
- [32] Melko, R. G., den Hertog, B. C., and Gingras, M. J. Long-Range Order at Low Temperatures in Dipolar Spin Ice. *Phys. Rev. Lett.*, **87**, p. 067203, 2001.

- [33] Klemke, B., Meissner, M., Strehlow, P., Kiefer, K., Grigera, S. A., and Tennent, D. A. Thermal Relaxation and Heat Transport in the Spin Ice Material DTO. *J. Low Temp. Phys.*, **163**, pp. 345–369, 2011.
- [34] Hiroi, Z., Matsuhira, K., Takagi, S., Tayama, T., and Sakakibara, T. Specific Heat of Kagome ice... *J. Phys. Soc. Japan*, **72**, p. 411, 2003.
- [35] Levin, Y. Electrostatic correlations: from plasma to biology. *Rep. Prog. Phys.*, **65**, 11, p. 1577, 2002.
- [36] Snyder, J., Ueland, B. G., Slusky, J. S., Karunadasa, H., Cava, R. J., and Schiffer, P. Low-temperature spin freezing in the  $\text{Dy}_2\text{Ti}_2\text{O}_7$  spin ice. *Phys. Rev. B*, **69**, p. 064414, 2004.
- [37] Onsager, L. Deviations from Ohms law in weak electrolytes. *J. Chem. Phys.*, **2**, pp. 599–615, 1934.
- [38] Liu, Y., Sellmyer, D. J., and Shindo, D. *Handbook of Advanced Magnetic Materials* (Springer Science and Business Media, Inc., New York, NY, 2006).
- [39] Matsuhira, K., Hinatsu, Y., Tenya, K., and Sakakibara, T. Low temperature magnetic properties of frustrated pyrochlore ferromagnets  $\text{Ho}_2\text{Sn}_2\text{O}_7$  and  $\text{Ho}_2\text{Ti}_2\text{O}_7$ . *J. Phys.: Condens. Matter*, **12**, pp. L649–L656, 2000.
- [40] Matsuhira, K., Hinatsu, Y., and Sakakibara, T. Novel dynamic magnetic properties in the spin ice compound  $\text{Dy}_2\text{Ti}_2\text{O}_7$ . *J. Phys.: Condens. Matter*, **13**, pp. L737–L746, 2001.
- [41] Snyder, J. S., Ueland, B. G., Slusky, J. S., Karunadasa, H., Cava, R. J., Mizel, A., and Schiffer, P. Quantum-Classical Reentrant Relaxation Crossover in  $\text{Dy}_2\text{Ti}_2\text{O}_7$  Spin Ice. *Phys. Rev. Lett.*, **91**, p. 107201, 2003.
- [42] Snyder, J., Slusky, J. S., Cava, R. J., and Schiffer, P. How ‘spin-ice’ freezes. *Nature*, **413**, pp. 48–51, 2001.
- [43] Matsuhira, K., Paulsen, C., L’hotel, E., Sekine, C., Hiroi, Z., and Takagi, S. Spin Dynamics at Very Low Temperature in  $\text{Dy}_2\text{Ti}_2\text{O}_7$ . *J. Phys.: Soc. Jap.*, **80**, p. 123711, 2011.
- [44] Snyder, J., Slusky, J. S., Cava, R. J., and Schiffer, P. Dirty spin ice: The effect of dilution of spin freezing in  $\text{Dy}_2\text{Ti}_2\text{O}_7$ . *Phys. Rev. B*, **66**, p. 064432, 2002.



- [45] Orendáč, M., Hanko, J., Čížmár, E., Orendáčová, A., Shirai, M., and Bramwell, S. T. Magnetocaloric study of spin relaxation in dipolar spin ice  $\text{Dy}_2\text{Ti}_2\text{O}_7$ . *Phys. Rev. B.*, **75**, p. 104425, 2007.
- [46] Fennell, T., Petrenko, O. A., Fák, B., Gardner, J. S., Bramwell, S. T., and Ouladdiaf, B. Neutron Scattering studies of the spin ices  $\text{Ho}_2\text{Ti}_2\text{O}_7$  and  $\text{Dy}_2\text{Ti}_2\text{O}_7$  in applied magnetic field. *Phys Rev B*, **72**, p. 224411, 2005.
- [47] Clarke, J. and Braginski, A. I. *The SQUID Handbook Vol. 1* (Wiley-VCH Verlag GmbH and Co. KGaA, Weinheim, 2004).
- [48] Josephson, B. D. Possible new effects in superconductive tunnelling. *Phys. Rev. Lett.*, **1**, pp. 251–253, 1962.
- [49] Griffiths, D. J. *Introduction to Electrodynamics* (Pearson Education Inc., Upper Saddle River, New Jersey, 1999), 3rd edition.
- [50] Mück, M., Korn, M., Mugford, C. G. A., and Kycia, J. B. A simple three-channel dc SQUID system using time domain multiplexing. *Rev Sci Instrum.*, **75**, p. 2660, 2004.
- [51] Gardner, J. S., Gaulin, B. D., and McK. Paul, D. Single crystal growth by the floating-zone method of a geometrically frustrated pyrochlore antiferromagnet,  $\text{Tb}_2\text{Ti}_2\text{O}_7$ . *J. Cryst. Growth*, **191**, p. 740, 1998.
- [52] Aharoni, A. Demagnetizing factors for rectangular ferromagnetic prisms. *J. Appl. Phys.*, **83**, 6, p. 3432, 1998.
- [53] Onsager, L. Reciprocal relations in irreversible processes. I. *Phys. Rev.*, **37**, pp. 405–426, 1931.
- [54] Onsager, L. Reciprocal relations in irreversible processes. II. *Phys. Rev.*, **38**, pp. 2265–2279, 1931.
- [55] Kubo, R. The fluctuation-dissipation theorem. *Rep. on Prog. in Phys.*, **29**, pp. 255–284, 1966.
- [56] Biltmo, A. and Henelius, P. Unreachable glass transition in dilute dipolar magnet. *Nat. Commun.*, **3**, p. 857, 2012.
- [57] Yavors’kii, T., Fennell, T., Gingras, M. J. P., and Bramwell, S. T.  $\text{Dy}_2\text{Ti}_2\text{O}_7$  Spin Ice: A Test Case for Emergent Clusters in a Frustrated Magnet. *Phys. Rev. Lett.*, **101**, p. 037204, 2008.

- [58] Lau, G. C., Freitas, R. S., Ueland, B. G., Muegge, B. D., Duncan, E. L., Schiffer, P., and Cava, R. J. Zero-point entropy in stuffed spin-ice. *Nature Phys.*, **2**, pp. 249–253, 2006.
- [59] Ueland, B. G., Lau, G. C., Freitas, R. S., Snyder, J., Dahlberg, M. L., Muegge, B. D., Duncan, E. L., and Cava, R. J. Magnetothermal study of a Dy-stuffed spin ice:  $\text{Dy}_2(\text{Dy}_x\text{Ti}_{2-x})\text{O}_{7-x/2}$ . *Phys. Rev. B*, **77**, p. 144412, 2008.
- [60] Ehlers, G., Cornelius, A. L., Orendae, M., Kajnakova, M., Fennell, T., Bramwell, S. T., and Gardner, J. S. Dynamical crossover in 'hot' spin ice. *J. Phys.: Condens. Matter*, **15**, pp. L9–L15, 2003.
- [61] Ryzhkin, I. A. and Petrenko, V. F. Violation of ice rules near the surface: A theory for the quasiliquid layer. *Phys. Rev. B*, **65**, p. 012205, 2001.
- [62] Watkins, M., Pan, D., Wang, E. G., Michaelides, A., VandeVondele, J., and Slater, B. Large variation of vacancy formation energies in the surface of crystalline ice. *Nat. Mater.*, **10**, pp. 794–798, 2011.